2022

Taken By Storm: The Rise And Fall Of Tau From Microtubule-Associated To Aggregated To Degraded

Melina Theoni Gyparaki
University of Pennsylvania

Taken By Storm: The Rise And Fall Of Tau From Microtubule-Associated To Aggregated To Degraded

Abstract

Tau is a microtubule-associated protein, which promotes neuronal microtubule assembly and stability. Accumulation of tau into insoluble aggregates known as neurofibrillary tangles (NFTs) is a pathological hallmark of several neurodegenerative diseases, known as tauopathies. Aggregated proteins are normally degraded by the cell's protein degradation mechanisms, autophagy or the ubiquitin-proteasome system (UPS). In tauopathies, however, the efficiency of these degradation pathways becomes challenged by the abnormal accumulation of the tau protein, which consequently, does not get fully degraded. The current hypothesis is that small, soluble oligomeric tau species preceding NFT formation cause toxicity. However, thus far, visualizing the spatial distribution of tau monomers and oligomers inside cells under physiological or pathological conditions has not been possible. Moreover, it is unclear whether certain tau aggregate species are more resistant to degradation. Here, using single-molecule localization microscopy, we show that tau forms small oligomers on microtubules ex vivo. These oligomers are distinct from those found in cells exhibiting tau aggregation and could be precursors of aggregated tau in pathology. Furthermore, using an unsupervised shape classification algorithm that we developed, we show that different tau phosphorylation states are associated with distinct tau aggregate species. Using machine learning, we also show that autophagy and UPS target distinct classes of tau aggregates for degradation. More specifically, we propose a model where tau fibrils are targeted by UPS for degradation and NFTs are mostly degraded by autophagy, generating more tau monomers and oligomers as well as small fibrils. Our work elucidates tau's nanoscale composition under nonaggregated and aggregated conditions ex vivo and further informs our understanding of how tau aggregates become degraded by the cell's degradation pathways.

Degree Type
Dissertation

Degree Name
Doctor of Philosophy (PhD)

Graduate Group
Biology

First Advisor
Melike Lakadamyali

Keywords
dementia, frontotemporal, microtubule, neurodegenerative, oligomer, tau

Subject Categories
Biology

TAKEN BY STORM: THE RISE AND FALL OF TAU FROM MICROTUBULE-ASSOCIATED TO

AGGREGATED TO DEGRADED

Melina Theoni Gyparaki

A DISSERTATION

in

Biology

Presented to the Faculties of the University of Pennsylvania

in

Partial Fulfillment of the Requirements for the

Degree of Doctor of Philosophy

2022

Supervisor of Dissertation

Dr. Melike Lakadamyali

Associate Professor of Physiology

Graduate Group Chairperson

Dr. Brian Gregory

Professor of Biology

Dissertation Committee

Dr. Tatyana Svitkina, Professor of Biology

Dr. Michael Lampson, Professor of Biology

Dr. Elizabeth Rhoades, Professor of Chemistry

Dr. Nicholas Betley, Assistant Professor of Biology

This work is dedicated to my parents, Kalliroi Papadopoulou and Konstantinos Gyparakis for their unconditional love and support and for all the sacrifices they made to ensure I have the best education and opportunities possible. Σας ευχαριστώ πολύ, μαμά και μπαμπά!

ACKNOWLEDGMENT

Sansom feel like home! You all were not only colleagues and friends but also felt like family to me. I will miss you all!

A big thank you to the wonderful friends I made in grad school: Amy, Kari, Jessica, Heather, Adriana, Andrea, Ellery, Rebecca, Jackie and to my college friends: Jonida, Reem, Caroline, Eliska, Mira and Gaia for all their support and encouragement during this time! I want to thank specifically Amy. Our daily texts mean the world to me! I am so happy we went through grad school together and finishing at the same time!

To my partner in all things, Nick, thank you so much for being in my life. I love you very much. Thank you for being there for me during the good and the bad. Thank you for helping me practice for my prelims, thank you for being the best peer reviewer I could ask for and thank you for your patience and support throughout this difficult journey of grad school. Also, thank you to Nick's parents, John and Rosemary and his family for welcoming me in their home and treating me like family from the beginning. Your support has been so important throughout grad school.

I also want to thank a little baby named Scottie. Scottie you are the most beautiful Yorkie and smartest doggie I have ever met. Thank you for being so playful and for filling Nick and I's lives with so much joy. We love you!

Lastly, I want to thank my family. My aunt Fiona and uncle Panayotis and my aunt Despina for all their support and love. My grandmothers in heaven, Theoni and Dora who always encouraged me to pursue my dreams. And of course my parents: my mom, Kalliroi, in heaven and my dad, Kostas, on earth. None of this would have been possible without their support and the sacrifices they made so that I have the best opportunities. Mama, thank you for motivating me to study and be academically driven from a young age. Thank you

for all the hours you put in every day to be by my side while I was doing homework at school. Thank you for working so hard so that I go to the best schools. I am immensely grateful for it all. Mpampa, thank you for always believing in me and teaching me to never lose hope and to always chase my dreams. Thank you mama and mpampa for helping me achieve my dreams and for teaching me to follow the light. I found Melike who shines bright and had the best grad school experience I could have imagined!

ABSTRACT

TAKEN BY STORM: THE RISE AND FALL OF TAU FROM MICROTUBULE-ASSOCIATED TO

AGGREGATED TO DEGRADED

Melina Theoni Gyparaki

Melike Lakadamyali

Tau is a microtubule-associated protein, which promotes neuronal microtubule assembly and stability. Accumulation of tau into insoluble aggregates known as neurofibrillary tangles (NFTs) is a pathological hallmark of several neurodegenerative diseases, known as tauopathies. Aggregated proteins are normally degraded by the cell's protein degradation mechanisms, autophagy or the ubiquitin-proteasome system (UPS). In tauopathies, however, the efficiency of these degradation pathways becomes challenged by the abnormal accumulation of the tau protein, which consequently, does not get fully degraded. The current hypothesis is that small, soluble oligomeric tau species preceding NFT formation cause toxicity. However, thus far, visualizing the spatial distribution of tau monomers and oligomers inside cells under physiological or pathological conditions has not been possible. Moreover, it is unclear whether certain tau aggregate species are more resistant to degradation. Here, using single-molecule localization microscopy, we show that tau forms small oligomers on microtubules *ex vivo*. These oligomers are distinct from those found in cells exhibiting tau aggregation and could be precursors of aggregated tau in pathology. Furthermore, using an unsupervised shape classification algorithm that we developed, we show that different tau phosphorylation states are associated with distinct tau aggregate species. Using machine learning, we also show that autophagy and UPS target distinct classes of tau aggregates for degradation. More specifically, we propose a model where tau fibrils are targeted by UPS for degradation and NFTs are mostly

degraded by autophagy, generating more tau monomers and oligomers as well as small fibrils. Our work elucidates tau's nanoscale composition under nonaggregated and aggregated conditions *ex vivo* and further informs our understanding of how tau aggregates become degraded by the cell's degradation pathways.

TABLE OF CONTENTS

LIST OF FIGURES

CHAPTER 1. INTRODUCTION

Tau protein

Tau is a microtubule-associated protein (MAP), which is encoded by the *MAPT* gene on chromosome 17 in humans (Neve et al. 1986). Transcription of the *MAPT* gene generates 6 tau protein isoforms by alternative splicing of exons 2, 3 and 10 in the central nervous system (CNS) (Goedert et al. 1989). Tau protein consists of an N-terminal region followed by microtubule-binding domains, a proline-rich region and a C-terminal region. The 6 tau isoforms differ in the amount of microtubule-binding domains and amino-terminal inserts they contain (Fig. 1.1A). Including exon 10 results in 4 microtubule-binding domains (4R), while omitting exon 10 results in 3 microtubule-binding domains (3R). Similarly, tau can have 2, 1 or 0 amino-terminal inserts (2N, 1N or 0N) through regulation of exons 2 and 3. In the peripheral nervous system (PNS), production of larger tau proteins can occur by transcription of exons 4A, 6 and 8 (Goedert, Spillantini, and Crowther 1992) (Fischer and Baas 2020). All 6 tau isoforms are present in the adult human brain while only 0N3R is present in the fetal human brain (T. Guo, Noble, and Hanger 2017). Mice and rats mostly express 4R tau (T. Guo, Noble, and Hanger 2017). Tau is evolutionary conserved and evidence of a *MAPT*-like gene has been found in many organisms, including sharks, hagfish and lampreys (Sündermann, Fernandez, and Morgan 2016). Tau's evolutionary conservation suggests that it must perform essential biological functions.
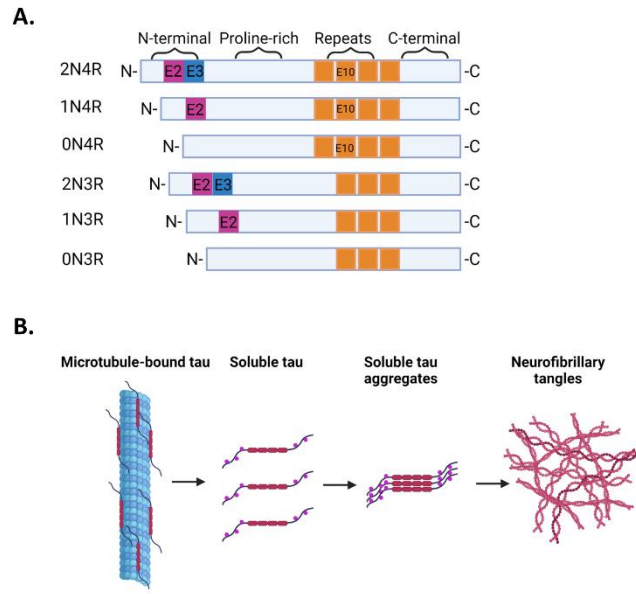
Figure 1.1: Tau in physiology and pathology.

A. Tau's different isoforms and their structural domains. Created with BioRender.com. B. A model of the tau aggregation pathway. Created with BioRender.com.

Tau structure

Tau is a highly soluble, heat-stable, intrinsically disordered protein (IDPs) with a transient secondary structure (Battisti et al. 2012). As with other IDPs, tau's conformation can change depending on whether or not it is associated with other proteins. Tau's microtubule-binding domains associate with the building blocks of microtubules, α- and β-tubulin proteins. More specifically, tau binds dynamically at the interface of tubulin heterodimers via a group of conserved tau residues (Kadavath et al. 2015). Recently, Cryo-Electron Microscopy (Cryo-EM) combined with molecular modeling showed that tau binds along the microtubule protofilament, therefore stapling together tubulin subunits and stabilizing the tubulin polymer (Kellogg et al. 2018). The peptide ^{275}KVQIINKK^{280} between regions 1 and 2 of the microtubule-binding domains (R1-R2), which is unique to the 4R

isoforms, strongly induces microtubule polymerization leading to greater microtubule affinity for 4R isoforms compared to 3R (Goode and Feinstein 1994). Tau's N-terminal projection domain projects away from the microtubule surface and can interact with the neuronal plasma membrane, membranous compartments such as mitochondria as well as other cytoskeletal elements (Jung et al. 1993) (Brandt, Léger, and Lee 1995). The projection domain is particularly important for maintaining proper spacing between axonal microtubules (Chen et al. 1992). Tau's proline-rich region has been shown to bind to the Src-homology 3 (SH3) domains of Fyn kinase protein, which has a role in protein trafficking (Reynolds et al. 2008) (Baba et al. 2009).

Tau's structure is also affected by post-translational modifications of its residues. Specifically, tau phosphorylation can facilitate the formation of α- and β-helices giving tau a secondary structure (Grundke-Iqbal et al. 1986) (Bancher et al. 1989). Moreover, tau hyperphosphorylation is thought to be involved in the formation of large insoluble tau aggregates known as paired-helical filaments (PHFs) and neurofibrillary tangles (NFTs) as it can affect tau's affinity for microtubules and is therefore linked to tau's dissociation from the microtubules (Grundke-Iqbal et al. 1986). However, it is not fully understood whether phosphorylation happens before or after PHF formation. It has been suggested that phosphorylation could stabilize the α-helix structure on tau (Sibille et al. 2012).

Tau's physiological role as a microtubule-associated protein

Tau has been traditionally thought to stabilize axonal microtubules (Drechsel et al. 1992) and to be involved in microtubule assembly and dynamics influencing neuron morphology (Drubin and Kirschner 1986) (Panda, Miller, and Wilson 1999). Moreover, tau is known to have roles in axon development and navigation (Dawson et al. 2001) (Sayas et al. 2015).

Early work showed that tau reduces the tubulin concentration required for microtubule polymerization (Weingarten et al. 1975). More recently, tau's role as a regulator of microtubule dynamics was proposed. More precisely, rather than stabilizing microtubules, it was suggested that tau allows microtubules to have long labile domains, which would explain why tau's concentration increases toward the distal, more labile end of microtubules (Qiang et al. 2018).

It has also been hypothesized that tau could be competing with motor proteins for microtubule binding and its overexpression could potentially cause obstacles and "traffic jams" for organelles and other proteins (Stamer et al. 2002) (Ebneth et al. 1998)(Dixit et al. 2008). In particular, it was recently suggested that in physiological conditions, concentrated regions of tau on neuronal axons, described as "cohesive islands" could be leading to kinesin-1 dissociation from the microtubules, while dynein is thought to slowly move through them (Siahaan et al. 2019) (R. Tan et al. 2019). However, this view is challenged by studies reporting that axonal transport dynamics are not altered by tau's knockdown or overexpression. Further, the "kiss-and-hop" mechanism of tau suggests that tau binding on microtubules is transient and hence should not disrupt other protein binding sites (Yuan et al. 2008) (Janning et al. 2014).

Furthermore, there is evidence that tau protects microtubules from cleavage by the microtubule-severing protein katanin and knockdown of tau results in cleavage and loss of microtubules as well as reduced axonal length (Siahaan et al. 2019) (R. Tan et al. 2019) (Qiang et al. 2006) (Yu et al. 2008). Tau depletion or mislocalization away from the axon may therefore render microtubules vulnerable to cleavage. Additionally, tau may be crucial for maintaining the non-branched structure of the axon as tau depletion results in an

increase in neuronal branching, normally seen in dendrites which have low tau expression (Yu et al. 2008).

Tau in pathology

Tau has disease relevance and its abnormal aggregation is a characteristic of several neurodegenerative diseases including Alzheimer's disease, which are collectively known as tauopathies. Other tauopathy examples include progressive supranuclear palsy, Pick's disease, corticobasal degeneration (CBD), chronic traumatic encephalopathy (CTE) as well as some frontotemporal dementias (Orr, Sullivan, and Frost 2017). In the case of familial tauopathies, such as some frontotemporal dementias, there can be mutations in the *MAPT* gene, which usually occur either in the microtubule-binding region of tau or can affect the number of microtubule-binding domains of the tau protein. Such familial tauopathies are associated with hyperphosphorylated, aggregated tau indicating that the mutations alone are sufficient to induce pathogenic tau formation (Poorkaj et al. 1998) (Hutton et al. 1998)(Spillantini et al. 1998)(Ghetti et al. 2015). Moreover, pathological tau aggregates from different tauopathies often involve different tau isoforms. For instance, while AD has a mix of 3R and 4R tau aggregates, Pick's disease is characterized by strictly 3R tau aggregates and progressive supranuclear palsy by 4R tau aggregates (G. Lee and Leugers 2012). It is also possible that tau isoforms are differentially expressed in certain brain regions depending on the tauopathy, which is the case for tau isoforms in AD and CTE, which are differentially expressed across the hippocampus (Cherry et al. 2021). Also, the nature of tau protofilaments can vary depending on the tauopathy with some protofilaments being disease-specific, which has made the idea of structure-specific tau strains prevalent in recent years (Fitzpatrick et al. 2017) (Sanders et al. 2014) (Falcon et al. 2018) (Falcon et al. 2019) (W. Zhang et al. 2019a). More specifically, the structure of

5

paired helical filaments (PHFs) and straight filaments (SFs) from AD brains was found to have a similar C-shaped conformation involving repeats 3, 4 and R' in CTE, but in the case of CTE there were two packing arrangements between the protofilaments known as Type I and II (Fitzpatrick et al. 2017) (Falcon et al. 2019). Cryo-EM work revealed some further differences in the conformations of fibrils in CBD, which were also grouped in two categories, Type I and II (W. Zhang et al. 2020). Recent work showed that tau PTMs influence tau filament structure and contribute to the structural diversity of different tau strains (Arakhamia et al. 2020). Interestingly, the transmission of distinct tau strains does not depend on strain isoform compositions but instead on their unique pathological conformations (He et al. 2020).

The tau aggregation pathway is not fully understood but a prominent model suggests that tau falls off the microtubule following its hyperphosphorylation at multiple residues, initially forming small, soluble aggregates also known as oligomers, and later forming larger insoluble aggregates such as PHFs and NFTs (V. M. Y. Lee, Goedert, and Trojanowski 2001) (Fig. 1.1B). This model has not been fully validated and there is evidence that contradicts it. NFTs were initially thought to be the most toxic tau species as they could be detected in post-mortem brains of AD patients (Guillozet et al. 2003) (Santacruz et al. 2005). However, work from animal models showed that neurodegeneration leading to synaptic dysfunction and behavioral abnormalities can occur in the absence of NFTs (Wittmann et al. 2001) (Cowan et al. 2010). Additionally, NFTs can persist for 20-30 years in neurons, which makes them less likely to be causing immediate toxicity (Morsch, Simon, and Coleman 1999). Currently, the most likely hypothesis is that earlier stages of the tau aggregation pathway are responsible for tau toxicity, particularly tau oligomers. Injecting tau oligomers into the brains of wild-type mice is sufficient to cause synaptic and cognitive

abnormalities (Lasagna-Reeves et al. 2011) (Castillo-Carranza et al. 2014). Moreover, tau oligomers have been associated with synaptic loss in transgenic mice expressing wild-type human tau (Spires et al. 2006) (Berger et al. 2007) (Clavaguera et al. 2013).

The nature of tau oligomers

Tau oligomers are most commonly associated with tau pathology. Soluble tau oligomers have been isolated from homogenized AD brains (Patterson et al. 2011). It has also been reported that tau oligomers can become insoluble by lengthening and adopting a β-sheet conformation, which gives them a granular appearance under atomic force microscopy (AFM) (Takashima 2013). However, it is not clear whether tau oligomers are solely a pathological feature. *In vitro* studies have shown that tau with the disease relevant P301L mutation isolated from yeast and wild-type tau isolated from rats can form tau clusters and oligomers on taxol-stabilized microtubules, respectively (Vandebroek et al. 2006) (Makrides et al. 2003). Moreover, the formation of an electrostatic zipper between the N-terminal halves of two tau molecules aligned in an anti-parallel fashion, is thought to facilitate tau dimerization (Rosenberg et al. 2008). Protein dimerization is an evolutionary favored mechanism to promote protein complex formation in physiological settings in addition to pathology (Marianayagam, Sunde, and Matthews 2004). Therefore, it is possible that tau can also dimerize and oligomerize to promote its physiological functions and is not only associated with its pathological state.

Despite the extensive *in vitro* characterization of tau oligomers, visualizing them in intact cells has been a challenge due to their small size and the resolution constraints of conventional light microscopy. Elucidating the nanoscale composition of tau on microtubules, in tau oligomers as well as in other tau aggregates is essential to improve

our understanding of the mechanisms that lead to pathological tau generation and propagation as well as in the search for therapeutic targets for tauopathies.

Degradation of tau aggregates

The over accumulation of tau aggregates in tauopathies is partly due to their inefficient clearance by UPS and autophagy, which normally degrade aggregated proteins in cells. UPS traditionally degrades short-lived poly-ubiquitinated proteins that are smaller in size to fit through the proteolytic core of the proteasome complex, while autophagy degrades larger proteins, aggregates and damaged organelles via the formation of the autophagosome which fuses into the lysosome where degradation occurs (Lilienbaum 2013). Since tau is naturally unfolded, it is a good candidate for UPS degradation in its monomeric state, while larger aggregates are thought to be degraded by autophagy due to their size (Bence, Sampat, and Kopito 2001) (Hamano et al. 2021). It is known that proteasome activity decreases in the aging brain and is lower in brain areas, which are abundant in NFTs (Keller, Gee, and Ding 2002) (Keller, Hanni, and Markesbery 2000). Moreover, *in vitro* studies have shown that aggregated tau can interact with the proteasome and inhibit its function (Keck et al. 2003). Recently, in a mouse model of tauopathy, accumulation of insoluble tau correlated with a decrease in proteasome activity and an increase in ubiquitinated proteins, while activating cAMP-protein kinase (PKA) signaling led to improvement of proteasome function and cognitive performance as well as lower levels of aggregated tau (Myeku et al. 2016). Therefore, the proteasome must be involved in the clearance of some tau aggregate species which can fit through its proteolytic core and is not limited to degrading monomeric tau species. Indeed, there is *in vitro* evidence supporting UPS-mediated tau aggregate degradation (David et al. 2002). Moreover, in studies using cell systems, the addition of proteasome inhibitors leads to an

accumulation of insoluble tau shown biochemically (Babu, Geetha, and Wooten 2005). However, the nature of the insoluble tau species accumulating is yet to be elucidated.

Similarly, there is evidence of autophagy defects such as accumulation of autophagic vacuoles in dystrophic neurites being associated with the presence of filamentous tau seen in AD brains (Nixon et al. 2005) (Sanchez-Varo et al. 2012). In fact, it is thought that the autophagic pathology seen in AD brains is more likely due to autophagy defects rather than activated autophagy (Boland et al. 2008). Inhibiting autophagy leads to accumulation of tau aggregates sometimes both soluble and insoluble species (Hamano et al. 2008). Furthermore, pharmacological activation of autophagy has also been shown to lead to increased clearance of tau aggregates, but as with UPS, the selectivity of the autophagy pathway when degrading tau has not been yet delineated (Congdon et al. 2012) (Krüger et al. 2012). Understanding the pathways that degrade tau and the selectivity of these pathways for different tau species is of great interest in the field.

Tau therapeutic targets

To this day, there are no effective treatments for tauopathies due to the lack of effective therapeutic targets and our limited understanding of the mechanisms of pathological tau generation, which deems tauopathies to be diseases of great complexity. Since tau phosphorylation is the most well-studied post-translational modification of tau and tau hyperphosphorylation is considered a pathological feature of tauopathies, there has been great interest in identifying inhibitors of the kinases catalyzing these increased tau phosphorylation events. GSK-3β and CDK5 kinases are among the most well studied kinases which phosphorylate tau (Tell and Hilgeroth 2013) (Martin et al. 2013). It has been shown that their inhibition reduces tau phosphorylation and tau deposits in mouse models

of tauopathy but it did not offer cognitive improvements to AD patients in a Phase 2 clinical trial (Noble et al. 2005) (Le Corre et al. 2006). Moreover, there is potential in inhibiting other tau post-translational modifications such as O-linked glycosylation and lysine acetylation. An inhibitor of O-linked glycosylation has been shown to reduce tau phosphorylation and the presence of insoluble tau deposits in a transgenic mouse model of tauopathy (Yuzwa et al. 2008). However, those findings have been inconsistent in different studies meaning that inhibition of O-linked glycosylation on its own is not the most effective approach (Borghgraef et al. 2013). Inhibitors of tau acetylation have also shown promise in transgenic mouse models of tauopathy, where there was an improvement in neuron loss (Min et al. 2015).

Another therapeutic approach has been to reduce microtubule dynamics in an attempt to counteract the increased dynamicity of microtubules, and other microtubule deficits seen in mouse models of tauopathy following tau's dissociation from the microtubules in pathology (Hempen and Brion 1996)(Cash et al. 2003). More precisely, there have been multiple therapeutic strategies using microtubule stabilizing drugs such as paclitaxel. Results in mouse models have been promising, however, paclitaxel is not blood brain barrier permeable (B. Zhang et al. 2005) (Brunden et al. 2011). Other microtubule stabilizing drugs that are blood brain barrier permeable have been identified without much success in the clinic (B. Zhang et al. 2012) (Brunden et al. 2010). One of the main challenges of this approach is the toxic effects of the anti-mitotic properties these drugs have in non-neuronal cells.

Inhibiting tau fibrillization had initially shown some promise but has not had much success in clinical trials mostly due to the fact that most fibrillization inhibitors act via unknown mechanisms and could be targeting other pathways leading to adverse effects (Wischik

et al. 2015) (Crowe et al. 2007) (Arkin and Wells 2004) (Akoury et al. 2013). Inhibiting proteolytic processing of tau and improving cellular proteostasis are very promising approaches. However, there are many gaps in our knowledge that currently prevent identifying suitable therapeutic targets in these areas. More specifically, it is thought that cellular proteases such as caspase, calpain, cathepsin and others can cleave tau in a way which generates pathological tau species (Rissman et al. 2004) (Ferreira and Bigio 2011) (Bi et al. 2000). In addition, the large selection of enzymes that can process tau hinder the determination of how they are all connected and whether some are more important than others. Similarly, improving cellular proteostasis is appealing but comes with challenges. For instance, it is not clear whether tau oligomers would only be degraded by autophagy or whether they could also be degraded by UPS. The big gap in our knowledge in this field is that it is not clear which tau aggregate species could be degraded by each pathway and how these tau aggregates impact the protein degradation systems altogether. Elucidating those protein degradation mechanisms of tau aggregates has the potential to yield new therapeutic target candidates.

Currently, one of the most pursued therapeutic avenues for neurodegenerative diseases is immunotherapy (Pedersen and Sigurdsson 2015). Initially, a major concern regarding immunotherapy was whether sufficient intraneuronal antibody concentrations could be achieved in the brain since antibody concentration in the brain is only approximately 0.1% of that in the blood. However, recent work has shown that tau inclusions most likely follow a prion-like method of transmission suggesting that pathological tau released extracellularly could be accessible to antibodies in the interstitial fluid of the brain, thus making immunotherapy a promising approach (Pedersen and Sigurdsson 2015) (Schroeder et al. 2016).

11

Visualizing tau in physiology and pathology

Electron microscopy (EM) approaches have been very informative regarding the structure of the tau protein both in physiology and pathology. Most of our knowledge on the composition of tau filaments and aggregates is thanks to EM and more recently, cryo-EM approaches (Necula and Kuret 2004) (Huseby and Kuret 2016) (Fitzpatrick et al. 2017) (Scheres et al. 2020). Recently, Cryo-EM also provided further insight into how wild type tau binds along the microtubule protofilament in physiology (Kellogg et al. 2018). Similarly, other *in vitro* approaches such as AFM have provided further structural insight into tau, specifically tau oligomers and fibrils (Wegmann, Muller, and Mandelkow 2012)(Makky et al. 2020)(Barrantes et al. 2009).

However, there are still many unknowns regarding tau's distribution in intact neurons. One of the main challenges of visualizing tau in intact cells has been the fact that tau is associated with the very dense axonal microtubule network of neurons and conventional light microscopy approaches cannot fully resolve its nanoscale composition due to the diffraction limit of spatial resolution in light microscopy. In conventional microscopy images, microtubule-associated tau is seen to fully occupy the tubulin polymer demonstrating a uniform distribution (Agostini et al. 2013). However, these images can be misleading as the resolving power is not sufficient to determine the distribution of the tau protein as individual tau molecules are smaller than 200 nm, which is the approximate resolution limit of these approaches.

Single-molecule localization microscopy (SMLM) approaches can exceed the resolution limit of conventional light microscopy approaches often reaching down to 20nm spatial resolution (Lelek et al. 2021) (Betzig et al. 2006) (Hess, Girirajan, and Mason 2006) (Rust,

Bates, and Zhuang 2006) (Heilemann et al. 2008). One such approach is known as STochastic Optical Reconstruction Microscopy or STORM (Rust, Bates, and Zhuang 2006). STORM typically uses fixed samples which are stained with photoswitchable fluorophores and imaged in a special buffer. The buffer contains thiols such as Cysteamine (also known as MEA), which are necessary for photoswitching. Additionally, the buffer contains an oxygen scavenger system, specifically glucose oxidase and catalase, which is important for reducing photobleaching (Lelek et al. 2021). This STORM buffer in combination with the photoswitchable molecules in the sample allow some molecules to stochastically activate, while the rest are in a dark state. Once a molecule is stochastically activated, its centroid position can be localized with nanoscale precision. Once all molecules in the sample have been activated, the resulted reconstructed image or STORM image containing localizations from all the fluorescent molecules in the sample is produced (Fig. 1.2). The localizations in the image can then be rendered with a Gaussian blur for visualization purposes and analyzed further with several quantitative approaches (Lelek et al. 2021).
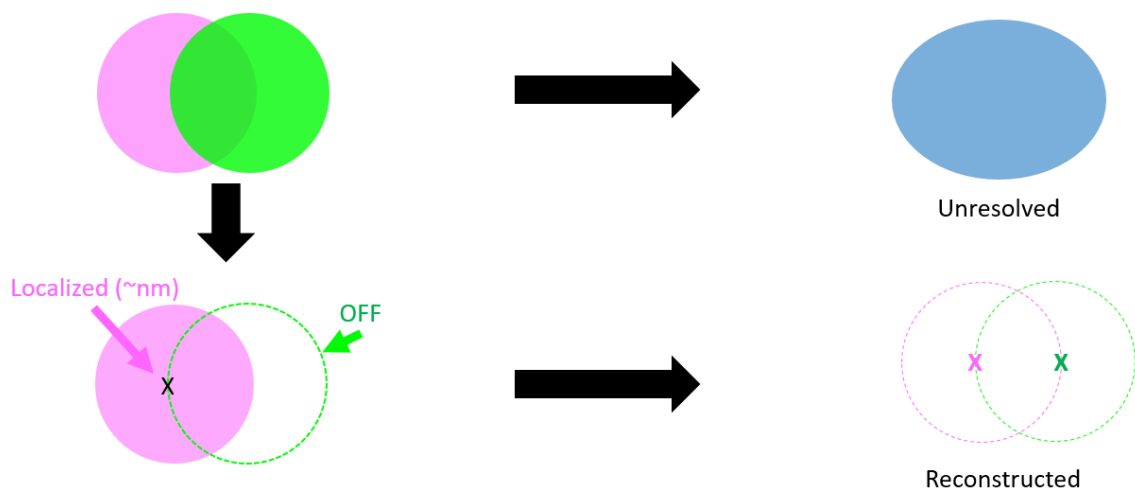
Figure 1.2: STORM imaging

The two fluorophores (magenta and green circles) on the left cannot be resolved due to the diffraction limit and instead appear as the unresolved blob on the right (blue). In STORM, during the blinking phase of the photoswitchable molecules, the fluorophore on the left (magenta) can be stochastically activated while the molecule on the right (green) is in an off state. Once all molecules have been activated a reconstructed STORM image (bottom right) is obtained.

In this work, we have used a combination of STORM and machine learning to study i) the nanoscale composition of tau on microtubules and in tau aggregates, and ii) which tau aggregate species are degraded by UPS versus autophagy. More specifically, in Chapter 2, I will show how we tested the hypothesis that tau has a non-uniform distribution on the microtubules and that this distribution is different when tau is aggregated. In Chapter 3, I will show how we tested whether different tau aggregate species have prominent phosphorylation markers. In Chapter 4, I will discuss how UPS and autophagy differentially degrade different tau aggregate species. Finally, in Chapter 5, I will summarize our findings and provide future directions for our work.

CHAPTER 2. TAU FORMS OLIGOMERIC COMPLEXES ON MICROTUBULES THAT ARE DISTINCT FROM TAU AGGREGATES

Adapted from article published as: Gyparaki, M. T., Arab, A., Sorokina, E. M., Santiago-Ruiz, A. N., Bohrer, C. H., Xiao, J. and Lakadamyali, M. (2021). Tau forms oligomeric complexes on microtubules that are distinct from tau aggregates. *PNAS*, 118, e2021461118 (19). PNAS authors do not need permission to include their articles as part of their dissertation.

Introduction

Tau is a microtubule-associated protein mainly expressed in neurons. Tau is an intrinsically disordered protein, which facilitates the assembly and stability of neuronal microtubules. Immunofluorescence labeling showed that tau is highly abundant in neuronal axons and shows a graded distribution with higher concentration toward the axon terminal (Weissmann et al. 2009). Tau binding is thought to stabilize neuronal microtubules, although this idea has recently been called into question, and recent work suggests that tau may bind the more labile part of microtubules, enabling them to have long labile domains (Qiang et al. 2018). The first near-atomic model of tau bound to microtubules obtained using cryogenic electron microscopy (cryo-EM) and computational modeling revealed that tau binds along the microtubule protofilament, stabilizing the interface between tubulin dimers (Kellogg et al. 2018). Tau has also been shown to undergo liquid–liquid phase separation *in vitro*, and tau condensates have been proposed to facilitate microtubule polymerization due to their ability to sequester soluble tubulin (Wegmann et al. 2018). *In vitro* reconstitution experiments further showed that tau forms

liquid condensates that are several microns in size on taxol-stabilized microtubules, and these tau "islands" regulate microtubule severing and microtubule–motor protein interactions (R. Tan et al. 2019) (Siahaan et al. 2019). However, despite progress, the distribution of tau on microtubules in intact cells and the physiological relevance of tau condensates are unclear.

Under pathological conditions, tau becomes hyperphosphorylated and detaches from microtubules, leading to the misfolding and formation of tau aggregates in the cytosol (Grundke-Iqbal et al. 1986). Accumulation of tau into insoluble aggregates known as neurofibrillary tangles (NFTs) is a hallmark of several neurodegenerative diseases such as Alzheimer's disease (AD) and frontotemporal dementia with parkinsonism linked to chromosome 17 (FTDP-17), which are collectively known as tauopathies. Liquid phase separation has also been suggested to play a role in pathological tau aggregation, as aggregation-prone tau mutants have an increased propensity to undergo liquid phase separation (Wegmann et al. 2018). Recently, cryo-EM studies have also revealed the high-resolution structures of insoluble tau aggregates, including paired helical filaments (PHF) and straight filaments (SFs) from AD brain (Fitzpatrick et al. 2017). While these insoluble aggregates such as PHFs, SFs, and NFTs have traditionally been considered the pathological tau species, recent evidence from animal models has shown that neurodegeneration in terms of synaptic dysfunction and behavioral abnormalities can exist without the presence of NFTs (Wittmann et al. 2001) (Cowan et al. 2010).

The current hypothesis is that earlier stages of tau aggregation initiate pathology. In particular, small, soluble tau oligomeric species preceding the formation of NFTs could be the cause of loss of tau function and toxicity. Soluble tau oligomers have been isolated

from homogenized AD brains and detected on sodium dodecyl sulfate–polyacrylamide gel electrophoresis gels (Patterson et al. 2011). These tau oligomers have also been implicated in synaptic loss in transgenic mice expressing wild-type human tau (Spires et al. 2006) (Berger et al. 2007) (Clavaguera et al. 2013). Moreover, injection of tau oligomers rather than monomers or fibrils into the brain of wild-type mice was sufficient to produce cognitive and synaptic abnormalities (Lasagna-Reeves et al. 2011) (Castillo-Carranza et al. 2014). Tau oligomers can lengthen and adopt a β-sheet conformation, which renders them detergent insoluble. Such oligomers have granular appearance under atomic force microscopy (AFM) (Takashima 2013).

Despite their *in vitro* characterization, to date, there have not been studies visualizing and characterizing the formation of these small oligomers in intact cells due to the lack of quantitative, high-resolution tools. The lack of sensitive tools that enable visualizing the spatial distribution and quantifying the stoichiometry of tau complexes within native and diseased neurons prevents progress in studying the mechanisms that lead to pathological tau oligomerization and the impact of early stages of tau aggregation on cellular processes.

Here, we have used quantitative super-resolution microscopy to visualize and determine the nanoscale organization of tau in various engineered cells modeling the nonaggregated state of tau (QBI-293 Clone 4.0 cells expressing 4R-P301L-GFP tau, BSC-1 cells expressing 3R-WT-GFP tau, and BSC-1 cells expressing 4R-WT-GFP tau) (J. L. Guo et al. 2016) as well as in rat hippocampal neurons. In addition, using an engineered cell model expressing tau harboring the FTDP-17 mutation P301L and transduced with exogenous tau fibrils to mimic tau aggregation in disease (QBI-293 Clone 4.1 cells

expressing 4R-P301L-GFP tau) (J. L. Guo et al. 2016), we characterized the nature of tau aggregates including oligomeric tau species. Surprisingly, our results show that, in engineered cell lines modeling a nonaggregated state of tau, tau forms a patchy distribution consisting of nanoclusters along the microtubule. Tau nanoclusters mainly correspond to monomeric, dimeric, and trimeric tau complexes. The nanoscale distribution of microtubule-associated tau in these engineered cells resembles the nanoscale distribution of microtubule-associated endogenous tau in hippocampal neurons isolated from rats. In engineered cell lines modeling an aggregated state of tau (QBI-293 Clone 4.1), tau forms a diverse range of aggregate species, including small oligomeric tau assemblies, small fibrillary structures, branched fibrils, and large plaque-like structures resembling NFTs. The oligomeric species found in the aggregated tau cell model are partially microtubule associated and are distinct from the monomers, dimers, and trimers found in the nonaggregated cell models and in neurons, since they are larger, containing more tau molecules.

Overall, we present a detailed, quantitative characterization of tau oligomers on microtubules in intact cells and of tau aggregates with nanoscale resolution in a cell model of FTDP-17.

Results

Microtubule-Associated Tau Is Partially Oligomeric under Nonaggregated Conditions.

To determine how tau is distributed when it is associated to microtubules under nonaggregated conditions, we performed single-molecule localization microscopy (SMLM) in various engineered cell models: a stable BSC-1 cell line that constitutively

expresses the 3R isoform of wild-type (WT) tau fused to green fluorescent protein (GFP; BSC-1 3R-WT-GFP tau), BSC-1 cells transiently expressing the 4R isoform of WT tau fused to GFP (BSC-1 4R-WT-GFP tau), and an inducible QBI-293 cell line that stably expresses GFP-tagged tau harboring a FTDP-17 mutation (P301L) under the control of doxycycline (Dox) (QBI-293 Clone 4.0 4R-P301L-GFP tau, referred to as Clone 4.0 in the rest of the manuscript). The pattern of GFP expression in all the engineered cell lines we imaged resembles the microtubule network (*SI Appendix A*, Fig. A1A), indicating that tau is predominantly microtubule associated in all cases as expected. Additionally, we transiently expressed the 4R-WT tau (without GFP fusion) in BSC-1 cells and detected tau localization using immunofluorescence labeling with a Tau-5 antibody. The 4R-WT tau formed a microtubule-associated pattern in cells similar to the GFP-fused 4R-WT tau (*SI Appendix A*, Fig. A1A). Hence, GFP-fused tau is able to bind microtubules in cells.

Since these engineered cell lines do not endogenously express tau or express it at very low levels (*SI Appendix A*, Fig. A1B), using the inducible Clone 4.0 cells as the model, we asked whether when tau expression is induced by Dox, the binding of tau to the microtubules impacts the microtubule network. To address this question, we imaged the microtubule network in Clone 4.0 before and after Dox induction using SMLM. As expected, tau expression led to increased microtubule density and microtubule bundling in line with the known functions of tau in facilitating microtubule polymerization and bundling (*SI Appendix A*, Fig. A1 C, *Top* and *Middle* and *SI Appendix A*, Fig. A1D, first two plots) (Kanai, Chen, and Hirokawa 1992) (Fauquant et al. 2011). These results further support that GFP-fused tau is able to induce microtubule polymerization and bundling.

We next labeled 4R-P301L-GFP tau (Fig. 2.1A and additional representative images in *SI Appendix A*, Fig. A2A), 3R-WT-GFP tau (Fig. 2.1B), and 4R-WT-GFP tau (*SI Appendix A*, Fig. A2B) in the corresponding cell models with a GFP nanobody conjugated with a photoswitchable fluorescent dye (AF647) to image tau's nanoscale distribution with SMLM. To ensure that fixation did not perturb tau localization, we tested two commonly used fixation protocols using either aldehyde-based fixation (paraformaldehyde, PFA) or alcohol-based fixation (methanol) (*SI Appendix*, *Materials and Methods*). PFA fixation led to a mislocalization of tau and loss of "microtubule-like" staining visible in live cells (*SI Appendix A*, Fig. A3A) in line with previous reports (Ebneth et al. 1998) (Illenberger et al. 1998). Methanol fixation, on the other hand, preserved the microtubule localization of tau (*SI Appendix A*, Fig. A3A). Indeed, when we determined the fluorescence intensity of microtubule-associated 4R-P301L-GFP tau in the same Clone 4.0 cells before and after methanol fixation, the fluorescence intensity was only reduced by a small amount (mean intensity: 871.2 AU before and 750.1 AU after fixation), suggesting that the majority of tau remains microtubule bound after fixation (*SI Appendix A*, Fig. A3B). Hence, we used methanol fixation for visualizing tau's nanoscale organization.
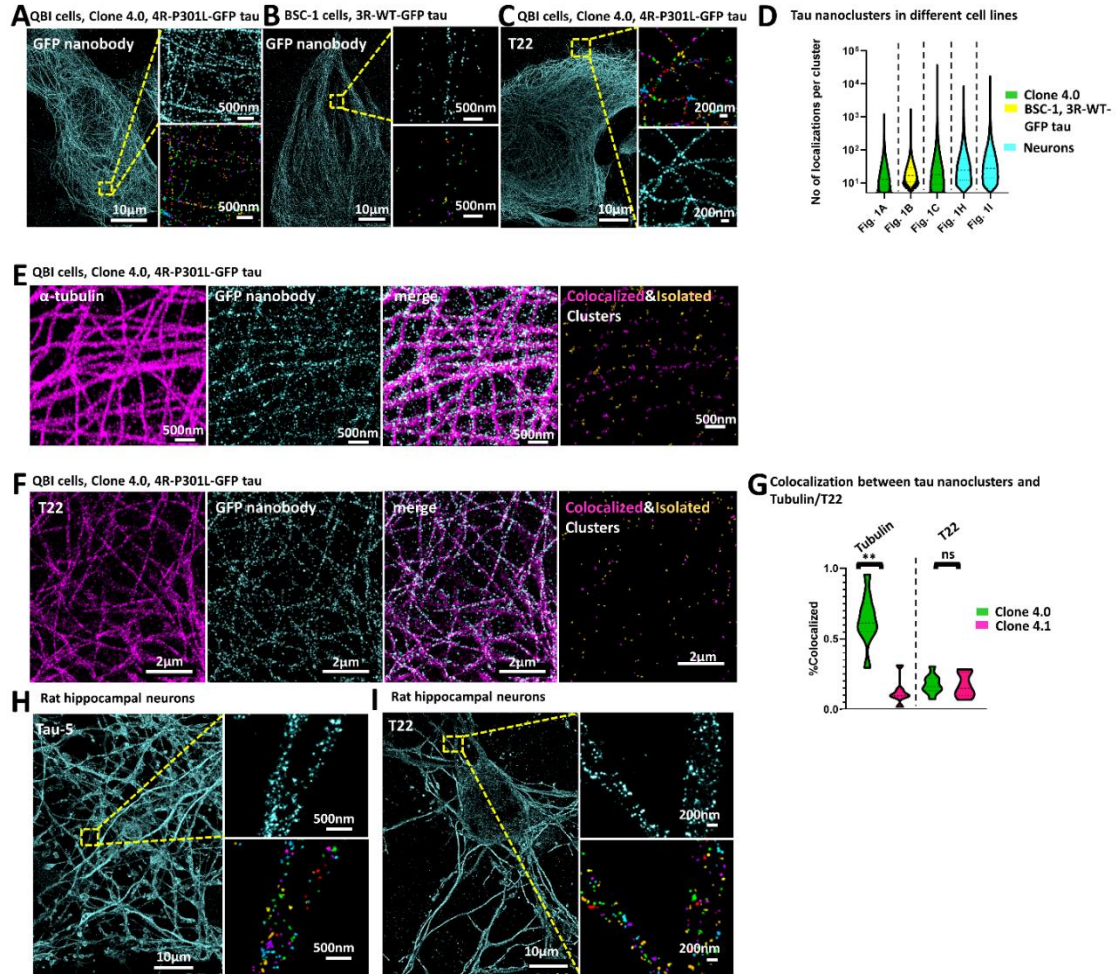
Figure 2.1: Microtubule-associated tau is partially oligomeric under nonaggregated conditions

A. Super-resolution image of tau in Clone 4.0 cells expressing 4R-P301L-GFP tau stained with GFP nanobody conjugated to Alexa Fluor 647 after overnight Dox induction of tau expression. (Inset) Pictured together with corresponding Voronoi segmentation. Segmented images are pseudo color coded with different colors corresponding to different segmented nanoclusters. B. Super-resolution image of tau in stable BSC-1 cells constitutively expressing 3R-WT-GFP tau stained with GFP nanobody conjugated to Alexa Fluor 647. (Inset) Pictured together with corresponding Voronoi segmentation. Segmented images are pseudo color coded with different colors corresponding to different segmented nanoclusters. C. Super-resolution image

of oligomeric tau detected by the tau oligomer-specific T22 antibody in Clone 4.0 cells expressing 4R-P301L-GFP tau after overnight Dox induction of tau expression. (Inset) Pseudo color-coded Voronoi segmentation of nanoclusters. D. Violin plots showing the number of localizations per nanocluster segmented with Voronoi segmentation in the different cell lines used in this study (green: Clone 4.0 cells expressing 4R-P301L-GFP tau after overnight Dox induction of tau expression; yellow: stable BSC-1 cells constitutively expressing 3R-WT-GFP tau; and cyan: rat hippocampal neurons). Plots for A and B correspond to the quantification of tau nanoclusters stained and imaged with a GFP nanobody. Plot for H corresponds to the quantification of tau nanoclusters stained and imaged with a Tau-5 antibody. Plots for C and I correspond to the quantification of tau nanoclusters stained and imaged with the oligomeric T22 antibody. The dashed lines indicate the median, and the dotted lines indicate the 25th and 75th percentile. (A) n = 15 cells, n = 3 experiments. (B) n = 15 cells, n = 2 experiments. (C) n = 19 cells, n = 3 experiments. (H) n = 3 cells. (I) n = 3 cells. E. Two-color super-resolution images of α-tubulin (magenta), total tau (cyan), and overlay in Clone 4.0 cells expressing 4R-P301L-GFP tau after overnight Dox induction of tau expression. The results of the colocalization analysis are shown in which tau nanoclusters colocalized with α-tubulin are color coded in magenta, and isolated tau nanoclusters are shown in yellow. F. Two-color super-resolution images of oligomeric tau detected by tau oligomer-specific T22 antibody (magenta), total tau (cyan), and overlay in Clone 4.0 cells expressing 4R-P301L-GFP tau after overnight Dox induction of tau expression. The results of the colocalization analysis are shown in which tau nanoclusters colocalized with T22 are color coded in magenta, and isolated tau nanoclusters are shown in yellow. G. Violin plots showing the percentage of tau nanoclusters colocalized with α-tubulin and T22 antibodies in Clone 4.0 cells expressing 4R-P301L-GFP tau after overnight Dox induction of tau expression (green) and Clone 4.1 cells maintained in Dox and expressing 4R-P301L-GFP tau (pink). (Tubulin in Clone 4.0: n = 9 cells, n = 2 experiments; Tubulin in Clone 4.1: n = 7 cells, n = 2 experiments; T22 in Clone 4.0: n = 9 cells, n = 3 experiments; T22 in Clone 4.1: n = 6 cells, n = 2 experiments). H. Super-resolution image of

tau in rat hippocampal neurons, stained with Tau-5 antibody, which detects all tau isoforms. (Inset) Pictured together with corresponding Voronoi segmentation. Segmented images are pseudo color coded with different colors corresponding to different segmented nanoclusters. I. Super-resolution image of oligomeric tau detected by oligomer tau-specific T22 antibody in rat hippocampal neurons. (Inset) Pseudo color-coded Voronoi segmentation of nanoclusters.

SMLM images revealed that both 3R (Fig. 2.1B) and 4R (*SI Appendix A*, Fig. A2B) isoforms of WT tau as well as the 4R isoform harboring the P301L mutation (Fig. 2.1A and *SI Appendix A*, Fig. A2A) are not uniformly distributed on the microtubule, unlike α-tubulin (compare Fig. 2.1 A and B and *SI Appendix*, Figs. A2A and B and A3C), but instead form nanoclusters. We segmented these nanoclusters using Voronoi tessellation (Levet et al. 2015) (Andronov et al. 2016) (Fig. 2.1A and B and *SI Appendix A*, Fig. A3D and *Materials and Methods*) and quantified the number of localizations per nanocluster (Fig. 2.1D) (corresponding to the number of times an AF647 fluorophore was localized) as well as the nanocluster area (*SI Appendix A*, Fig. A3E), obtaining a broad distribution in all cases. These parameters were similar for 3R-WT-GFP tau in stable BSC-1 cells and 4R-P301L-GFP tau in Clone 4.0 cells, despite vast differences in expression level between 3R-WT-GFP tau and 4R-P301L-GFP tau (fivefold difference in expression, *SI Appendix A*, Fig. A3F). Furthermore, when we compared low and high GFP tau-expressing BSC-1 cells transiently expressing the same tau construct (4R-WT-GFP tau) and cultured in the same way (*SI Appendix A*, Fig. A3G, threefold difference in expression), we found that tau formed nanoclusters in both high- and low-expressing cells. Tau nanoclusters further contained only a slightly higher number of localizations in high-expressing cells compared to the low-expressing cells (median: 13 ± 36.58 for low-expressing cells versus median: 15 ± 59.98 for high-expressing cells, *SI Appendix A*, Fig.

A3H). Previous work showed that 4R-P301L tau in Clone 4.0 cells remains soluble and does not form insoluble tau inclusions for up to 2 d after Dox induction (J. L. Guo et al. 2016). To determine the impact of the duration of Dox induction on tau nanocluster formation, we cultured and imaged Clone 4.0 cells for 1 or 2 d after Dox induction and found that tau nanoclusters were similar for these time points (*SI Appendix A*, Fig. A3I). Taken together, these results suggest that tau nanocluster formation does not strongly depend on the type of tau isoform or the method of tau expression (transient, stable/constitutive, or stable/inducible) and is only weakly dependent on the level of tau expression. Since tau distribution was similar between two isoforms of WT tau and tau harboring the P301L mutation, we used the inducible 4R-P301L-GFP tau Clone 4.0 cell line for subsequent analysis.

To determine the monomeric versus oligomeric nature of tau within these nanoclusters, we used a number of different approaches. In principle, the number of localizations per nanocluster in SMLM images is proportional to the number of proteins. However, repeated fluorophore blinking and the fact that the labeling ratio between the protein and the fluorophore is often not one to one typically leads to overcounting artifacts (Durisic, Cuervo, and Lakadamyali 2014).

First, to exclude the possibility that these are artificial nanoclusters resulting from repeated blinking of the same fluorophore, we used Distance Distribution Correction (DDC) (Bohrer et al. 2019) to eliminate multiple localizations from the same molecule. Although DDC narrowed down the distribution of GFP tau nanocluster areas and the number of localizations per cluster (*SI Appendix A*, Fig. A4 A–C), the distributions still remained broad. Importantly, DDC correction did not eliminate the presence of nanoclusters (*SI*

Appendix A, Fig. A4A), suggesting that these are not artificial nanoclusters due to repeated fluorophore blinking.

Second, we used a commercial oligomeric tau antibody (T22) to specifically stain oligomeric tau. SMLM images of tau labeled with the T22 antibody revealed a discontinuous microtubule-like pattern, suggesting that the oligomeric T22 antibody binds to microtubule-associated tau (Fig. 2.1C and additional representative images in *SI Appendix A*, Fig. A2C).

Taken together, our analyses suggested that observed tau nanoclusters contain oligomeric tau molecules associated with microtubules. To estimate the number of tau molecules in these nanoclusters, we next used a method that we previously developed to estimate the stoichiometry of proteins in super-resolution images using the number of localizations distribution from the monomeric protein images as a calibration (Cella Zanacchi et al. 2017). To determine the number of localizations distribution corresponding to the monomeric protein, we performed a 100-fold dilution of the GFP nanobody to sparsely label individual tau molecules instead of saturating all GFP epitopes. This approach has previously been successfully used to calibrate antibody-labeled receptors to determine their stoichiometry within synapses (Ehmann et al. 2014). The resulting images under dilute labeling conditions showed "nanoclusters" that were much sparser than those in densely labeled cells (*SI Appendix A*, Fig. A4D). Nanoclusters under dilute labeling conditions also contained a significantly lower number of localizations compared to those in densely labeled cells (*SI Appendix A*, Fig. A4E). We assumed that the nanoclusters under sparse labeling conditions therefore mainly corresponded to monomeric tau and appeared as nanoclusters because of repeated blinking of the same

fluorophore. Indeed, DDC eliminated the appearance of nanoclusters (*SI Appendix A*, Fig. A4F) and Voronoi segmentation of DDC-corrected images did not detect any nanoclusters under dilute labeling conditions. Using the distribution of the number of localizations per nanocluster prior to DDC correction under dilute labeling conditions as a calibration (*SI Appendix*, *Materials and Methods*), we determined that tau nanoclusters in the densely labeled 4R-P301L-GFP tau Clone 4.0 cells contain ~60% monomers, ~20% dimers, and ~20% trimers (*SI Appendix A*, Fig. A4 G and H). Tau nanoclusters in the BSC-1 cells stably expressing 3R-WT-GFP tau consisted of ~60% monomers, ~25% dimers, and ~15% trimers, which is very similar to the percentages determined in the 4R-P301L-GFP tau Clone 4.0 cell line (*SI Appendix A*, Fig. A4I).

To further support these results, we labeled tau together with α-tubulin or with T22 and carried out two-color SMLM (Fig. 2.1 E and F). We used the images of microtubules or of oligomeric tau labeled with T22 antibody as a mask and categorized the tau nanoclusters into two populations: those that colocalize with the reference mask and those that are isolated (*SI Appendix A*, *Materials and Methods* and Fig. 2.1 E and F). Approximately 61 ± 19% of the GFP tau nanoclusters were microtubule associated (Fig. 2.1G). Similarly, ~20 ± 7% of GFP tau nanoclusters colocalized with T22-stained tau oligomers (Fig. 2.1G). A positive control experiment in which we labeled GFP tau with nanobodies in two colors and carried out colocalization analysis showed ~60 ± 13% colocalization under conditions in which we expect full colocalization (*SI Appendix A*, Fig. A5A), consistent with previous two-color super-resolution results(Spiess et al. 2018). Hence, our two-color imaging and colocalization analysis underestimates the true extent of colocalization by ~1.7-fold, suggesting that tau is almost exclusively microtubule associated in Clone 4.0, and ~34%

of tau colocalizes with T22. The latter number is in line with our calibration and stoichiometry estimation showing ~40% tau dimers/trimers in Clone 4.0.

Finally, to confirm that the nanoclusters are not due to overexpression of the GFP fusion protein in the engineered cell lines, we stained endogenous tau in hippocampal neurons, which mainly express the 3R isoform of tau (Fuster-Matanzo et al. 2012), with a total tau antibody, Tau-5 (Fig. 2.1H and additional representative images in *SI Appendix A*, Fig. A2D) as well as T22 (Fig. 2.1I and additional representative images in *SI Appendix A*, Fig. A2E). We obtained similar results in which tau formed nanoclusters containing a wide distribution of a number of localizations that are recognized by the oligomeric tau T22 antibody (quantified in Fig. 2.1D and *SI Appendix A*, Fig. A3E). We repeated the dilute labeling experiments by lowering the concentration of the primary Tau-5 antibody by 100-fold while keeping the secondary antibody concentration at the same level in neurons. Under dilute primary antibody labeling conditions, we obtained sparse nanoclusters containing significantly fewer localizations and likely corresponding to monomeric tau similar to the nanobody experiments (*SI Appendix A*, Fig. A4J). These results indicate that tau oligomers are also present in physiological conditions in cultured neurons and are not an artifact of GFP fusion.

Based on these results, we concluded that under physiological conditions in neurons and under nonaggregated conditions in engineered cell lines, tau is primarily microtubule associated, and a proportion of tau that is associated with microtubules forms dimeric and trimeric complexes.

Tau Oligomers in Cells Exhibiting Tau Aggregation Are Distinct from Tau Oligomers in Nonaggregated Tau Cell Models.

To determine the nanoscale distribution and composition of tau aggregates, we used an engineered cell line modeling tau aggregation: QBI-293 Clone 4.1 cells expressing 4R-P301L-GFP tau under Dox control, which we will refer to as Clone 4.1 cells. Clone 4.1 is a subclone of Clone 4.0 and was obtained after exogenously transducing the parent clone (Clone 4.0) with *in vitro* reconstituted tau fibrils to induce tau aggregation and selected because it stably maintains tau aggregates when cultured in the presence of Dox (J. L. Guo et al. 2016). Western blot analysis showed that Clone 4.1 expresses tau at slightly lower levels than Clone 4.0 (*SI Appendix A*, Fig. A1B), and hence, the tau aggregation seen in Clone 4.1 is not a result of higher tau expression levels but instead is seeded by the exogenously introduced tau fibrils.

Previous work using this subclone showed that it recapitulates the tau aggregation seen in disease states, such as formation of large tau inclusions resembling NFTs (J. L. Guo et al. 2016). Furthermore, it was shown that when tau expression is stopped by culturing the Clone 4.1 cells off Dox, tau aggregates are cleared via lysosomal degradation (J. L. Guo et al. 2016). These previous results suggest that Clone 4.1 is a good model system for pathological tau aggregation and for gaining new insights into mechanisms of tau aggregation and clearance *ex vivo*. SMLM images of tau in Clone 4.1 (Fig. 2.2A and additional representative examples in *SI Appendix A*, Fig. A6) were dramatically different from those of Clone 4.0 (Fig. 2.1A and *SI Appendix A*, Fig. A2A). While a small population of microtubule-associated tau remained, there was a large population of cytosolic tau aggregates having diverse sizes and shapes.

The resulting Voronoi-segmented objects ranged from small nanoclusters, similar to those observed in nonaggregated tau cell models and neurons, to fibrillary structures and large conglomerate aggregates that are reminiscent of NFTs in terms of their size (Fig. 2.2A). The number of localizations per segmented object (Fig. 2.2B) and the area of the segmented objects (*SI Appendix A*, Fig. A5B) were very broad and on average higher compared to the nanoclusters in Clone 4.0, in line with the visual impression of the presence of a wide range of aggregate structures.
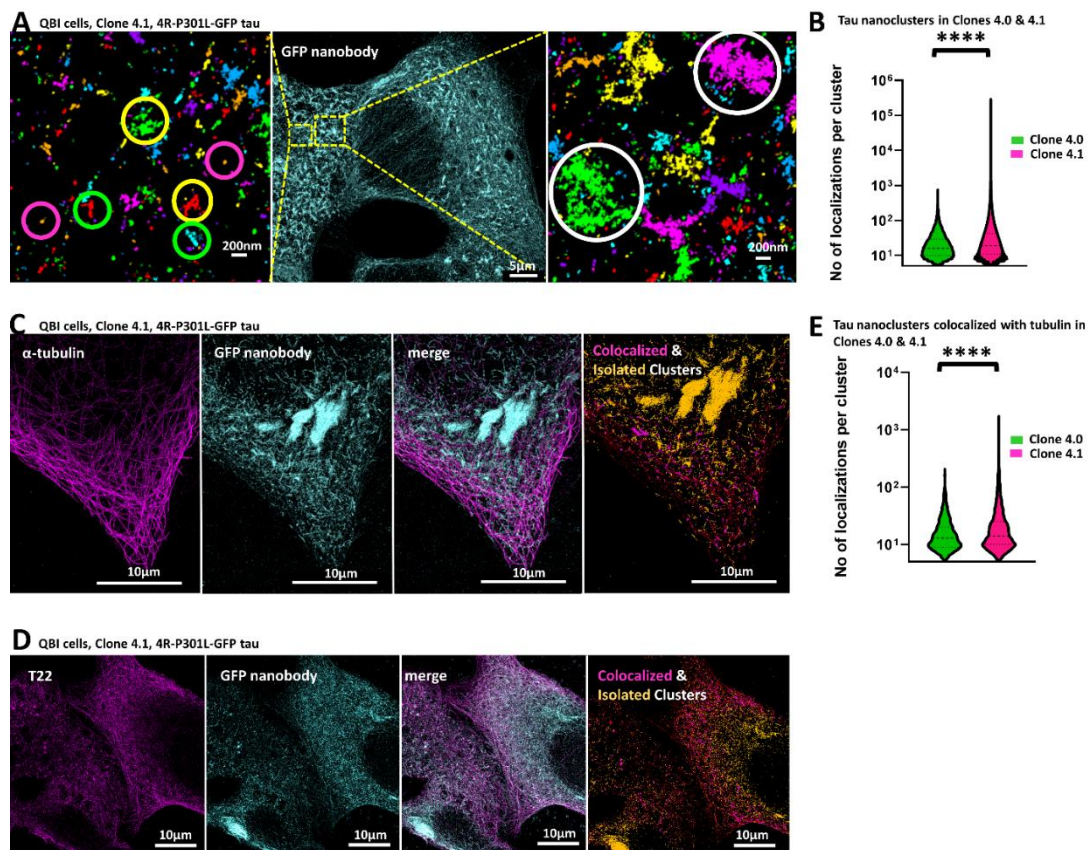
Figure 2.2: Tau oligomers in cells harboring tau aggregates are distinct from tau oligomers in cells modeling a nonaggregated tau state.

A. Super-resolution image of tau in Clone 4.1 cells maintained in Dox and expressing 4R-P301L-GFP tau. Zoomed in regions after Voronoi segmentation are shown. Segmented images are pseudo color coded with different colors corresponding to different segmented objects. Nanoclusters (magenta circles), fibrillary structures (green circles), branched fibrils (yellow circles), and conglomerate NFT-like structures (white circles) are visible in the segmented images. B. Violin plots showing the number of localizations per Voronoi-segmented tau nanocluster in Clone 4.0 cells expressing 4R-P301L-GFP tau after overnight Dox induction of tau expression (green) and Voronoi-segmented tau object in Clone 4.1 cells maintained in Dox and expressing 4R-P301L-GFP tau (pink). The dashed lines indicate the median, and the dotted lines indicate the 25th and 75th percentile (Clone 4.0: n = 15 cells, n = 3 experiments; Clone 4.1: n = 20 cells, n = 3 experiments). ****$P < 0.0001$. C. Two-color super-resolution images of α-tubulin (magenta), total tau (cyan), and overlay in Clone 4.1 cells maintained in Dox and expressing 4R-P301L-GFP tau. The results of the colocalization analysis are shown in which tau aggregates colocalized with α-tubulin are color coded in magenta, and isolated aggregates are shown in yellow. D. Two-color super-resolution images of oligomeric tau detected by tau oligomer-specific T22 antibody (magenta), total tau (cyan), and overlay in Clone 4.1 maintained in Dox and expressing 4R-P301L-GFP tau. The results of the colocalization analysis are shown in which tau aggregates colocalized with T22 are color coded in magenta, and isolated aggregates are shown in yellow. E. Violin plots showing the number of localizations per Voronoi-segmented tau nanocluster that colocalizes with α-tubulin in Clones 4.0 cells expressing 4R-P301L-GFP tau after overnight Dox induction of tau expression (green) and Clone 4.1 cells maintained in Dox and expressing 4R-P301L-GFP tau (pink). The dashed lines indicate the median and the dotted lines indicate the 25th and 75th percentile (4.0: n = 9 cells, n = 2 experiments; 4.1: n = 7 cells, n = 2 experiments). ****$P < 0.0001$.

To once again determine the percentage of oligomeric tau and the amount of cytosolic versus microtubule-associated tau present in these aggregated tau cells, we performed two-color SMLM. We labeled tau together with α-tubulin (Fig. 2.2C) or with T22 (Fig. 2.2D)

and performed the colocalization analysis. The percentage of microtubule-associated tau in Clone 4.1 (~10 ± 9% uncorrected or ~17% corrected based on the colocalization positive control) was significantly lower than that in Clone 4.0 (~61% uncorrected and 100% corrected) (Fig. 2.1G). However, similar to Clone 4.0, ~20 ± 9% of tau (~34% corrected) colocalized with the oligomeric T22 antibody (Fig. 2.1G). The large tau aggregates reminiscent of neurofibrillary tangles were clearly excluded from microtubules and also did not colocalize with T22 (Fig. 2.2 C and D). The number of localizations per microtubule-associated tau object was higher in Clone 4.1 than that for the nanoclusters in Clone 4.0, suggesting that there are small tau aggregates that remain on the microtubule (Fig. 2.2E). To further confirm this result, we next used the calibration approach to determine the copy number composition of the oligomeric tau species in Clone 4.1 by fitting the distribution of the number of localizations to the calibration function obtained from the nanobody dilution experiment (*SI Appendix A*, Fig. A5C). The distribution of the number of localizations for Clone 4.1 is highly skewed with a long tail corresponding to the presence of a diverse range of large aggregates containing a high number of localizations. We therefore focused on fitting the part of the curve corresponding to smaller aggregates, including nanoclusters and small fibrils. This analysis showed that the copy number of tau within these small aggregates ranged between one to seven tau molecules. Interestingly, the percentage of monomeric tau was similar in Clone 4.0 and Clone 4.1, whereas the percentage of dimers and trimers decreased, and the percentage of higher-order oligomers increased in Clone 4.1 compared to Clone 4.0. These results suggest that the dimers and trimers may seed the formation of the higher-order oligomers consisting of greater than three tau proteins during tau aggregation.

We next asked if tau aggregation had any impact on the integrity of the microtubule network. To address this question, we imaged the microtubule network in Clone 4.1 cells using SMLM. Surprisingly, tau aggregation led to a disruption of the microtubule network, leading to significantly less dense microtubules in Clone 4.1 compared to Clone 4.0 both with (+Dox) and without (−Dox) tau (*SI Appendix A*, Fig. A1 C and D, *Bottom*, third plot). This finding suggests that tau aggregates have an adverse effect on the microtubule network integrity. Overall, our results show the presence of oligomers consisting of greater than three tau proteins in cells harboring tau aggregates that are not present under nonaggregated conditions and that remain partially microtubule associated, in addition to a diverse range of larger tau aggregates that together disrupt the integrity of the microtubule network in a cell model of FTDP-17.

Discussion

By using cell models in which tau is either predominantly microtubule associated or tau is aggregated, we demonstrated using super-resolution microscopy that tau forms small oligomers—mostly dimers and trimers—on microtubules, which are distinct from tau aggregates. The distribution of tau on microtubules in cell models representing the nonaggregated state of tau (BSC-1 cells expressing 3R-WT-GFP tau and 4R-WT-GFP tau as well as QBI-293 Clone 4.0 cells expressing 4R-P301L-GFP tau) and in hippocampal neurons is not uniform, but instead, we showed that tau forms nanoclusters. Previous AFM and other *in vitro* studies have shown that P301L tau isolated from yeast (Vandebroek et al. 2006) and WT tau from rat (Makrides et al. 2003) form tau clusters and oligomers on taxol-stabilized microtubules, respectively. Furthermore, these previous studies showed that P301L tau causes microtubules to stick together and bend abnormally, which was not

the case for WT tau (Vandebroek et al. 2006). However, in the context of human tau expressed in mammalian cells and endogenous tau in neurons, we did not observe such microtubule abnormalities, and both WT and P301L tau formed nanoclusters.

Most recently, *in vitro* studies described the formation of physiological tau condensates (R. Tan et al. 2019) also called tau "cohesive islands" (Siahaan et al. 2019) on microtubules. In both cases, these tau structures were shown to undergo liquid–liquid phase separation, and the size of the condensates was in the micrometer range. The nanoclusters we observe are much smaller than these liquid condensates that form *in vitro*; instead, microtubule-associated tau inside cells mainly consists of small tau complexes including monomers, dimers, and trimers. Historically, tau oligomerization has been mostly deemed a pathological feature of tau. However, our findings show that endogenous tau can form small oligomers under physiological conditions in neurons. It has been speculated that an electrostatic zipper resulting from anti-parallel alignment of N-terminal halves of two tau molecules may be mediating tau dimerization (Rosenberg et al. 2008). Since tau is a highly disordered protein, it would be interesting to explore how it could form oligomers on microtubules.

Future studies exploring the relationship between different tau isoforms/mutants and oligomer formation as well as investigating whether tau isoforms/mutants that do not form oligomers are resistant to aggregation would bring exciting new insights into the mechanisms of physiological and pathological tau oligomerization. From an evolutionary point of view, protein dimerization/oligomerization is a commonly used mechanism of functional regulation for many proteins, as it promotes protein complex formation in physiological settings rather than just in pathology (Marianayagam, Sunde, and Matthews

2004). Our findings therefore bring up interesting questions regarding the physiological function of tau oligomers, which should be subject of future studies. They can potentially mediate microtubule bundling as well as interact with and regulate the function of microtubule motors and severing enzymes as suggested in previous *in vitro* studies (Dixit et al. 2008) (R. Tan et al. 2019) (Siahaan et al. 2019).

Introducing tau oligomers into the brain of WT rodents has resulted in synaptic and memory dysfunction, supporting the hypothesis that tau oligomers are toxic (Fá et al. 2016) (Ondrejcak et al. 2018). Moreover, introducing tau oligomers directly into mammalian neurons using patch clamp electrodes also modified synaptic transmission and blocked events that could be underlying memory storage (Hill et al. 2019). Overexpression of human tau in a mouse N2A cell model also led to the formation of tau oligomers, which could be detected with immuno-electron microscopy and super-resolution microscopy as clusters associated to the plasma membrane (Merezhko et al. 2018). These tau clusters were shown to be secreted via an unconventional secretion pathway (Merezhko et al. 2018). Hence, tau oligomers likely also play an important role in propagation of tau pathology between neuronal cells. Here, we showed that in cells in which tau has undergone aggregation, the proportion of tau monomers was similar to cells lacking tau aggregation, but the proportion of dimers/trimers decreased, and higher-order oligomers appeared. This result, taken together with the result that tau forms small oligomers in hippocampal neurons, suggests that there is a distinction between small physiological tau oligomers and larger pathological tau oligomers.

Previous *in vitro* aggregation studies showed that tau dimers are the basic subunit of higher-order tau oligomers (Feinstein et al. 2016) and that tau dimerization is one

34

important rate-limiting step in the progression of tau aggregation (Friedhoff et al. 1998). These results are in line with our work, but here, we further demonstrate that tau dimers/trimers exist on microtubules prior to tau aggregation and therefore may be primed to template further aggregation in disease.

We showed that the majority of tau aggregates were excluded from microtubules. However, a small population of aggregated tau was found associated with microtubules, further suggesting that aggregation could be initiated from dimers/trimers present on microtubules. We further showed that tau aggregation negatively impacted the microtubule network itself. The density of the remaining microtubules in Clone 4.1 cells was lower than the basal conditions in Clone 4.0 cells (i.e., before the induction of tau aggregation). These results suggest that it is not just the dissociation of tau from the microtubule but the formation of tau aggregates that leads to microtubule disruption. It would be interesting to explore the mechanisms that lead to this microtubule network disruption and whether a specific tau aggregate species (oligomers or larger aggregates) leads to toxicity and the loss of microtubule integrity.

Overall, we present an approach based on super-resolution microscopy and quantitative analysis to characterize the distribution of tau in intact cells with nanoscale spatial resolution. Our approach opens the door for studying the mechanisms and kinetics of tau aggregation *in vivo*, the presence of early tau aggregates including pathological oligomers in disease, and screening for drugs that can potentially target and disrupt these pathological oligomers.

Materials and Methods

A detailed description of the methods can be found in *SI Appendix A*. Briefly, a stable cell line expressing 3R-WT-GFP tau was derived from African green monkey (*Cercopithecus aethiops*) kidney epithelial cells (BSC-1; CCL-26; American Type Culture Collection). For some experiments, BSC-1 cells were transfected with either a 4R-WT-GFP tau construct or a 4R-WT tau construct to transiently express tau (*SI Appendix*, Figs. S1A, S2B, and S3 G and H). In addition, two stable human embryonic kidney-derived QBI-293 cell lines (Clone 4.0, Clone 4.1) expressing full-length human tau T40 (2N4R or 4R) carrying the P301L mutation with a GFP tag, a kind gift from the V. Lee laboratory at the University of Pennsylvania, Philadelphia, PA, were used for experiments. Clone 4.1 is sorted from Clone 4.0 cells to enrich for large, compact tau aggregates after exogenous tau fibril addition. Clone 4.0 was cultured in Dox overnight (16 to 24 h) prior to fixation unless otherwise stated (reference *SI Appendix A*, Fig. A3I for different Dox timing experiments), whereas Clone 4.1 was maintained in Dox continuously. E18 Sprague Dawley rat hippocampal neurons were obtained in suspension from the Neuron Culture Service Center at the University of Pennsylvania. Cells were grown on chambered coverglass, fixed with ice cold methanol, and immunostained with appropriate antibodies prior to super-resolution microscopy using a Nanoimager from Oxford Nanoimaging.

CHAPTER 3. PHOSPHORYLATION OF SPECIFIC TAU RESIDUES IS ASSOCIATED WITH DIFFERENT TYPES OF HIGHER ORDER TAU AGGREGATE CLASSES

Adapted from article published as: Gyparaki, M. T., Arab, A., Sorokina, E. M., Santiago-Ruiz, A. N., Bohrer, C. H., Xiao, J. and Lakadamyali, M. (2021). Tau forms oligomeric complexes on microtubules that are distinct from tau aggregates. *PNAS*, 118, e2021461118 (19). PNAS authors do not need permission to include their articles as part of their dissertation.

Introduction

Tau is a microtubule-associated protein whose activity is regulated by the degree of its phosphorylation and is otherwise known as a phosphoprotein (Lindwall and Cole 1984) (Alonso et al. 1994). Tau found in the human brain normally contains 2-3 moles of phosphate per 1 mole of tau protein, an amount found to be optimal for tau's association with microtubules and its role in promoting microtubule assembly (Kopke et al. 1993). Almost all tau is soluble in normal brain, whereas in AD brain tau exists in soluble oligomeric and insoluble fibrillized forms (Kopke et al. 1993) (Grundke-Iqbal et al. 1986) (Bancher et al. 1989). Even though the amount of soluble tau is similar in normal and AD brain, the amount of total tau is significantly increased in AD brain almost entirely due to the presence of abnormally hyperphosphorylated tau (Khatoon, Grundke-Iqbal, and Iqbal 1992). Phosphorylation levels of tau increase by 3-4 fold (8 moles of phosphate per mole of tau) when tau becomes hyperphoshorylated (Kopke et al. 1993). Up to 40% of the abnormally hyperphosphorylated tau exists in the cytosol and is not part of PHFs or NFTs (Kopke et al. 1993) (Grundke-Iqbal et al. 1986) (Bancher et al. 1989). Moreover, this abnormally hyperphosphorylated tau is disruptive to microtubules and inhibits their

assembly (Alonso et al. 1994) (B. Li et al. 2007). Phosphorylation-specific tau antibodies, such as AT8 targeting Ser202/Thr205, have been useful in tracking the progression of tau pathology. Most AD human postmortem brain tissue staging is consistent with the Braak staging scheme where NFTs containing hyperphosphorylated tau are found in the transentorhinal region in stages I-II, then in limbic regions such as the hippocampus and stages III-IV and finally in the general neocortex area during stages V-VI. In later stages, other phosphorylation sites emerge (H. Braak and Braak 1991) (Heiko Braak et al. 2006). It is very possible that differences in tau phosphorylation sites could lead to the development of different tau strains differentiating tauopathies but also adding heterogeneity within the same disease.

Here, we have used quantitative super-resolution microscopy in combination with an unsupervised machine learning-based shape classification approach we developed to study the different tau aggregate species present in an engineered cell model expressing tau harboring the FTDP-17 mutation P301L and transduced with exogenous tau fibrils to mimic tau aggregation in disease (QBI-293 Clone 4.1 cells expressing 4R-P301L-GFP tau). Using antibodies that recognize different phosphorylation states of tau and our shape classification method, we further show that different phosphorylation states associate with distinct higher-order tau aggregate species in this engineered cell model.

Results

Iterative Hierarchical Clustering Identifies the Presence of Distinct Tau Aggregate Classes.

To further investigate the types of higher-order tau aggregates present in Clone 4.1 cells, we developed an unsupervised shape classification algorithm based on iterative

hierarchical clustering to classify the large tau aggregates present in SMLM images (*SI Appendix B*, *Materials and Methods* and Fig. B1A–F). We named the algorithm Iterative Hierarchical Clustering c-RSD (constrained relative SD). We first visually separated Clone 4.1 cells into two categories: those showing a low level of tau aggregation containing mainly small tau aggregates and those showing a high level of tau aggregation containing larger tau aggregates. The SMLM images from these two categories were then segmented into individual tau aggregates using density-based spatial clustering of applications with noise (DBSCAN) (Ester et al. 1996) (*SI Appendix B*, *Materials and Methods*). We focused on tau aggregates containing more than 500 localizations. This choice was due to the fact that aggregates with fewer localizations than 500 represented a uniform class of nanoclusters with no particular shape and likely corresponded to tau oligomers (*SI Appendix B*, Fig. B1C) (~2.5% of all segmented objects had >500 localizations in Clone 4.1 cells). DBSCAN segmentation of images from Clone 4.0 cells gave rise to very few segmented objects containing >500 localizations (~0.12% of all segmented objects had >500 localizations in Clone 4.0 cells), further confirming that these objects correspond to tau aggregates not present in cells lacking tau aggregation. The tau aggregates coming from cells with low and high tau aggregation levels were combined into a single list and further classified with Iterative Hierarchical Clustering c-RSD. The number of localizations per tau aggregate, tau aggregate area, length, and width were used as classification parameters. We imposed a threshold for the coefficient of variation for each parameter and grouped the tau aggregates together into individual classes as long as the coefficient of variation in the parameters did not exceed the imposed threshold (i.e., the tau aggregates within each class were "self-similar" within the imposed threshold) (*SI Appendix B*, *Materials and Methods*).

Smaller variation thresholds result in a larger number of identified classes from the classification scheme. We selected the threshold such that the classification was more sensitive to aggregate length and width (i.e., aggregate shape) than the number of localizations and area.

Table S.3.1 contains the number of tau aggregates that were segmented before classification and the resulting number of classes after classification. The classes were represented in the form of a dendrogram tree (*SI Appendix B*, Fig. B1D). The initial classification tended to overestimate the number of classes and tau aggregates that were visually self-similar were classified as distinct classes. Thus, we further narrowed them down by combining classes that were close in the dendrogram tree and visually looked similar to each other (*SI Appendix B*, Table S.3.1 and Fig. B1 D–F). This classification generated 22 classes containing tau aggregates coming from cells with both low and high levels of tau aggregation. These classes contained tau aggregates ranging in area by three orders of magnitudes (from 0.025 μm^2 for the smallest classes to 30 μm^2 for the largest ones). The presence of as many as 22 classes of tau aggregates suggests that the tau aggregates found in Clone 4.1 cells are highly diverse in terms of their size and shape.

We plotted the results in the form of an ellipse graph in which each ellipse corresponds to a specific tau aggregate class (Fig. 3.1 A–J). The size of the ellipse corresponds to the percentage of total tau aggregates from cells with low or high levels of tau aggregation in that particular class (*SI Appendix B*, Table S.3.2), whereas the shape of the ellipse represents the shape of the aggregates in that particular class (i.e., more elongated ellipses correspond to elongated aggregates with high aspect ratio). Visual inspection of

aggregates within specific classes revealed linear tau fibrils (e.g., class 6, Fig. 3.1D), branched tau fibrils (e.g., classes 9 and 10, Fig. 3.1E), NFT pretangle-like structures (e.g., classes 12 and 15, Fig. 3.1I) as well as large agglomerate structures resembling NFTs (e.g., classes 21 and 22, Fig. 3.1J). These different classes may represent different stages of tau aggregation or different aggregation pathways. There was a large overlap in terms of the tau aggregate classes found in cells with low and high levels of tau aggregation. Linear and branched tau fibrils constituted the majority of tau aggregate classes in both cases. However, there were also some unique classes that were only present in cells with high levels of tau aggregation (Fig. 3.1 H and J and *SI Appendix B*, Table S.3.2). In particular, classes having large areas and a large number of localizations that resembled NFT-like structures (e.g., classes 21 and 22) were only found in cells with high levels of tau aggregation, whereas small tau fibrils (e.g., class 6) were more representative of cells with low levels of tau aggregation.
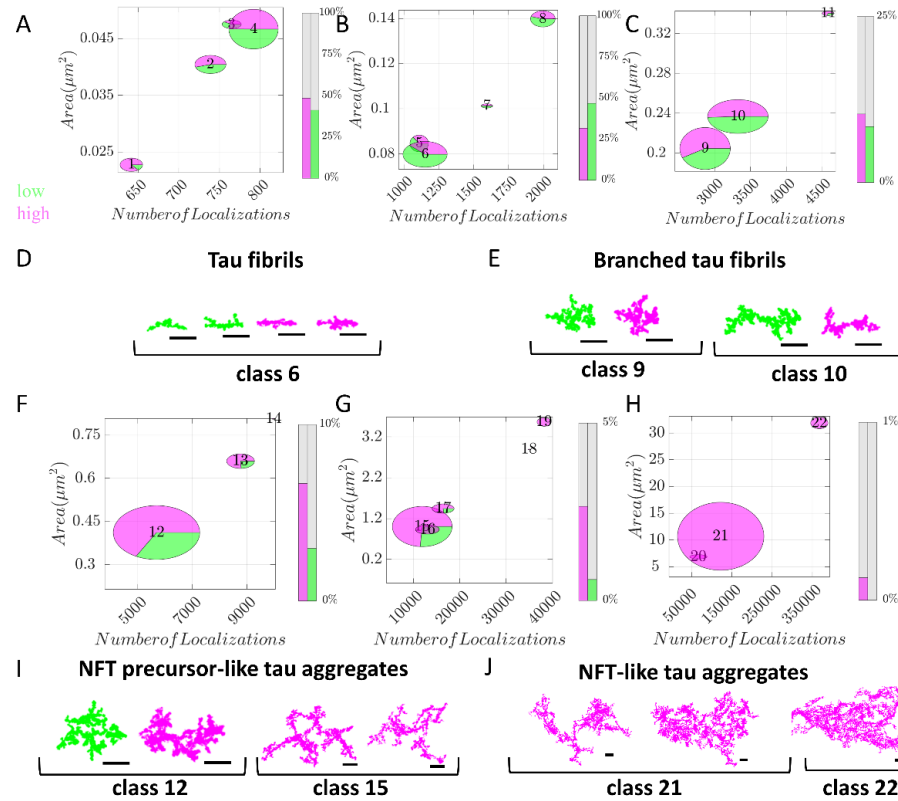
Figure 3.1: Shape classification reveals distinct classes of tau aggregates in Clone 4.1 cells. A–C and F–H. Ellipse plots showing the different tau classes found in Clone 4.1 cells maintained in Dox and expressing 4R-P301L-GFP tau. They are showing either low (green) or high (magenta) levels of tau aggregation. Each ellipse represents a separate class. The plot axes represent the number of localizations per tau aggregate and area of tau aggregates in square micrometer. Each ellipse is placed on the plot to represent the average number of localizations and area of the tau aggregates within that class. The size of the ellipses is scaled within each plot to represent the proportion of tau aggregates contained in that particular class, but the size is not comparable between the different plots. Green represents the proportion of tau aggregates from low tau aggregation cells, whereas magenta represents the proportion of tau aggregates from high tau aggregation cells. The bar charts next to the ellipse plots represent the percentage of tau aggregates from each category (low in green and high in

42

magenta) found in classes in the specified number of localizations and area range. Ellipses represent average numbers, not extreme outliers. D, E, I, and J. Representative super-resolution images of tau aggregates from some of the most prominent classes in each plot. Shapes from cells showing low levels of tau aggregation are colored green, whereas those from cells showing high levels of tau aggregation cells are colored magenta. (Scale bars: 500 nm.)

Phosphorylation of Specific Tau Residues Is Associated with Different Types of Higher-Order Tau Aggregates.

Iterative Hierarchical Clustering c-RSD revealed the presence of a diverse range of tau aggregates (Fig. 3.1 A–J). However, the nature of tau present within these aggregates is unclear. In order to investigate the phosphorylation state of tau within these aggregate species, we performed two-color SMLM using two commonly used phospho-tau antibodies, Thr231 and AT8, which are known to have high labeling specificity (D. Li and Cho 2020). Thr231 targets tau that is phosphorylated at the 231st threonine, which is considered to be an early marker of tau aggregation. AT8 targets tau that is phosphorylated at the serine residue at position 202 and threonine at position 205 (Ser202/Thr205), which is considered to be a late marker of tau aggregation. Staining with both antibodies gave rise to a low, nonspecific, fluorescent signal in Clone 4.0 cells compared to Clone 4.1 cells (*SI Appendix B*, Fig. B2 A and B), indicating that tau present in Clone 4.0 cell line is not hyper-phosphorylated at any of the targeted residues (Matsuo et al. 1994). This result is in line with the expectation that hyper-phosphorylation of these residues is a marker of pathological tau aggregation and further supports that Clone 4.1 cells exhibit common markers of tau pathology found in disease. Single-color (Fig. 3.2 A and B and additional representative images in *SI Appendix B*, Fig. B3 A and B) and

two-color (*SI Appendix B*, Fig. B3 C and D) SMLM images of Clone 4.1 cells with either the Thr231 or the AT8 antibodies revealed that both antibodies bind to a wide range of tau aggregates having diverse shapes and sizes. Only ~12 ± 10% (~20% corrected) of GFP tau found within Clone 4.1 cells colocalized with either Thr231 or AT8 (Fig. 3.2C), suggesting that aggregation in this cell model can potentially proceed in the absence of hyperphosphorylation of these particular tau epitopes. The number of localizations per tau aggregate detected by the two antibodies was similar, suggesting that there is overlap in the tau aggregates that these antibodies target (*SI Appendix B*, Fig. B3E).
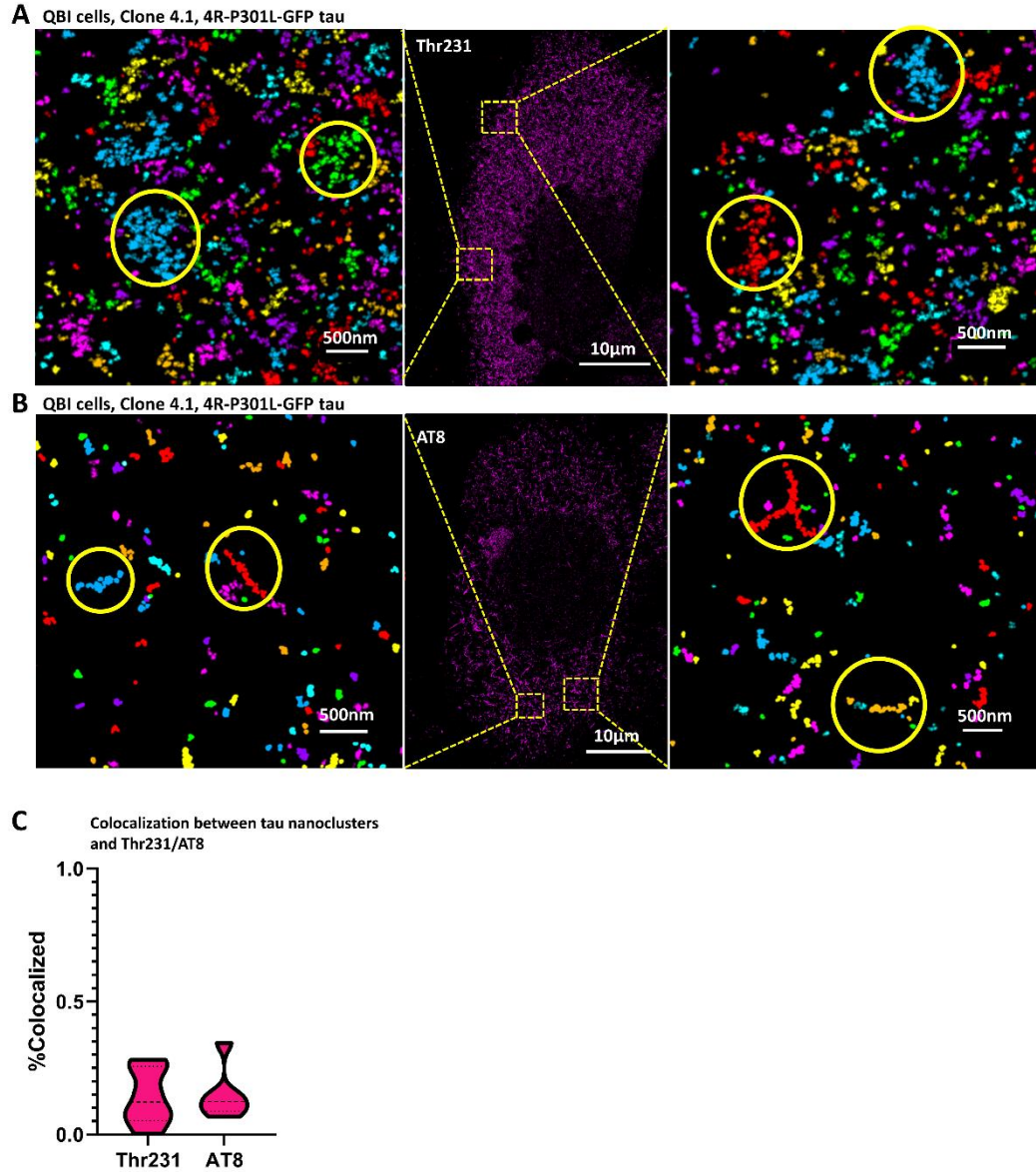
Figure 3.2: Branched tau fibrils and long tau fibrils are the predominant tau structures recognized by Thr231 and AT8 antibodies, respectively. A. Super-resolution image of tau labeled with the Thr231 antibody in Clone 4.1 cells maintained in Dox and expressing 4R-P301L-GFP tau. Zoomed-in regions after Voronoi segmentation are shown. Segmented images are pseudo color coded with different colors corresponding to different segmented objects. Yellow circles highlight branched tau fibril-like structures. B. Super-resolution image of tau

labeled with AT8 antibody in QBI cells, Clone 4.1, expressing 4R‑P301L‑GFP tau. Zoomed in regions after Voronoi segmentation are shown. Segmented images are pseudo color coded with different colors corresponding to different segmented objects. Yellow circles highlight long tau fibril-like structures. C. Violin plots showing the percentage of tau nanoclusters colocalized with Thr231, and AT8 antibodies in Clone 4.1 cells maintained in Dox and expressing 4R‑P301L‑GFP tau (pink). (Thr231 in Clone 4.1: n = 6 cells, n = 2 experiments; and AT8 in Clone 4.1: n = 6 cells, n = 3 experiments)

To further investigate whether different tau aggregates have differential phosphorylation states, we classified tau aggregates from Clone 4.1 cells stained with either the GFP nanobody or the Thr231 or AT8 antibody using Iterative Hierarchical Clustering c-RSD. We obtained 23 classes, very similar to the number of classes obtained from classifying the GFP nanobody-labeled aggregates in cells having low or high levels of tau aggregation (*SI Appendix B*, Table S.3.2). As expected, there was large overlap in the tau aggregate classes stained with the Thr231, AT8, and GFP nanobody (Fig. 3.3 A–J). However, tau aggregates from cells stained with Thr231, which is an earlier tau aggregation marker, were over-represented by approximately twofold in class 3, corresponding to small, branched tau fibrils (Fig. 3.3E and *SI Appendix B*, Table S.3.3) compared to AT8 or the GFP nanobody. It is therefore possible that phosphorylation at this residue is a characteristic of small, branched tau fibrils. Similarly, AT8-labeled tau aggregates were over-represented by approximately two- to fourfold in classes 4 and 5, corresponding to long linear fibrillary structures, suggesting that phosphorylation at Ser202/Thr205 may be a prominent feature of this class of tau aggregates (Fig. 3.3D and *SI Appendix B*, Table S.3.3). Furthermore, there were unique classes resembling NFT pretangle-like and NFT-like structures, which were only present in cells stained with the late tau aggregation

marker AT8 but not the early tau aggregation marker Thr231 (Fig. 3.3 F–J and *SI Appendix B*, Table S.3.3). It is possible that the phosphorylated Thr231 epitope is not accessible to the antibody within these large aggregates. However, it is also possible that not all tau aggregates acquire this phosphorylation mark.
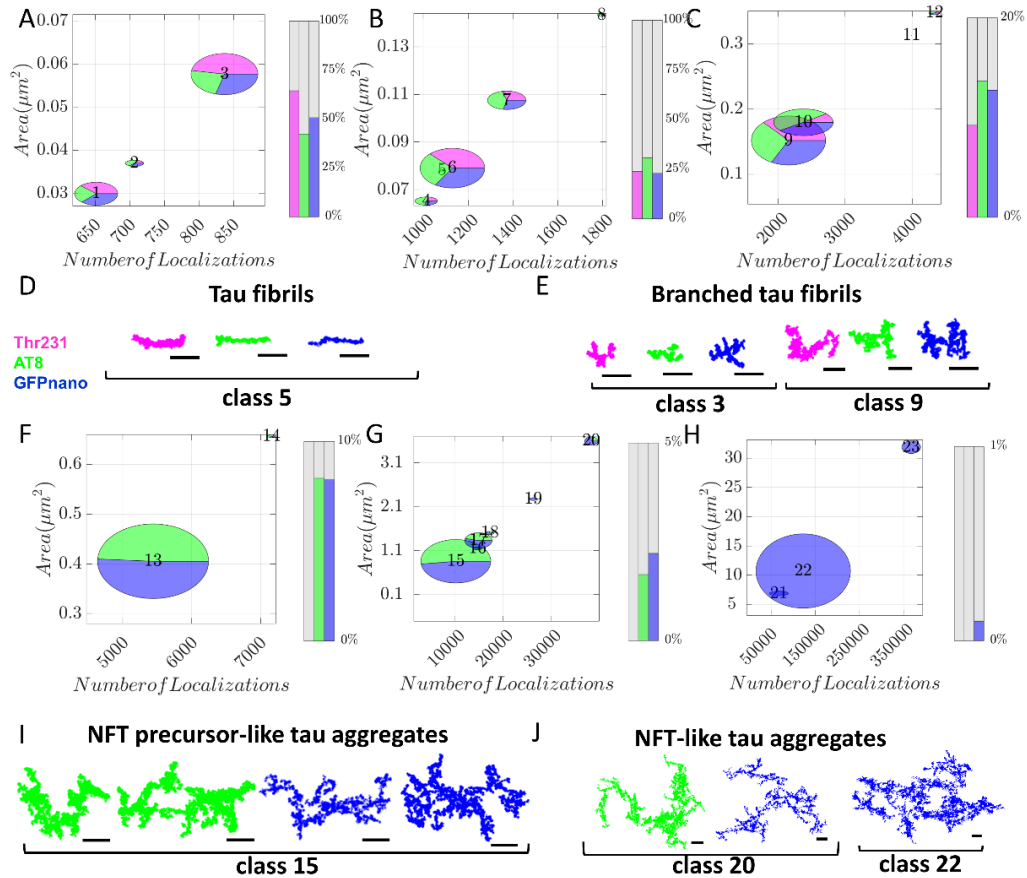
Figure 3.3: Shape classification differentiates higher-order aggregates based on phosphorylation status. A–C and F–H. Ellipse plots showing the different tau classes found in Thr231- (magenta), AT8- (green), or GFP nanobody- (blue) labeled Clone 4.1 cells maintained in Dox and expressing 4R-P301L-GFP tau. Ellipse representation is the same as in Fig. 3.1. D, E, I, and J. Representative super-resolution images of tau aggregates from some of the

47

most prominent classes in each plot. Shapes from Thr231-stained cells are colored magenta, those from AT8-stained cells are colored green, and those from the GFP nanobody staining are colored blue. N/A indicates not available. (Scale bars: 500 nm.)

Discussion

In this work, we showed that oligomers in cells that represent a nonaggregated state of tau are not hyperphosphorylated at residues Thr231 and Ser202 and Thr205, but oligomers in cells that represent an aggregated state of tau contain these phosphorylation markers, suggesting that physiological oligomers are distinct from pathological oligomers. Hyperphosphorylation of tau has been considered a prerequisite for tau aggregation since the negative charge of phosphor residues neutralizes the positively charged microtubule-binding region of tau, leading to tau's dissociation from the microtubules and eventual aggregation (Maeda et al. 2007). However, tau oligomerization can occur without hyperphosphorylation or the addition of inducers, suggesting that hyperphosphorylation of tau *in vivo* could be important for dissociation from microtubules but may not be necessary for the aggregation step (Hill et al. 2019). Additionally, biochemical studies have shown that tau oligomers are most likely hetero-oligomers of nonhyperphosphorylated and hyperphosphorylated tau (Kopke et al. 1993). Hence, it is possible that tau aggregation can start on the microtubule before tau dissociation due to hyperphosphorylation. In the future, it would be interesting to study the kinetics of pathological tau aggregation over time to directly test this model.

Phosphorylation at Thr231 is an early aggregation event which diminishes the ability of tau to bind to microtubules and is often used as a marker for postmortem diagnosis of most tauopathies (Cho and Johnson 2003). Phosphorylation at Ser202 and Thr205 is a

marker of late-stage aggregation and is also used for postmortem diagnosis of tauopathies (Kimura et al. 2018). Here, we show that phosphor-tau antibodies that recognize these different phosphorylation sites label a subset of tau aggregates, suggesting that tau aggregation can proceed in the absence of phosphorylation at these residues. Furthermore, using Iterative Hierarchical Clustering c-RSD, we classified the tau aggregates containing these specific phosphorylation marks. The resulting classification identified a variety of distinct classes of tau aggregates that could be grouped into four general categories: tau fibrils, branched tau fibrils, NFT pretangle-like tau aggregates, and NFT-like tau aggregates. There was an overlap in the classes stained by the nanobody/antibodies, but there were also classes that were more prominently recognized by either the Thr231 or the AT8 antibodies. These results suggest that phosphorylation at certain residues may be a characteristic of distinct types of tau aggregates.

In recent years, the idea of tau strains with distinct structural conformations has become prevalent (Kimura et al. 2018) (Prusiner 1984). In particular, it has been found that different tauopathies are associated with disease-specific tau protofilaments (Fitzpatrick et al. 2017) (Sanders et al. 2014) (Falcon et al. 2018) (Falcon et al. 2019) (W. Zhang et al. 2019b). Recent cryo-EM work in combination with mass spectrometry–based proteomics revealed that posttranslational modifications (PTMs) of tau such as ubiquitination can mediate interprotofilament interfaces (Arakhamia et al. 2020). Based on these results, a structure-based model has been proposed in which cross-talk between tau PTMs influences tau filament structure, leading to diversity of tauopathy-specific tau strains (Arakhamia et al. 2020).

It is possible that some of the different classes of tau aggregates we detected in our FTDP-17 model are propagated by the different tau strains and that differences in tau filament structure identified in cryo-EM lead to different higher-order tau aggregate classes identified in super-resolution microscopy, an idea reinforced by the finding that the phosphorylation state of tau is distinct in certain tau aggregate classes. It would be interesting in the future to determine whether different *MAPT* mutations and different tau PTMs associated with tauopathies, including acetylation, phosphorylation, and ubiquitination (Alquezar, Arya, and Kao 2021), lead to different tau aggregates. A combination of super-resolution microscopy and cryo-EM can in the future reveal differences in tau filament structure of different classes of higher-order tau aggregates.

Here, using super-resolution microscopy and a shape classification method, we showed that tau aggregate species could have distinct phosphorylation marker profiles which could lead to the formation of distinct tau strains. Our custom algorithm, Iterative Hierarchical Clustering c-RSD, will be a useful tool for differentiating between tau aggregates associated with different tau strains in the future and could facilitate the study and identification of tau strains *in vitro* and *in vivo*.

Materials and Methods

A detailed description of the methods can be found in *SI Appendix B*.

CHAPTER 4. DISTINCT TAU AGGREGATE SPECIES BECOME DEGRADED BY THE UBIQUITIN-PROTEASOME SYSTEM AND AUTOPHAGY

Introduction

Tauopathies are characterized by the abnormal accumulation of tau aggregates, which are not properly degraded by the cell's main degradation pathways of autophagy and the ubiquitin-proteasome system (UPS). More specifically, UPS involves degradation by the 20S proteasome, which is the proteolytic core of the 26S holoenzyme (Bochtler et al. 1999). Intrinsically disordered proteins (IDPs) such as soluble tau can also be degraded just by the 20S proteasome without the need of the 19S regulatory subunit (David et al. 2002). Phosphorylation and aggregation of tau can inhibit its degradation by the 20S subunit (Poppek et al. 2006). Hyperphosphorylated, insoluble tau aggregates are traditionally thought to be degraded by autophagy instead (Cheng et al. 2018). Yet, the presence of accumulated lysosomes, autolysosomes, autophagosomes as well as defective lysosomal membranes in the brains of AD, CBD and PSP patients indicates defective autophagic activity (Nixon et al. 2005) (Nixon 2013) (Piras et al. 2016). In fact, excess of tau aggregates is indeed thought to have a negative impact on UPS and/or autophagy, inhibiting these pathways inside neurons. Along similar lines, pharmacological inhibition of these pathways can result in the accumulation of tau aggregates (J. L. Guo et al. 2016). Previously, using super-resolution microscopy and machine learning based shape classification (see Chapter 3), we showed that tau aggregates form a morphologically diverse class consisting of tau oligomers, linear fibrils, branched fibrils, NFT Precursor-like and NFT-like species. However, the physical nature of the tau aggregates which can be cleared by UPS or autophagy pathways as well as the physical nature of tau aggregates that accumulate as a result of dysfunctional clearance

mechanisms has not been elucidated. Understanding the nature of such aggregate species could have important therapeutic implications.

Here, using super-resolution imaging and computational analysis, we have now extended our previous work in the aggregated tau cell line, QBI-293 Clone 4.1 cells expressing 4R-P301L-GFP tau to determine i) the timing of tau aggregate clearance upon removal of soluble tau, and ii) the morphological characteristics of tau aggregate species degraded by autophagy and/or UPS.

Results

Tau protein and tau aggregate density gradually decrease following the removal of soluble tau

To examine the process of tau aggregate degradation, we performed single molecule localization microscopy (SMLM) in an engineered cell model of tau aggregation consisting of an inducible QBI-293 cell line stably expressing GFP-tagged tau harboring a FTDP-17 mutation (P301L) under the control of doxycycline (Dox) (QBI-293 Clone 4.1 cells expressing 4R-P301L-GFP tau). Removal of Dox from the culture media ceases expression of the soluble tau construct. Previous work (J. L. Guo et al. 2016) showed that removal of dox led to a decrease in the tau aggregate amount by using Western Blot analysis of the Triton-insoluble fraction. The decrease in tau aggregates was not a result of dilution due to cell division as whole coverslip quantification of Triton-insoluble aggregates in cells plated at 5 days off dox and analyzed at 7 and 10 days off dox without any further passaging showed a similar decrease in total tau aggregate intensity (J. L. Guo et al. 2016). To get a deeper insight into the physical nature of tau aggregates cleared upon dox removal in this cell model, we used SMLM imaging of cells fixed at several time

points after dox removal. The SMLM results recapitulated the previous findings demonstrating a decrease in tau aggregates over time (Fig. 4.1A, *SI Appendix C*, Fig. C1A-G). A quantitative analysis of the localizations corresponding to tau proteins in our images revealed a gradual decrease in tau protein density upon Dox removal compared to the +dox control, where cells are kept in media containing Dox (Fig. 4.1B). More specifically, the most significant decrease in tau protein density starts on day 3 off dox (median: 0.0002361) compared to the +dox control (median: 0.0007115) (a 3-fold decrease) and the next major drop is on day 10 off dox (0.00004606) (a 15-fold decrease) (Fig. 4.1B, C). These results are consistent with tau aggregate degradation shown in previous studies (J. L. Guo et al. 2016) and inconsistent with cell division mediated aggregate dilution, where a gradual 2-fold decrease is expected per day as cells divide.
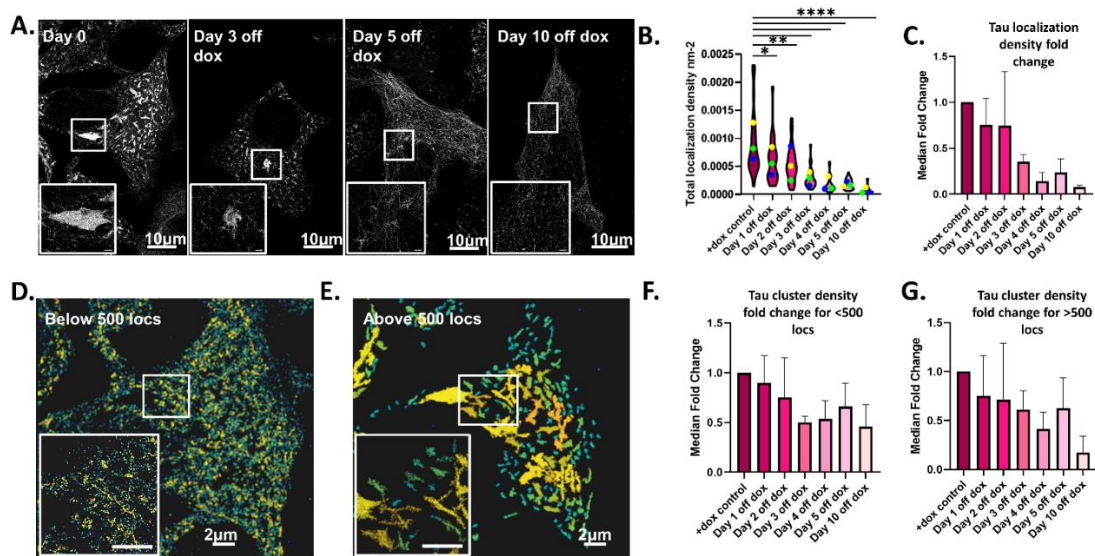
Figure 4.1: Tau aggregate density decreases in the absence of soluble tau. A. SMLM images of tau in the FTDP-17 cell model, where doxycycline (dox), which controls the expression of the soluble tau construct has been removed from the media for several days. Scale bar in inset is 1μm. B, C. Plots of the total localization density (proportional to tau protein density) (B) and median fold

change in the localization density (C) of tau proteins in cells exhibiting tau aggregation under +dox and various days following dox removal. Plots represent three biological replicates (different colored means in B). Fold change is calculated with respect to +dox. D. Segmented images of tau clusters with less than 500 localizations (locs). E. Segmented images of tau clusters with more than 500 localizations (locs). Different clusters are pseudocolored. Scale bar for insets is 2 µm. F. Median fold change plots of the number of clusters with less than 500 localizations normalized to the cell area in cells exhibiting tau aggregation either with +dox or day 1, 2, 3, 4, 5 or 10 after dox removal. Fold change is calculated with respect to +dox. G. Plots of the number of clusters with more than 500 localizations normalized to the cell area in cells exhibiting tau aggregation either on day 0 or day 1, 2, 3, 4, 5 or 10 after dox removal. Error bars indicate standard deviation (SD). +dox control: n= 29 cells, n= 3 experiments, Day 1 off dox: n= 27 cells, n= 3 experiments, Day 2 off dox: n= 30 cells, n= 3 experiments, Day 3 off dox: n= 27 cells, n= 3 experiments, Day 4 off dox: n= 29 cells, n= 3 experiments, Day 5 off dox: n= 27 cells, n= 3 experiments, Day 10 off dox: n= 28 cells, n= 3 experiments, * P<0.05, ** P<0.001, ****P < 0.0001.

Visual inspection of images showed that large tau aggregates resembling NFTs seem smaller in size and their presence becomes less frequent in images from later days off dox (*SI Appendix C*, Fig. C1A-G). As we previously showed (see Chapter 2), tau aggregates in Clone 4.1 cells are mainly cytosolic and only a small percentage of small, oligomeric tau is microtubule-associated. Interestingly, a pattern resembling microtubule-associated tau similar to Clone 4.0 cells (non-aggregated cell model) re-appears on day 5 off dox in some cells and persists at later time points (Fig. 4.1A). On day 10 off dox, almost all tau is microtubule-associated and large tau aggregate structures are rarely observed. These results are also inconsistent with cell division mediated dilution, in which we would expect to have similar aggregates over time but with reduced numbers per cell area.

To get better insight into the clearance dynamics of the small tau aggregates compared to large tau aggregate species, we used the Voronoi tessellation approach to cluster and segment individual tau aggregates (Fig. 4.1D, E). We then divided the segmented tau aggregates into two categories, aggregates with less than 500 localizations, which we previously showed mainly correspond to tau oligomers/small fibrils and those containing more than 500 localizations, which mainly correspond to insoluble tau aggregates including large linear and branched fibrils and NFTs. We determined the number of tau aggregates belonging to each category and normalized this number with cell area to calculate how tau oligomer and insoluble aggregate density changes over time upon Dox removal. Interestingly, the density of tau aggregates with less than 500 localizations (likely corresponding to tau oligomers) is relatively consistent from +dox to day 1 and 2 off dox, drops at day 3 off dox and maintains similar levels until day 10 off dox (Fig. 4.1F). The density of large and insoluble tau aggregates containing more than 500 localizations also drops on day 3 off dox but continues to decrease over time with the next major drop happening at 10 days off dox (Fig. 4.1G). These results suggest that small tau aggregates (oligomers, small fibrils) are degraded first while the larger tau aggregates take longer time to clear and continue to be degraded until later days off dox. Alternative interpretation of these results could be that large aggregates become split up into smaller units (oligomers, small fibrils) at later time points and these smaller aggregates are then cleared. Breaking apart of the larger aggregates into smaller oligomers (<500 localizations) would lead to an increase in this small aggregate density and the simultaneous clearance of these small aggregates would then balance out the increase potentially resulting in constant levels of small aggregates present throughout the later days of dox removal.

Pre-NFTs and NFTs are more efficiently cleared upon Dox removal compared to linear fibrils.

Next, we aimed to examine more closely which tau aggregate species become degraded during the dox removal process. In particular, we focused on large tau aggregates containing more than 500 localizations. We manually classified data from the +dox control, day 1 off dox and day 2 off dox into 4 categories: linear fibrils, branched fibrils, NFT Precursors, and NFTs. We then used this manual classification to train and test a machine learning model for predicting different classes of tau aggregates under different conditions (see more below).

Prior to the prediction of different tau classes using machine learning, we first performed a simpler principal component analysis (PCA) on the tau aggregates from +dox, day 1, 2, 3, 4, 5 and 10 off dox to look for similarities as well as differences between these conditions. Principal component analysis (PCA) is a technique that uses a linear combination of the original variables to create new, uncorrelated, variables (called latent variables). This data transformation reduces the number of variables while preserving as much of the information as possible. In this particular example, the original data consists of a series of spatial shape descriptors that describe the tau aggregates, including geometric (e.g., area, number of localizations, etc.), boundary (e.g., elasticity, bending energy, etc.), image-related (e.g., texture, grayscale intensity, etc.), fractal (e.g., Minkowski dimension, Haussdorff area, etc.), skeleton (e.g. cloud width, mean length, etc.), and moments (e.g. inertia, dispersion, etc.) descriptors. Data from the +dox control, day 1 and day 2 off dox completely overlapped in the PCA space indicating that there are many similarities in the characteristics (shape, size) of tau aggregates present in these groups, which is consistent with our observation that substantial degradation does not

start until day 3 off dox (Fig. 4.1B, *SI Appendix C*, Fig. C2A). We further compared the PCA plots of the manually classified subsets of linear fibrils (*SI Appendix C*, Fig. C2B), branched fibrils (*SI Appendix C*, Fig. C2C), NFT Precursors (*SI Appendix C*, Fig. C2D), and NFTs (*SI Appendix C*, Fig. C2E). While these different classes were separated in the PCA space as expected (*SI Appendix C*, Fig. C2F), each individual class showed a high degree of overlap when comparing the +dox control, day 1 and day 2 off dox, suggesting that these classes have similar characteristics in +dox, 1 and 2 days off dox conditions. Since the data between these three experiments were so similar, we represented them as one color in the PCA plot along with data from day 3, 4, 5 and 10 off dox represented as different colors (Fig. 4.2A, B, *SI Appendix C,* Fig. C3). We noticed that the data points belonging to day 4, 5 and 10 off dox showed a shift towards the upper left quadrant of the PCA space compared to +dox, 1 and 2 days off dox (Fig. 4.2A, B). When we compared the data from later days off dox (4, 5 and 10 days) to the manually classified classes of linear/branched fibrils and NFT Precursors/NFTs, we saw that the observed shift corresponded to a shift towards linear/branched fibrils and away from NFT Precursors/NFTs (Fig. 4.2C, D). These results suggest that NFT Precursor and NFT aggregates have been either already degraded or broken down at these later time points, whereas the linear/branched fibrils are still remaining.
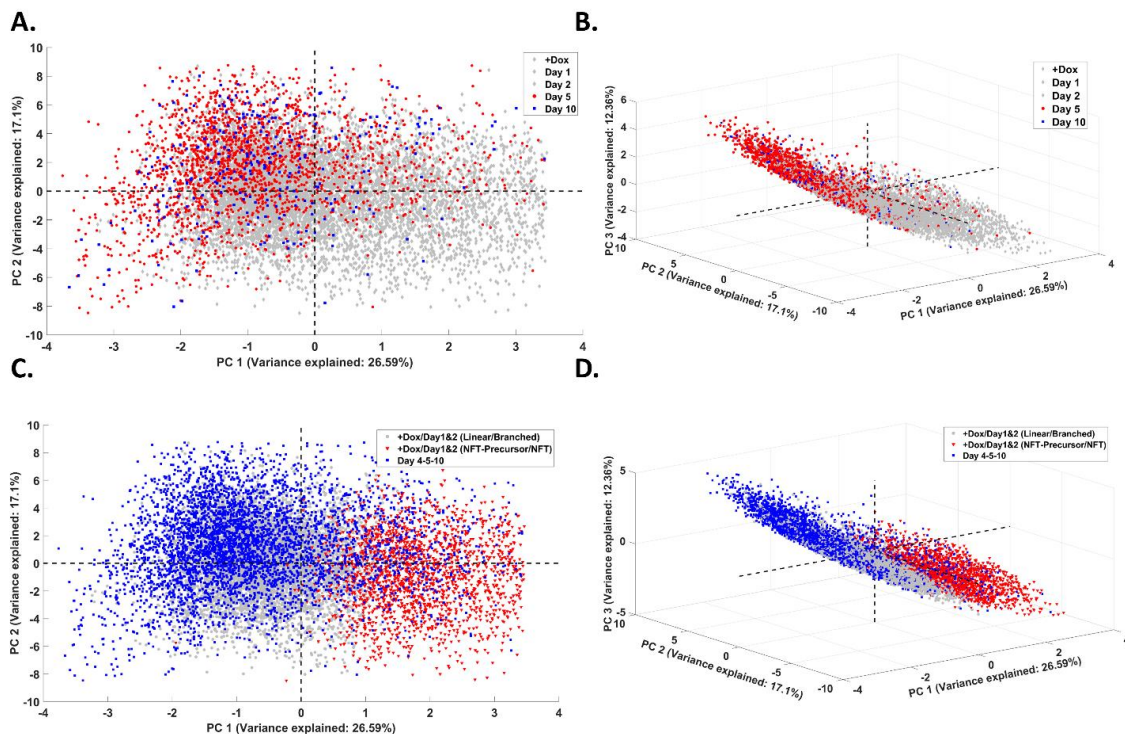
Figure 4.2: PCA reveals differences in tau aggregate structures from different days off dox. A, B. 2-D and 3-D PCA plot of tau aggregates from cells from +dox control (grey), Day 1 (grey), Day 2 (grey), Day 5 (red) and Day 10 off dox (blue). C, D. 2-D and 3-D PCA plots of tau aggregates from cells of Day 4, 5 and 10 off dox (blue) superimposed with tau aggregates from +dox, Day 1 and Day 2 that are either linear or branched fibrils (grey) or NFT and NFT Precursor structures (red).

To further support these results, we used the machine learning approach to classify tau aggregates into distinct aggregate classes. We first trained the model on a subset of the manually classified tau aggregates and then used the model to predict the remaining subset of manually classified tau aggregates that were not used for the training. To determine the robustness of the model in classifying tau aggregates, we generated a confusion matrix to compare the classified classes to the true classes (determined from the manual classification) (Fig. 4.3A). The probability that a prediction would match the true class was high for all types of classes, giving high confidence that the classification

can robustly distinguish different classes of tau aggregates. We then used the machine learning to predict tau classes present in the entire dataset from +dox control and Days 1-10 off dox conditions and plotted the percentage of aggregates belonging to each class on different days. Interestingly, the proportion of linear fibrils increased starting at around 4 days off dox while the proportion of NFT Precursors and NFTs decreased (Fig. 4.3B). The proportion of branched fibrils stayed steady (Fig. 4.3B). These results suggest that NFT precursors and NFTs are more efficiently cleared or broken apart while fibrils, particularly linear fibrils are more resistant to degradation and are less efficiently cleared over time.
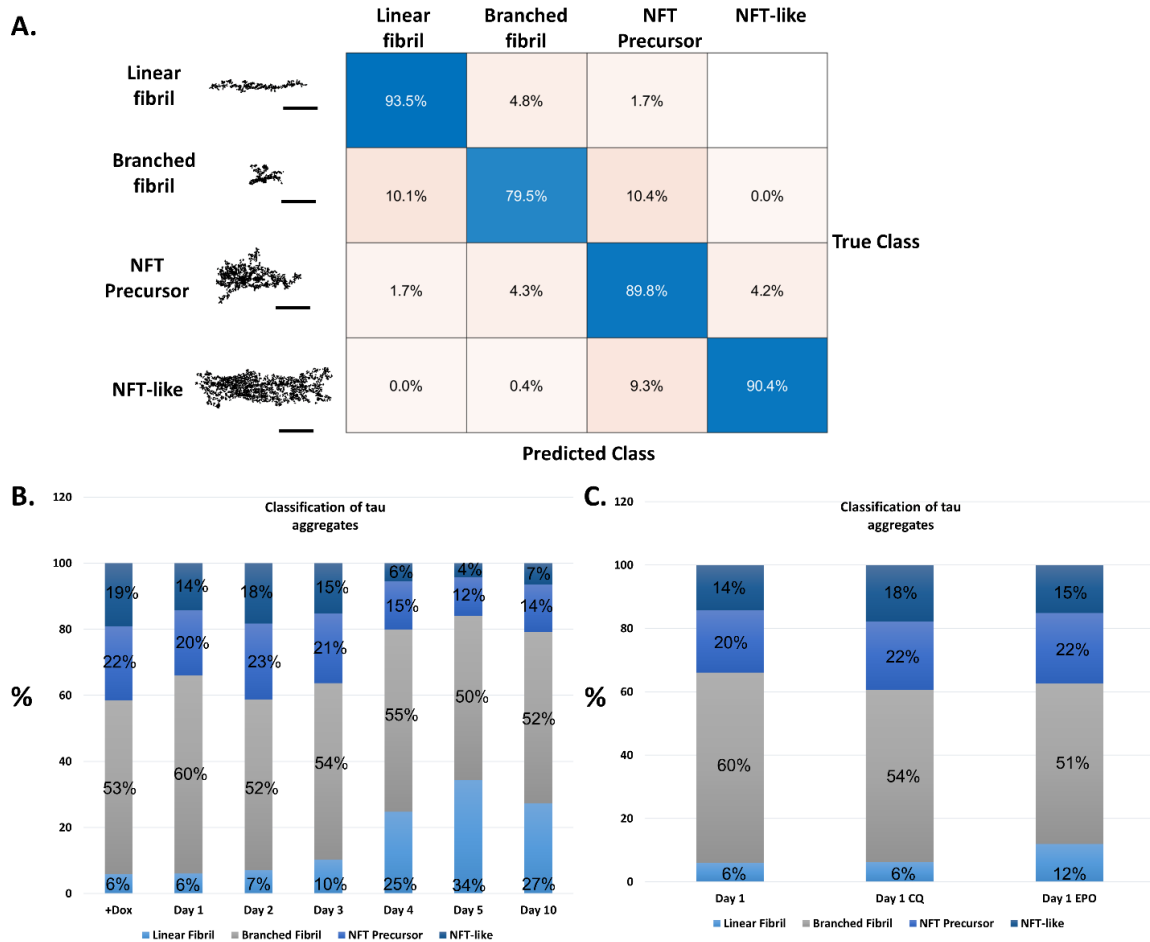
Figure 4.3: Linear fibrils persist longer than other tau aggregates following dox removal. A. Confusion matrix showing the confidence of the class predictions in % accompanied by representative STORM images of each class. B. Stacked bar plots showing the percentage of tau aggregate structures that belong to each of the four classes in cells from +dox control, Day 1, 2, 3, 4, ,5 and 10 off dox. C. Stacked bar plots showing the percentage of tau aggregate structures that belong to each of the four classes in cells from Day 1 off dox, Day 1 off dox and CQ and Day 1 off dox and epo.

Autophagy and UPS clear distinct classes of tau aggregates

To determine which degradation pathways are responsible for clearance of tau aggregates following the removal of soluble tau from Clone 4.1 cells, we employed inhibitors of the autophagy and UPS pathways. More specifically, we used chloroquine diphosphate (CQ), a widely used autophagy inhibitor, which inhibits the fusion of autophagosomes with lysosomes by lowering the lysosomal pH (Mauthe et al. 2018). We either added 30 μM CQ simultaneously while removing Dox and treated for 1 day (day 1 off dox and CQ). In a second set of experiments, we added 30 μM CQ after cells had been without dox for 1 day and treated for 1 day (day 2 off dox and CQ) (Fig. 4.4A). To ensure that the treatments indeed inhibited autophagy, we performed a Western blot in cell lysates from Clone 4.1 cells. There was a decrease in autophagy flux indicated by the presence of both LC3-I and LC3-II in lysate from cells treated with CQ for 1 day together with dox removal (day 1 off dox and CQ) compared to cells from +dox or day 1 off dox control without CQ treatment (*SI Appendix C*, Fig. C4A). Similar results were obtained for day 2 off dox and CQ compared to +dox or day 2 off dox control without CQ treatment (*SI Appendix C*, Fig. C4B). Additionally, we transfected Clone 4.0 cells with a plasmid containing LC3, an autophagosomes marker, fused to mRFP and eGFP. When autophagosomes fuse with lysosomes to initiate autophagy, lysosomal acidification quenches eGFP but not mRFP. Therefore, eGFP fluorescence reports autophagosomes before fusion whereas mRFP fluorescence reports both autophagosomes and autolysosomes (Mohan et al. 2019). We compared cells in the following conditions: day 2 off dox and day 2 off dox and 30 μM CQ. On day 2 off dox, there were more autolysosomes present than autophagosomes as is expected when autophagy is active (*SI Appendix C*, Fig. C4C). On day 2 off dox and 30

µM CQ, there were much fewer autolysosomes present consistent with autophagy inhibition (*SI Appendix C,* Fig. C4D).
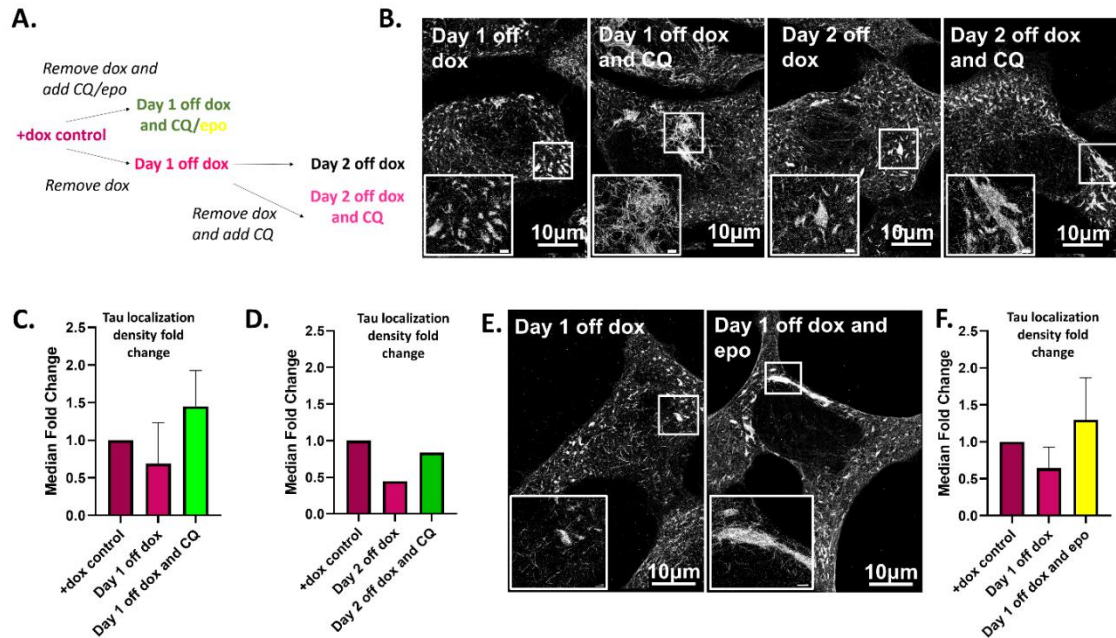
Figure 4.4: Autophagy and UPS inhibition lead to tau aggregate accumulation. A. Schematic of CQ and epo treatments. B. SMLM images of tau in the FTDP-17 cell model, where dox has been removed for one or two days and 30uM of autophagy inhibitor, chloroquine diphosphate (CQ) has been added either on day 1 off dox or day 2 off dox. Scale bar in inset is 1µm. C and D. Plots of the median fold change in tau protein density in cells exhibiting tau aggregation following removal of dox for one or two days and/or treatment with autophagy inhibitor, CQ on day 1 or day 2 off dox. C: +dox control: n= 18 cells, n= 2 experiments, Day 1 off dox: n= 14 cells, n= 2 experiments, Day 1 off dox and CQ: n= 17 cells, n=2 experiments. D: + dox control: n= 10 cells, Day 2 off dox: n= 10 cells, Day 2 off dox and CQ: n= 7 cells. E. SMLM images of tau in the FTDP-17 cell model, where dox has been removed for one day and/or 20nM of proteasome inhibitor, epoxomicin (epo) has been added on day 1 off dox for 6hr and replaced with off dox cell media. Scale bar in inset is 1µm. F. Plots of the median fold change in tau protein density in cells exhibiting tau aggregation following removal of dox for one day and/or treatment with epo on day 1 off dox. +dox control: n= 13 cells,

n= 2 experiments, Day 1 off dox: n= 13 cells, n= 2 experiments, Day 1 off dox and epo: n= 15 cells, n= 2 experiments. Error bars indicate standard deviation (SD).

Addition of CQ led to further accumulation of tau protein in both treatments (Fig. 4.4B). In the case of day 1 off dox quantitative analysis of the tau localization density in each condition revealed that CQ treatment led to a 1.5-fold increase in tau protein density compared to the +dox control and almost a 2-fold increase compared to tau aggregates from day 1 off dox without CQ treatment (Fig. 4.4C). These results suggest that there is a basal level of tau degradation in these cells even prior to turning dox off, which, when inhibited leads to further accumulation of tau. Day 2 off dox with CQ treatment also led to an accumulation of tau protein compared to day 2 off dox without treatment, but not compared to +dox, which could mean that there are other compensatory degradation mechanisms like UPS that are active at this later point or that some degradation has already happened between +dox and day 1 off dox prior to CQ treatment (Fig. 4.4D). It should be noted that these latter results are preliminary and further biological replicates are needed for confirming these conclusions.

To test the involvement of UPS pathway, we employed a commonly used proteasome inhibitor called epoxomycin (epo), which modifies catalytic subunits of the 20S proteasome resulting in its inhibition (Meng et al. 1999). To ensure that this treatment led to proteasome inhibition, we performed a Western blot on lysates from cells in all conditions and specifically looked at ubiquitination. There was a slightly higher amount of ubiquitination in the treatment groups compared to the non-treated controls after normalizing for well loading as expected (*SI Appendix C*, Fig. C5A, B). Addition of 20nM of epo while simultaneously removing dox for 1 day (day 1 off dox and epo) also led to an accumulation of tau protein as with CQ (Fig. 4.4E). Similarly, as with CQ, there was an

approximate 1.5-fold increase compared to +dox and almost a 2-fold increase compared to day 1 off dox (Fig. 4.4F).

We next carried out a similar analysis on data from autophagy and proteasome inhibition experiments. PCA analysis showed that data from the CQ and epo treatment overlapped with data from day 1 off dox in the PCA space, suggesting that both conditions contain tau aggregate species having the physical characteristics of the full range of tau aggregate classes present. Interestingly, there was not a full overlap between data from the CQ and epo experiments in the PCA space, suggesting that they could possess slightly different tau aggregate sub-populations (*SI Appendix C,* Fig. C6A, B).

Finally, we used the machine learning based classification to predict the tau aggregate classes present upon CQ and epo treatment compared to untreated control conditions. Interestingly, the proportion of linear fibrils increased by 2-fold compared to other tau aggregate classes in cells treated with epo compared to day 1 off dox cells (Fig. 4.3C). On the other hand, the proportion of NFT Precursors and NFT-like structures slightly increased in cells treated with CQ (Fig. 4.3C). These results suggest that UPS is likely involved in the degradation of linear fibrils, which accumulate following proteasome inhibition (Fig. 4.5). Based on the results that linear fibrils also accumulate in 4-10 days off dox without treatment, it is possible that UPS becomes overwhelmed and can no longer degrade fibrils at these later time points (Fig. 4.5). Furthermore, our results also suggest that autophagy is more likely to be involved in the clearance of NFT precursors and NFTs, since these structures accumulate upon autophagy inhibition (Fig. 4.5). Branched fibrils could also be a by-product of breakdown of the NFT precursor and NFT tau aggregates by autophagy, in addition to smaller tau species like oligomers and monomers, which then associate with the microtubules (Fig. 4.5).
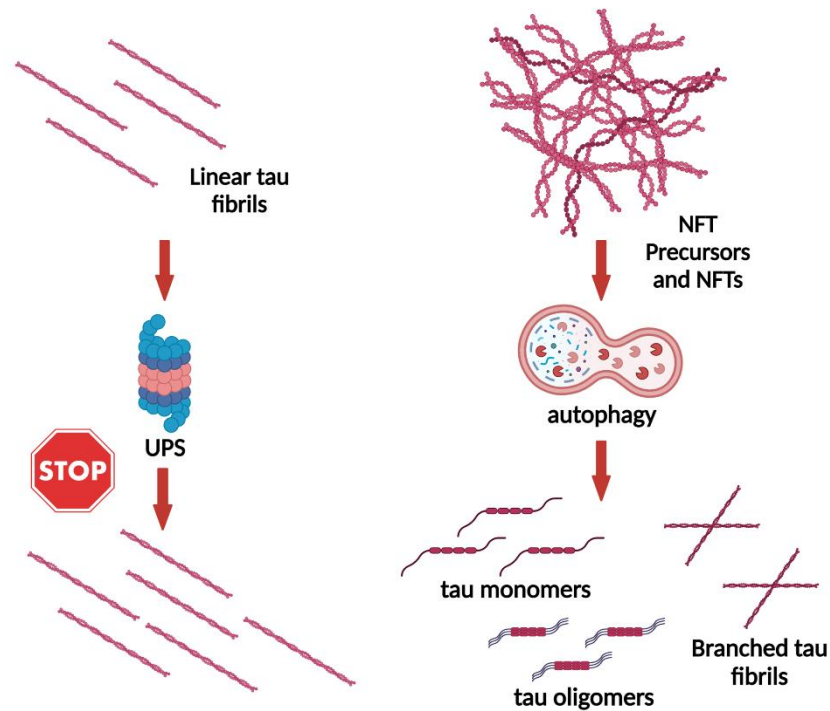
Figure 4.5. Working model of tau aggregate clearance. Created with BioRender.com. In the illustrated model, linear tau fibrils are degraded by UPS. However, UPS can become overwhelmed and fail to degrade the linear tau fibrils resulting in their accumulation. NFT Precursors and NFTs are degraded by autophagy. By-products of those could be branched tau fibrils in addition to tau monomers and oligomers.

Discussion

Here, we demonstrated using super-resolution microscopy that tau aggregates become degraded in the absence of soluble tau in an engineered cell model of tau aggregation. This finding recapitulates what has already been shown by (J. L. Guo et al. 2016) using this cell model. Understanding how tau aggregates become degraded in this engineered cell model could have important implications for the development of selective therapeutic approaches targeting tau aggregate clearance pathways to reverse neurodegeneration.

Quantitative analysis of our results showed that following a cease in soluble tau expression, the number of small tau aggregates (<500 localizations) was reduced first and then reached a plateau while the number of larger tau aggregates (>500 localizations) was reduced gradually over time. One interpretation could be that small tau aggregates get degraded first followed by larger tau aggregates which get degraded gradually over time. An alternative interpretation could be that large tau aggregates become broken down into smaller ones at later time points and those smaller aggregates then become degraded. In either case, it is highly likely that breakdown of large tau aggregates into smaller units takes place. In some cases, such breakdown of tau aggregates has been shown to exacerbate neurodegeneration by contributing to the generation of toxic tau fragments (Y. P. Wang et al. 2007). However, breakdown of tau aggregates also has the potential to facilitate tau aggregate clearance as chaperone proteins can associate more easily with tau fragments and facilitate their degradation (Yipeng Wang et al. 2009).

In the cell model we are using, clearance of tau aggregates is successful and by day 10 off dox, most NFT precursor and NFT aggregates have been cleared almost completely with a return to microtubule associated tau, which resembles more physiological state of tau localization. This result suggests that large tau aggregates are likely a sink for tau protein and once these large tau aggregates are cleared, the remaining tau has higher affinity for microtubules. The process of tau aggregate clearance is often full of roadblocks in tauopathies. Findings from this cell model likely do not fully recapitulate the complexity of the human brain, but elucidating how degradation occurs in this simpler system could offer direction regarding the main targets to focus on in the brain. Particularly, our findings using machine learning based shape classification of tau aggregates showed that linear tau fibrils increase in proportion over time, suggesting that these aggregates may be

harder to degrade. Understanding the reasons behind why this aggregate species is more resistant to degradation can potentially offer avenues for facilitating their clearance. Previously, we showed that these linear fibrils are enriched in hyperphosphorylation marks in Ser 202/Thr205 (Gyparaki et al. 2021). One potential explanation could be that hyperphosphorylation at these residues is refractive to tau degradation, a hypothesis that can be explored in future work.

We next examined the involvement of the two main degradation pathways: UPS and autophagy in the clearance of tau aggregates in Clone 4.1 cells. We showed that pharmacological inhibition of UPS or autophagy leads to an accumulation of tau aggregates. Interestingly, we found that autophagy inhibition led to an increase in NFT Precursors and NFTs. These results agree with the already existing literature where autophagy has been shown to degrade both soluble and insoluble forms of tau as well as both wild-type and mutant forms of tau (Dolan and Johnson 2010) (Y. Wang et al. 2010). UPS inhibition led to a greater increase in the number of linear fibrils than autophagy inhibition, which suggests that UPS could be involved in the clearing of those aggregate species to a greater extent than autophagy. An increase in tau accumulation following UPS inhibition is consistent with the literature (David et al. 2002) (Liu et al. 2009) (J. Y. Zhang et al. 2005). However, due to size limitations of the proteolytic core of the proteasome, tau aggregates are not thought to be degraded by UPS. Our findings indicate that the proteasome is possibly involved in more than the degradation of tau monomers and small oligomers as it was previously thought (Rubinsztein 2006). Based on our findings, we propose a model, where tau fibrils are targeted by UPS for degradation but UPS becomes overwhelmed and cannot properly degrade those structures leading to their accumulation. Moreover, we propose that NFT Precursors and NFTs are degraded by

autophagy and broken down into tau monomers and oligomers as well as tau branched fibrils. The branched fibrils remained similar in proportion throughout the different days following dox removal. This could be due to branched fibrils being a byproduct of degradation of larger structures and incomplete clearance of branched fibrils by autophagy. In fact, a similar behavior has been observed with α-synuclein, which is another aggregation-prone protein (Grassi et al. 2018). Trimming of α-synuclein into a smaller and more toxic aggregate structure is a result of a failed autophagic process. As a next step, it would be important to determine whether this model holds true in neurons, which could further inform therapeutic strategies targeting cellular degradation mechanisms.

Materials and Methods

A detailed description of the methods can be found in *SI Appendix C.* Briefly, a stable human embryonic kidney-derived QBI-293 cell lines (Clone 4.1) expressing full-length human tau T40 (2N4R or 4R) carrying the P301L mutation with a GFP tag, a kind gift from the V. Lee laboratory at the University of Pennsylvania, Philadelphia, PA, was used for experiments. Clone 4.1 is sorted from the parent Clone 4.0 cell line to enrich for large, compact tau aggregates after exogenous tau fibril addition. Clone 4.1 was maintained in Dox continuously (+dox) or Dox was removed from the culture media for several days to perform experiments (Day 1 off dox, Day 2 off dox etc). Pharmacological treatments of Clone 4.1 cells were performed by incubating the cells with media containing either 20nM epo or 30μM CQ. Cells were grown on chambered coverglass, fixed with ice cold methanol, and immunostained with GFP nanobody fused to AlexaFluor 647 prior to super-resolution microscopy using a Nanoimager from Oxford Nanoimaging.

CHAPTER 5. CONCLUSIONS AND FUTURE DIRECTIONS

In this dissertation, I have discussed my research findings on the nanoscale distribution of tau on microtubules and in tau aggregates as well as the characterization of different tau aggregate species in cell models of disease and how they are degraded by UPS and autophagy. In chapter 2, I showed that tau forms oligomeric complexes on microtubules that are different from those present in pathological conditions. Moreover, I found evidence supporting that microtubule-associated tau dimers/trimers grow in size in pathological conditions suggesting that aggregation could precede the dissociation of tau from the microtubules. In chapter 3, I showed that different tau aggregate species could be distinguished by the phosphorylation markers they possess reinforcing the idea of the existence of different tau strains. Finally, in chapter 4, I showed that in an engineered model of tauopathy, removal of soluble tau leads to clearance of tau protein as well as tau aggregates by degradation regulated by UPS and autophagy. The combination of super-resolution imaging and computational approaches I used allowed me to elucidate areas of limited understanding in the field of tauopathies. In the following sections, I have summarized some useful future directions and areas to explore based on the improved understanding we have from our findings.

Microtubule-associated tau oligomers in disease

The canonical disease-state theory for tauopathies posits that tau becomes mutated and/or hyperphosphorylated, dissociates from the microtubules and then aggregates. Our findings of microtubule-associated tau dimers/trimers in an engineered cell model of tauopathy as well as in neurons have recently challenged this traditional view. The idea that tau aggregation could be seeded on the microtubule by these dimers/trimers prior to

its dissociation significantly changes how we think of its mechanism of aggregation. More recently, (Cario et al. 2022) showed that the R5L mutation in the N-terminal domain of tau disrupted the formation of microtubule-associated tau patches (analogous to what we refer to as oligomers) but did not affect tau's microtubule affinity using an *in vitro* TIRF binding assay with taxol-stabilized microtubules. It would be interesting to explore this finding in neurons to study the effect of the R5L mutation and generally tau's N-terminal projection domain on the microtubule-associated tau oligomers and tau aggregation. Moreover, previously, single-molecule tracking revealed that tau dwells on a single microtubule for a very short time (∼40 ms) in what has been described as a kiss-and-hop interaction before hoping on to the next microtubule (Janning et al. 2014). These experiments were performed using a Halo-tagged tau fusion construct. Since microtubule-associated tau consists of tau oligomers in addition to monomers, a crucial future direction would be to explore whether this dynamic interaction of tau with the microtubules changes when tau exists in larger complexes. Additionally, it is worth exploring whether there is a cut-off number of the molecules in a tau oligomeric complex after which the complex cannot re-associate with the microtubules dynamically and therefore, falls off and continues to aggregate in the cytosol. Future findings in this direction would be critical for determining future therapeutic targets for tauopathies.

Distinguishing tau aggregates based on their post-translational modifications

Our work showed that it is possible to distinguish different tau aggregate species based on their shape and other characteristics such as their phosphorylation markers. One of the most unanswered questions despite the extensive research in the field is what exactly drives tau aggregation and whether it holds true for all types of tau aggregates. Based on what we know so far, different tauopathies have neurodegeneration in common but in

most cases, their clinical presentation differs and the tau aggregates present in each consist of different tau isoforms. To start, it is helpful to identify certain characteristics that drive aggregation and could be present in most tau aggregates. For instance, the Ser 202/Thr 205 phosphorylation site of tau combined with phosphorylation at Ser 208 and absence of phosphorylation at Ser262 has been shown to readily form fibers of tau *in vitro* without the addition of any aggregation inducer (Despres et al. 2017). However, it is not clear whether these phosphorylation markers are also present in smaller tau aggregates such as oligomers. Therefore, it would be crucial to characterize different stages of tau aggregate species and determine common phosphorylation markers as well as other post-translational modifications (PTMs) that perhaps are acquired in early stages and persist as well as others that are added along the way.

Most phosphorylation markers of tau are present on the C-terminal half of the protein (Flores-Rodríguez et al. 2015). Biochemical analysis of sarkosyl-insoluble tau from patients of different tauopathies shows distinct patterns of C-terminal tau fragments (Arai et al. 2004) (Taniguchi-Watanabe et al. 2016). Moreover, tau filaments extracted from patients of different tauopathies also exhibit ultrastructural differences at the atomic level as revealed by cryo-EM studies (Sanders et al. 2014) (Kaufman et al. 2016) (Arakhamia et al. 2020). More recently, such differences have been attributed to PTMs of tau and not limited to hyperphosphorylation (Arakhamia et al. 2020). Ubiquitination of tau residues and specifically, the C terminus of ubiquitin stabilizes the interprotofilament surface in filaments of tau from AD. (Arakhamia et al. 2020) proposed a model where the incorporation of ubiquitin into the tau protofilaments from AD and CBD could facilitate the inter-protofilament packing process and lead to ultrastructurally distinct polymorphs. The unsupervised machine learning approach we developed could offer insight into the

71

distinction of different tau aggregate species based on their shape and PTMs and could complement parallel work using cryo-EM and mass spectroscopy (MS) - based proteomics.

Exploiting autophagy and UPS to target different tau aggregate species

Determining how distinct tau aggregate species get degraded by autophagy or UPS could revolutionize therapies for tauopathies. To tackle this puzzle, we employed pharmacological treatments that inhibit UPS or autophagy and studied the tau aggregate populations which accumulate thereafter. In the future, we hope to expand our current approach to also implement supervised machine learning in combination with modeling. The goal is to create models for each type of tau aggregate present in a sample and examine whether the same tau aggregate populations are present under various treatment conditions. This approach could tell us if specific tau aggregates are resistant to degradation as well as which specific tau aggregates are more efficiently cleared by UPS or autophagy. This approach would not only be useful for segmented tau aggregates from super-resolution images but could also be used in combination with different types of light as well as electron microscopy samples. For instance, analyzing tau aggregates from post-mortem tauopathy brain tissue, which contain a specific set of PTM markers and comparing those from different tauopathies could facilitate the detection of distinct tau strains.

An important PTM, which also regulates degradation is ubiquitination. Ubiquitin most commonly, marks proteins for degradation by the proteasome and it contains seven lysine (K) chains (Swatek and Komander 2016). How these residues become ubiquitinated can determine the fate of a protein. K48-linkage has been implicated in proteasomal

degradation, whereas K63-linkage has been implicated in autophagy (Swatek and Komander 2016) (J. M. M. Tan et al. 2008). However, recently, K63-linked ubiquitination of AD brain derived tau oligomers was shown to contribute to AD pathogenesis (Puangmalai et al. 2022). Therefore, examining the type of ubiquitin linkage in distinct tau aggregates from different tauopathies would also contribute to our understanding of tau strains but also which tau aggregate species are potentially targeted for degradation by the proteasome and/or autophagy.

Furthermore, understanding how autophagy and UPS malfunction in tauopathies, whether their malfunction is caused solely by the presence of an overwhelming amount of tau aggregates and whether it is influenced by additional factors is essential. In the future, monitoring the efficiency of autophagy and the UPS with inducible systems of tau aggregation similar to the cell model we used could elucidate whether failure to clear aggregates could be due to increasing tau aggregate concentration or due to the presence of specific tau aggregate species. Previously, age-dependent increases in phosphorylated tau have led to defective autophagy in AD (Reddy and Oliver 2019). Moreover, other studies have shown that accumulation of tau aggregates inhibits the fusion of the autophagosome with the lysosome in AD (Feng et al. 2020). Interestingly, proteasomal activity but not tau protein level has been shown to decrease in AD affected brain regions compared to unaffected (Keller, Hanni, and Markesbery 2000). An interesting direction would be to explore whether tau oligomers specifically impair the function of the proteasome, as previously other protein oligomers seen in neurodegenerative diseases have been implicated in an oligomer-driven impairment of the 20S proteasome that might also hold true for tau (Thibaudeau, Anderson, and Smith 2018).

Tau aggregates and membrane interactions

In recent years, we have gained a better understanding into how tau aggregates are transported from one neuron to the next. In fact, both tau monomers and pathological tau aggregates can be released from a donor cell and taken up by a recipient cell (De La-Rocque et al. 2021). Moreover, there is evidence that tau secretion can occur in a vesicle-dependent way through exosomes or ectosomes but also via more unconventional, non-vesicular pathways involving translocation across the plasma membrane (G. Lee and Leugers 2012) (Dujardin et al. 2014) (Katsinelos et al. 2018) (Merezhko et al. 2018). Therefore, understanding how different tau aggregates species are interacting with the plasma membrane and transported to recipient cells would have important implications for the spread of neurodegenerative diseases. Our super-resolution images can be acquired using the Total Internal Reflection Fluorescence Microscopy (TIRFM) modality, which is ideal for studying the membrane since it can illuminate fluorophores near the membrane through the generation of an evanescent field (Fish 2009). An important future direction would be to image tau along with components of the plasma membrane and examine the distribution of the protein across the plasma membrane in physiological and pathological conditions. In particular, it would be important to explore how tau PTMs and specifically phosphorylation affect its interaction with the membrane. The existing data is conflicting so far because studies have used different cell lines containing different tau species and studied different phosphorylation sites, making it challenging to reach a consensus (Bok et al. 2021). It is speculated that phosphorylation of physiological tau has an inhibitory effect on its association with the membrane whereas phosphorylation of tau oligomers and fibrils has the opposite effect (Bok et al. 2021). However, these findings need to be carefully validated.

74

Furthermore, once tau dissociates from the microtubules, it is likely that it interacts with other membranous organelles such as the endoplasmic reticulum (ER) and mitochondria. Increased tau has been observed on the surface of the rough ER in the brains of AD patients (Perreault et al. 2009). Additionally, increased mitochondria-ER contacts have also been reported in the brains of those patients, which could be related to the increased tau also observed (Perreault et al. 2009). Elucidating the involvement of tau in the regulation of mitochondria-ER contacts would shed light on other ways it could be contributing to neurodegeneration by altering mitochondrial dynamics, apoptosis, lipid metabolism among other processes (Csordás, Weaver, and Hajnóczky 2018) (Moltedo, Remondelli, and Amodio 2019).

APPENDICES

APPENDIX A.

Supplementary Materials and Methods for Chapter 2

Cell culture

A stable cell line expressing 3R-WT-GFP tau was derived from African green monkey (*Cercopithecus aethiops*) kidney epithelial cells (BSC-1; CCL-26; American Type Culture Collection). For some experiments, BSC-1 cells were transfected with either a 4R-WT-GFP tau construct or a 4R-WT tau construct to transiently express tau (see Figures S1A, S2B, S3G,H). Cells were grown in complete growth medium (Eagle's minimum essential medium with Earle's salts and non-essential amino acids plus 10% FBS, 1mM sodium pyriuvate, 2mM L-glutamine, 500 ug/ml Geneticin [G418 Sulfate; Thermo Fisher Scientific] and penicillin-streptomycin) in a 37°C incubator containing 5% CO_2.

Two stable human embryonic kidney-derived QBI-293 cell lines (Clone 4.0, Clone 4.1) expressing full length human tau T40 (2N4R) carrying the P301L mutation with a GFP tag, a kind gift from the V. Lee lab at the University of Pennsylvania, were used for the majority of experiments. Clone 4.1 was originally sorted from the parent Clone 4.0 cells to enrich for large compact tau aggregates after exogenous tau fibril addition (J. L. Guo et al. 2016). Cells were grown in Dulbecco's modified Eagle's medium supplemented with 10% tetracycline-screened fetal bovine serum (FBS), 1% pyruvate (10mM), 1% penicillin-streptomycin and L-glutamine (20 mM), 5ug/ml blasticidin, 200ug/ml Zeozin and were maintained in a 37°C incubator containing 5% CO_2. Clone 4.1 was maintained in media containing 100ng/mL of Doxycycline (Dox), whereas 100ng/nL of Dox was only added in the media overnight (16-24 h) before fixation for Clone 4.0 unless otherwise stated in order

to express the 4R-P301L-GFP tau construct. For all imaging, cells were plated on eight-well Lab-Tek 1 coverglass chambers (Nunc).

E18 Sprague-Dawley rat hippocampal neurons were obtained in suspension from the Neuron Culture Service Center at the University of Pennsylvania. Neurons were plated in eight-well Lab-Tek 1 coverglass chambers (Nunc) which had been precoated with 0.5 mg/ml poly-L-lysine (Sigma-Aldrich) 24 hr before plating. Neurons were cultured in maintenance media consisting of Neurobasal (Gibco) supplemented with 2mM GlutaMAX, 100 U/ml penicillin, 100 mg/ml streptomycin, and 2% B27 (Thermo Fisher Scientific) in a 37°C incubator containing 5% CO_2.

Cell lysate extraction and Western blotting

Cell lysate was extracted from QBI cells with Dox-regulated expression of 4R-P301L-GFP tau (Clone 4.0 grown in the presence (+) or absence (-) of Dox and Clone 4.1 grown in Dox) by RIPA (Radioimmunoprecipitation) buffer containing phosphatase and protease inhibitors and incubated on ice for 15 min. Lysates were then centrifuged at maximum speed on a tabletop centrifuge for 30 min at 4 °C. Protein concentration was determined using the Bradford assay. 2-3ug of protein per sample were resolved in 4-12% Bis-Tris NuPAGE (polyacrylamide) gels, transferred to nitrocellulose membranes, and blocked in Odyssey blocking buffer (Li-Cor Biosciences) before probing with Tau-5 antibody (see Table S.2.1). The blots were further incubated with IRDye labeled secondary antibodies and scanned using ODY-2816 Imager (Li-Cor Biosciences). GAPDH was used as a loading control. Image analysis was performed using Image Studio Lite software (LI-COR). Fluorescent band intensity was normalized to the GAPDH loading control.

Immunostaining

Two different fixation protocols were tested: paraformaldehyde (PFA) or methanol fixation. For PFA fixation, cells were initially washed with PBS for three times (5 min per wash), then fixed with 4% PFA for 10 min at room temperature and washed again three times (5 min per wash) with PBS following fixation. Since PFA fixation disrupted tau localization, for the experiments reported in the manuscript, cells were fixed using methanol fixation. Briefly, cells were first incubated with microtubule stabilizing buffer (MTSB: 15g PIPES, 1.9g EGTA, 1.32 $MgSO_4 \cdot 7H_2O$, 5g KOH, H_2O to a liter, pH=7) for 3 min and then ice cold methanol was added in the buffer for 3 min. Following this short incubation, cells were washed with MTSB twice. Cells were then blocked for 1hr using 4% (wt/vol) BSA in PBS. They were then incubated with the appropriate dilution of primary and secondary antibodies (or nanobody) in blocking buffer consisting of 3% (wt/vol) BSA and 0.2% Triton X-100 (vol/vol; Thermo Fisher Scientific) in PBS. Cells were washed with washing buffer (0.2% BSA and 0.05% Triton X-100; Thermo Fisher Scientific) between antibody/nanobody incubations. A list of antibodies/nanobodies used in this study is provided in Table S.2.1. The nanobody we used was GFP VHH, recombinant binding protein (gt-250, Chromotek). The secondary antibodies we used were AffiniPure goat anti-mouse IgG (H+L, 115-005-003; Jackson ImmunoResearch) at a dilution of 1:100, and AffiniPure donkey anti-rabbit IgG (H+L, 711-005-152; Jackson ImmunoResearch) at a dilution of 1:100. The nanobody and the secondary antibodies used in this study were custom-labeled with an Alexa Fluor A647 or Alexa Fluor 405-Alexa Fluor 488 and an Alexa Fluor 405-Alexa Fluor A647 or Alexa Fluor 405-Alexa Fluor 488 activator/reporter dye pair combination at 0.12-0.15 mg/ml concentration, respectively (Bates et al. 2007).

SMLM imaging

SMLM was acquired using an Oxford Nanoimaging system. To avoid bias, images were randomly acquired and all acquired images were included in the analysis unless there was substantial drift present in the images, which could not be corrected by post-processing. The Nanoimager-S microscope had the following configuration: 405-, 488-, 561- and 640-nm lasers, 498-551- and 576-620-nm band-pass filters in channel 1, and 666-705-nm band-pass filters in channel 2, 100 x 1.4 NA oil immersion objective (Olympus), and a Hamamatsu Flash 4 V3 sCMOS camera. Localization microscopy images were acquired with 15 ms exposure for 50,000 frames. For multi-color SMLM, 110,000 frames with 15 ms exposure were acquired with sequential laser activation. The images were then processed using the NimOS localization software (Oxford Nanoimaging).

Data analysis

Voronoi Tesselation Analysis

Localizations were exported in .csv format using the NimOS localization software and converted to .bin files using MATLAB R2017a. The rendered SMLM images were cropped using the AFIB plugin in ImageJ (National Institutes of Health) (Schindelin et al. 2012). Voronoi Tesselation Analysis was performed in MATLAB R2017a similarly to (Otterstrom et al. 2019) (Levet et al. 2015) (Andronov et al. 2016). First, a Voronoi threshold was chosen manually to define a Voronoi cluster as a collection of Voronoi polygons with areas smaller than the given threshold. We confirmed that the selected threshold led to proper segmentation of the super-resolution images visually and used the same threshold across different conditions for consistency. In the case of Clone 4.0, we cropped regions in which

single microtubules were visible and avoided dense areas consisting of microtubule bundles to avoid segmentation errors due to inability to resolve the tau associated with individual microtubules within these bundles. The x and y coordinates from the localizations were processed by the "delaunayTriangulation" function and then the 'Voronoidiagram" function to generate Voronoi polygons. The Voronoi polygon areas were calculated from the shoelace algorithm. A new molecule list assigning localizations to different channels (0-9) according to their Voronoi area was then generated. Next, these localizations were put into different clusters and their cluster statistics were generated and used for analysis. The different clusters were pseudocolored based on their channel (0-9) and visualized using a custom-written software, Insight3 (provided by B. Huang, University of California, San Francisco, San Francisco, CA; (Huang et al. 2008).

Outlier Removal Analysis

In the segmented clusters, there is a positive correlation between the cluster area and the number of localizations per cluster. However, clusters corresponding to imaging artefacts (e.g. molecules that do not photoswitch) fall outside of this positive correlation as they contain a large number of localizations but small area. We used this positive correlation between cluster area and the number of localizations to filter clusters corresponding to imaging artefacts. This procedure removed 0.1316% of clusters from the data.

GFP nanobody Calibration

We determined the number of localizations corresponding to a single tau molecule labeled with the GFP-nanobody by carrying out super-resolution imaging under dilute labeling conditions corresponding to a 1:10000 dilution of the GFP-nanobody. We segmented

these images using Voronoi segmentation as described above and determined the number of localizations per cluster. The number of localizations distribution was fit to a log normal function to extract two parameters mu and sigma corresponding to the log normal distribution function (f1). The above-mentioned distribution function (f1) and its convolution with itself two times (f2 = f1*f1) and three times (f3 = f2*f1) is used to determine the percentage of single-tau molecules, monomers and oligomers by fitting a linear combination of these functions to the distribution of the number of localizations per cluster from the actual experiment corresponding to 1:100 dilution of the GFP-nanobody as previously described (Cella Zanacchi et al. 2017).

SMLM Colocalization Analysis

Colocalization analysis was performed using a custom-built algorithm in MATLAB R2017a for all multi-color SMLM data. Regions with similar tau density were cropped for quantitative analysis, avoiding overcrowded regions to minimize segmentation errors. The threshold on Voronoi polygon size was kept consistent between different conditions and clusters having fewer than 5 localizations were filtered. First, a list of reference boundaries from the reference cluster (channel 1) is obtained. The boundaries are then extended by a set radius (30 nm) and the points inside the boundary are obtained. Next, the points from the non-reference cluster (channel 2) that fall into the reference cluster are determined. The percentage of colocalized points in the non-reference clusters is also determined. A threshold of 40% colocalization is required for a cluster to be considered colocalized and anything below 40% is considered isolated. This threshold was determined after qualitative examination of the colocalized clusters visually and used throughout the analysis for consistency.

Distance Distribution Correction (DDC) Analysis

The DDC algorithm developed by (Bohrer et al. 2019) was used to correct for blinking in SMLM images acquired using the GFP nanobody fused to Alexa Fluor A647 or Alexa Fluor 405-Alexa Fluor 488 without 405nm activation as previously explained.

Statistical Analysis

Non-parametric Mann-Whitney tests were performed using OriginPro 2017 software for all data imaging data sets. A paired student t-test was performed for the fixation control experiment in Fig. A3B.

Supplementary Figures for Chapter 2
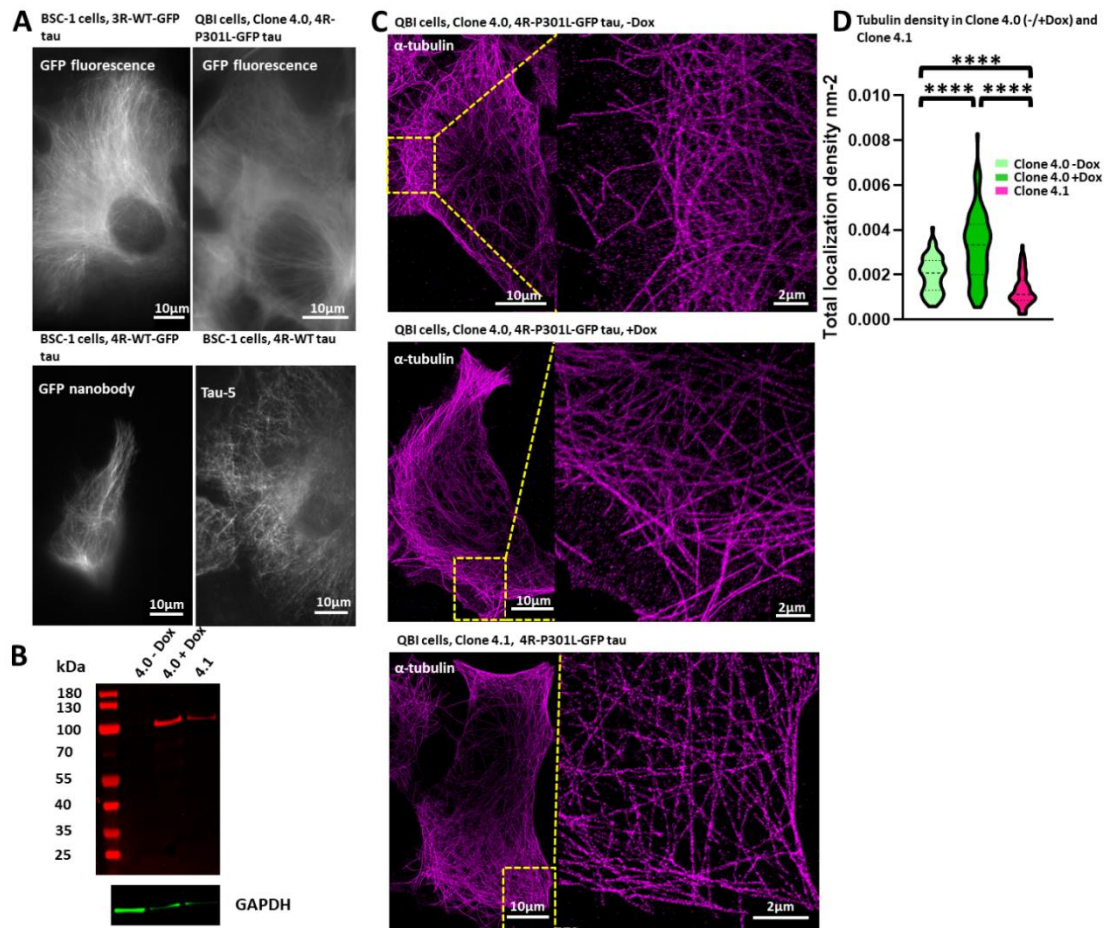
Fig. A1: Tau localization and microtubule network density in the engineered cell lines. A. Wide-field images of GFP fluorescence in live BSC-1 cells expressing 3R-WT-GFP tau, live Clone 4.0 cells expressing 4R-P301L-GFP tau after overnight Dox induction of tau expression, fixed BSC-1 cells expressing 4R-WT-GFP tau stained by GFP nanobody conjugated to AlexaFluor 647, fixed BSC-1 cells expressing 4R-WT tau stained by Tau-5 antibody, which was labeled with a secondary mouse antibody conjugated to AlexaFluor 647. B. Western Blot showing tau and GAPDH (loading control) from lysates of Clone 4.0 cells cultured in the absence of Dox (4.0 –Dox), Clone 4.0 cells expressing 4R-P301L-GFP tau after overnight Dox induction (4.0 +Dox) and Clone 4.1 cells maintained in Dox

and expressing 4R-P301L-GFP tau (4.1). C. Super-resolution image and zoom of α-tubulin in Clone 4.0 cells in the absence of Dox induction (i.e no GFP-tau expression) (top panel). Super-resolution image and zoom of α-tubulin in Clone 4.0 cells expressing 4R-P301L-GFP tau after overnight Dox induction of tau expression (non-aggregated tau expression) (middle panel). Super-resolution image and zoom of α-tubulin in Clone 4.1 cells maintained in Dox and expressing 4R-P301L-tau (aggregated tau expression) (bottom panel). D. Violin plots showing the total tubulin localization density per nm^2 measured by calculating the total number of detected localizations in the super-resolution images per unit area of the cell. Total localization density was measured in Clone 4.0 cells cultured without Dox induction of tau expression (-Dox, light green), Clone 4.0 cells after overnight Dox induction of 4R-P301L-GFP tau expression (+Dox, dark green) and in Clone 4.1 cells maintained in Dox and expressing 4R-P301L-GFP tau (pink). Tubulin localization density is proportional to microtubule network density. The dashed lines indicate the median and the dotted lines indicate the 25th and 75th percentile (Clone 4.0 -Dox: n=12 cells, n=2 experiments, Clone 4.0 +Dox: n=10 cells, n=2 experiments, Clone 4.1: n=9 cells, n=2 experiments). ****, p<0.0001.
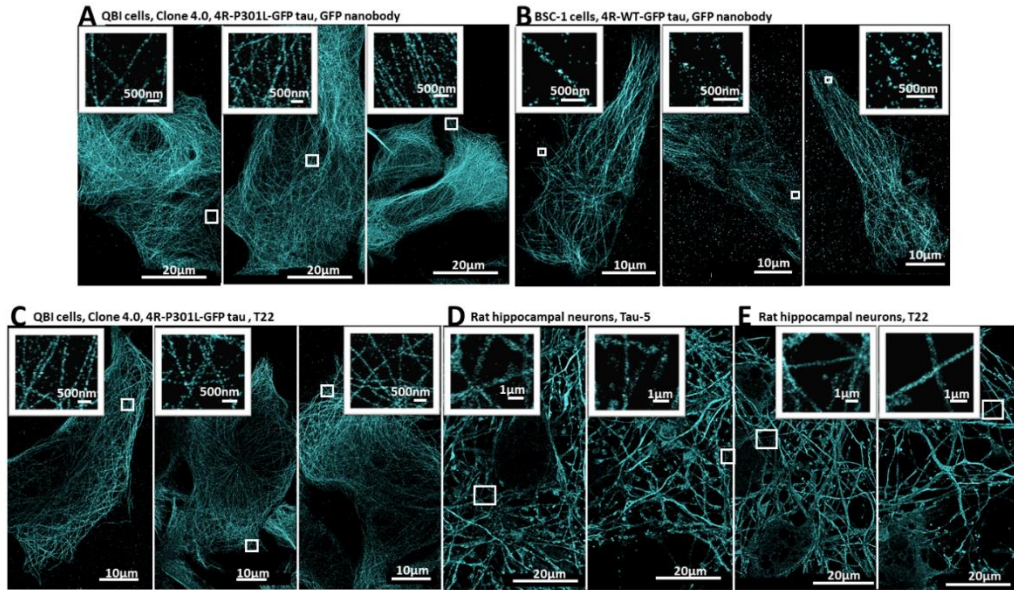
Fig. A2: Representative images of tau in different cell lines used in this study. A. Super-resolution images of tau in Clone 4.0 expressing 4R-P301L-GFP tau after overnight Dox induction of tau expression, stained with a GFP nanobody conjugated to AlexaFluor 647. B. Super-resolution images of tau in BSC-1 cells expressing 4R-WT-GFP tau, stained with GFP nanobody conjugated to AlexaFluor 647. C. Super-resolution images of oligomeric tau detected by the tau oligomer specific T22 antibody in Clone 4.0 expressing 4R-P301L-GFP tau after overnight induction of tau expression. D. Super-resolution images of tau in rat hippocampal neurons, stained with Tau-5 antibody, which detects all tau isoforms. E. Super-resolution images of oligomeric tau detected by tau oligomer specific T22 antibody in rat hippocampal neurons.
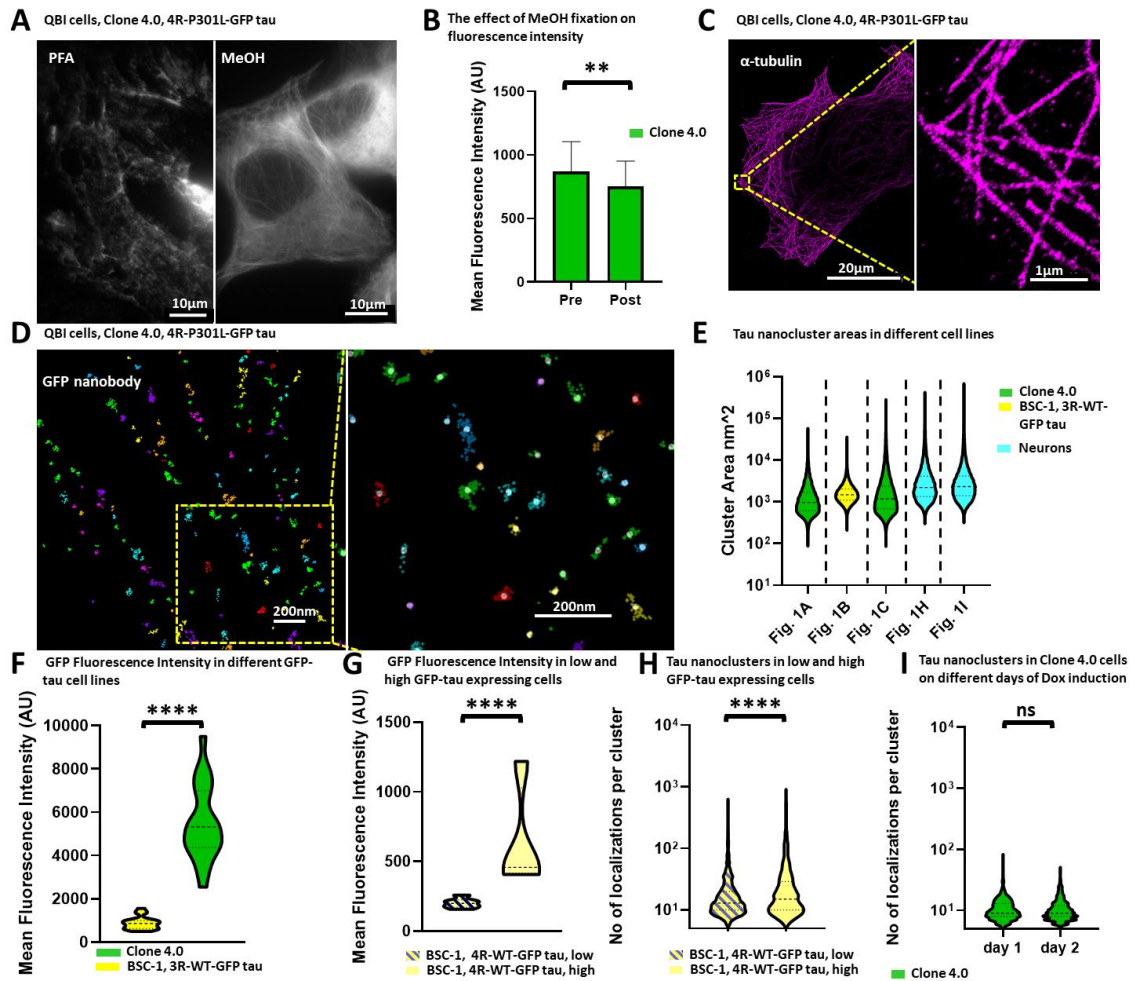
Fig. A3: Tau forms nano-clusters on microtubules.

A. Wide-field images of GFP fluorescence in Clone 4.0 cells expressing 4R-P301L-GFP tau after overnight Dox induction of tau expression, fixed with either PFA or MeOH. B. Bar plots showing the mean fluorescence intensity of GFP-tau in AU before (pre-) and (post-) methanol fixation in Clone 4.0 cells expressing 4R-P301L-GFP tau after overnight Dox induction of tau expression (n=5 cells). **, $p<0.01$. C. Super-resolution image of α-tubulin staining in Clone 4.0 cells expressing 4R-P301L-GFP tau after overnight Dox induction of tau expression, and zoom. D. Voronoi segmentation of a region of a Clone 4.0 cell expressing 4R-P301L-GFP tau after overnight Dox induction of tau expression and zoom.

The different colors represent different nano-clusters whose center is represented by a white dot. Individual fluorophore localizations are represented as color-coded crosses. Localizations that are in close spatial proximity are segmented as belonging to the same nano-cluster. E. Violin plots showing the area of Voronoi segmented nano-clusters in nm^2 in the different cell lines used in this study (green: Clone 4.0 cells expressing 4R-P301L-GFP tau after overnight Dox induction of tau expression; yellow: stable BSC-1 cells constitutively expressing 3R-WT-GFP tau; and cyan: rat hippocampal neurons). Plots for Fig. 1A, Fig. 1B correspond to the quantification of tau nano-clusters stained and imaged with a GFP-nanobody. Plot for Fig. 1H corresponds to the quantification of tau nano-clusters stained and imaged with a Tau-5 antibody. Plots for Fig. 1C and 1I correspond to the quantification of tau nano-clusters stained and imaged with the oligomeric T22 antibody. The dashed lines indicate the median and the dotted lines indicate the 25th and 75th percentile (Fig.1A: n=15 cells, n= 3 experiments, Fig.1B: n=15 cells, n=2 experiments, Fig.1C: n=19 cells, n=3 experiments, Fig.1H n=3 cells, Fig.1I: n=3 cells). F. Violin plots showing the mean fluorescence intensity (AU) in conventional fluorescence images of tau in live BSC-1 cells expressing 3R-WT-GFP tau as well as in live Clone 4.0 cells expressing 4R-P301L-GFP tau after overnight Dox induction of tau expression. The fluorescence intensity of GFP-tau is proportional to the tau expression level in the two cell lines. The dashed lines indicate the median and the dotted lines indicate the 25th and 75th percentile (3R-WT-GFP tau: n=20 cells, Clone 4.0: n=20 cells). ****, $p<0.0001$. G. Violin plots showing the mean fluorescence intensity (AU) in conventional fluorescence images of tau in live BSC-1 cells, transiently transfected with 4R-WT-GFP tau, that either express low (yellow with lines) or high (yellow without lines) levels of GFP-tau. The dashed lines indicate the median and the dotted lines indicate the 25th and 75th percentile (low: n= 6 cells, high: n= 4 cells). ****, $p<0.0001$. H. Violin plots showing the number of localizations

per nano-cluster in super-resolution images of tau in BSC-1 cells, transiently transfected with 4R-WT-GFP tau, that either express low (yellow with lines) or high (yellow without lines) levels of GFP-tau. The dashed lines indicate the median and the dotted lines indicate the 25th and 75th percentile (low: n= 6 cells, high: n= 4 cells). ****, $p<0.0001$. I. Violin plots showing the number of localizations per nano-cluster in super-resolution images of tau in Clone 4.0 cells expressing 4R-P301L-GFP tau that have been induced with Dox for either 1 day or 2 days. The dashed lines indicate the median and the dotted lines indicate the 25th and 75th percentile (day 1: n= 6 cells, day 2: n= 7 cells). ns, non-significant.
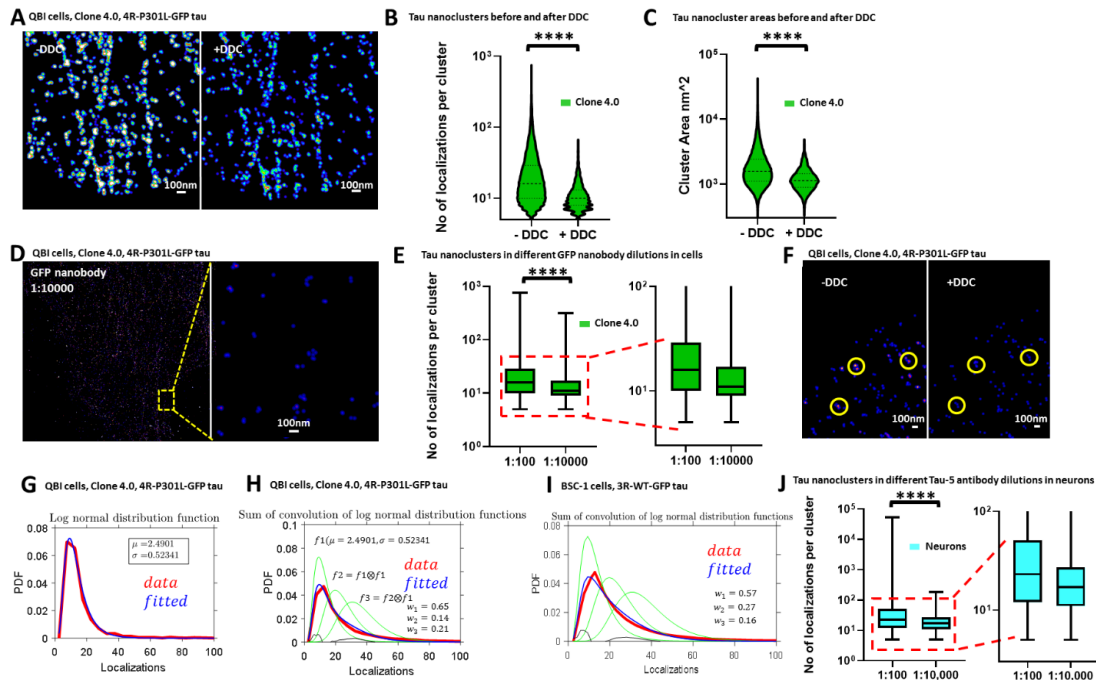
Fig. A4: Tau nano-clusters consist of monomers, dimers and trimers. A. Super-resolution images of GFP-tau in Clone 4.0 cells expressing 4R-P301L-GFP tau after overnight Dox induction of tau expression and before/after DDC correction. Color map corresponds to localization density with less dense regions shown in blue and denser regions shown in red. B. Violin plots showing the number of localizations per Voronoi segmented nano-cluster in Clone 4.0 cells expressing 4R-P301L-GFP tau after overnight Dox induction of tau expression and before/after DDC correction. The dashed lines indicate the median and the dotted lines indicate the 25th and 75th percentile (n=15 cells, n=3 experiments). ****, p<0.0001. C. Violin plots showing the area of Voronoi segmented nano-clusters in nm^2 in Clone 4.0 cells expressing 4R-P301L-GFP tau after overnight Dox induction of tau expression and before/after DDC correction. The dashed lines indicate the median and the dotted lines indicate the 25th and 75th percentile (n=15 cells, n=3 experiments). ****, p<0.0001. D. Super-resolution image of tau stained with GFP nanobody conjugated to AlexaFluor 647 in Clone 4.0 cells expressing 4R-P301L-GFP tau after overnight Dox induction of tau expression, where the GFP nanobody has been diluted 100-fold more than in the usual imaging conditions and zoom. Color map corresponds to localization density with less dense regions shown in blue and denser regions shown in red. E. Box plots showing the number of localizations per Voronoi segmented nano-cluster in normal labeling conditions corresponding to 1:100 dilution of the GFP nanobody and in dilute labeling conditions corresponding to 1:10,000 dilution of the nanobody. (1:100: n=15 cells, n=3 experiments, 1:10,000: n=5 cells) in Clone 4.0 cells expressing 4R-P301L-GFP tau after overnight Dox induction of tau expression. Box corresponds to 25-75 percentile, line corresponds to median and whiskers correspond to the minimum and maximum. A zoom of the box plot is shown as inset. ****, p<0.0001. F. Super-resolution images of tau in Clone 4.0 cells expressing 4R-P301L-GFP tau after overnight Dox induction of tau

expression, where the GFP nanobody has been diluted 100-fold more (1:10,000) than in the usual imaging conditions, before and after DDC correction. Color map corresponds to localization density with less dense regions shown in blue and denser regions shown in red. Yellow circles indicate GFP tau nano-clusters before and after DDC correction. G. Plot showing the number of localizations per nano-cluster under dilute labeling conditions (red) and the log normal fit (blue) used as calibration function (f_1) for monomeric tau in Clone 4.0 cells expressing 4R-P301L-GFP tau after overnight Dox induction of tau expression and stained with GFP nanobody conjugated to AlexaFluor 647. H. Plot showing the number of localizations per nano-cluster under normal (experimental) labeling conditions (red) in Clone 4.0 cells expressing 4R-P301L-GFP tau after overnight Dox induction of tau expression, dimeric and trimeric calibration functions (f_2 and f_3) (green) obtained by linear convolution of the monomeric calibration function (f_1) obtained from the log normal fit in (G), and the fit of the experimental data to a combination of f_1, f_2 and f_3 (blue) with weights w_1, w_2 and w_3 corresponding to the proportion of monomers, dimers and trimers. I. Plot showing the number of localizations per nano-cluster under normal (experimental) labeling conditions (red) in BSC-1 cells expressing 3R-WT-GFP tau, dimeric and trimeric calibration functions (f_2 and f_3) (green) obtained by linear convolution of the monomeric calibration function (f_1) obtained from the log normal fit in (G), and the fit of the experimental data to a combination of f_1, f_2 and f_3 (blue) with weights w_1, w_2 and w_3 corresponding to the proportion of monomers, dimers and trimers. J. Box plots showing the number of localizations per Voronoi segmented nano-cluster in normal labeling conditions corresponding to 1:100 dilution of the Tau-5 primary antibody and the secondary anti-mouse antibody labeled with AlexaFluor 647 and in dilute labeling conditions corresponding to 1:10,000 dilution of the Tau-5 primary antibody and 1:100 dilution of the anti-mouse secondary antibody labeled with AlexaFluor 647 in rat

hippocampal neurons. (1:100: n=7 cells, n=2 experiments, 1:10,000: n=6 cells, n=2 experiments). Box corresponds to 25-75 percentile, line corresponds to median and whiskers correspond to the minimum and maximum. A zoom of the box plot is shown as inset. ****, $p<0.0001$.

A QBI cells, Clone 4.1, 4R-P301L-GFP tau

B Tau nanocluster areas in Clones 4.0 & 4.1

C QBI cells, Clone 4.1, 4R-P301L-GFP tau

Sum of convolution of log normal distribution functions

$w_1 = 0.57$
$w_2 = 0.17$
$w_3 = 0.07$
$w_4 = 0.09$
$w_5 = 0.01$
$w_6 = 0.01$
$w_7 = 0.08$
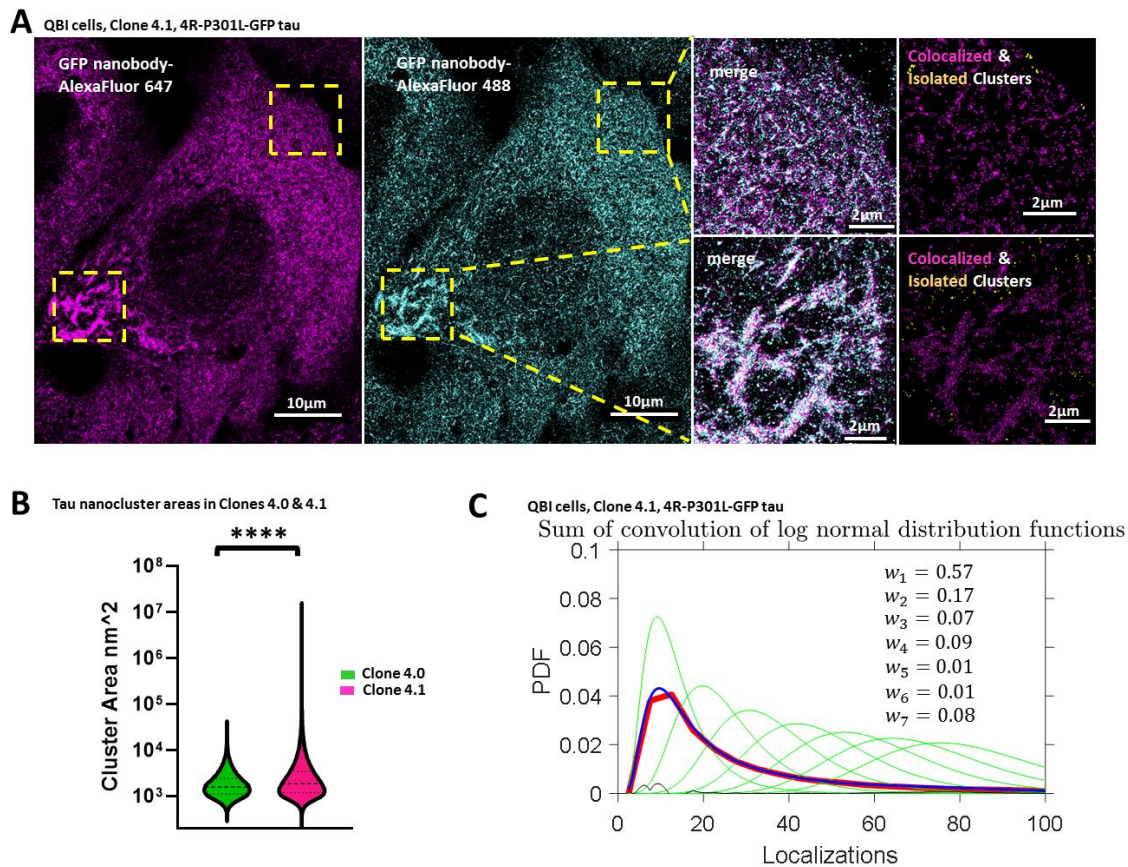
Fig. A5: Tau oligomers in Clone 4.1 cells contain more tau protein than the tau oligomers in Clone 4.0 cells. A. Two-color super-resolution images of tau stained with GFP nanobody conjugated to AlexaFluor 647 (magenta), or AlexaFluor 488 (cyan) and zoomed in overlay of two different regions (yellow boxes) in Clone 4.1 cells maintained in Dox and expressing

4R-P301L-GFP tau. The results of the co-localization analysis are shown in which tau structures imaged with AlexaFluor488 that co-localize with tau structures imaged with AlexaFluor647 are shown in magenta and isolated tau structures imaged with AlexaFluor488 that did not co-localize with tau structures imaged with AlexaFluor647 are shown in yellow. B. Violin plots showing the area of Voronoi segmented nano-clusters in nm^2 in Clone 4.0 cells expressing 4R-P301L-GFP tau after overnight Dox induction of tau expression (green) and Voronoi segmented tau objects in Clone 4.1 maintained in Dox and expressing 4R-P301L-GFP tau after overnight Dox induction of tau expression (pink). The dashed lines indicate the median and the dotted lines indicate the 25th and 75th percentile (Clone 4.0: n=15 cells, n=3 experiments, Clone 4.1: n=20 cells, n=3 experiments). ****, $p<0.0001$. C. Plot showing the number of localizations per tau object under normal (experimental) labeling conditions (red) in Clone 4.1 cells maintained in Dox and expressing 4R-P301L-GFP tau, dimeric-heptameric calibration functions (f_2-f_7) (green) obtained by linear convolution of the monomeric calibration function (f_1) obtained from the log normal fit in (Fig. A4G), and the fit of the experimental data to a combination of f_1-f_7 (blue) with weights w_1-w_7 corresponding to the proportion of monomers, dimers, trimers and higher order oligomers.
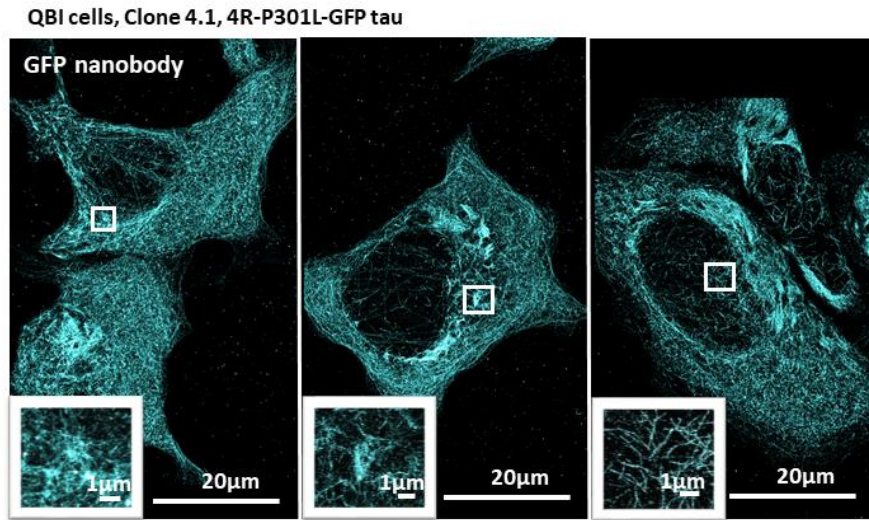
Fig. A6: Representative images of tau in Clone 4.1 cells maintained in Dox and expressing 4R-P301L-GFP tau in an aggregated state. Super-resolution images of tau in Clone 4.1 cells maintained in Dox and expressing 4R-P301L-GFP tau, stained with GFP nanobody conjugated to AlexaFluor 647.

Antibody	Host species	Catalog number	Vendor
α-tubulin	Rabbit	ab18251	Abcam
T22	Rabbit	ABN454	Sigma-Aldrich
Thr231	Mouse	MN1040	ThermoFisher Scientific
AT8	Mouse	MN1020	ThermoFisher Scientific
GFP Binding Protein	Alpaca	gt-250	ChromoTek
Tau-5	Mouse	AHB0042	ThermoFisher Scientific
GAPDH	Mouse	A01622-40	GenScript

Table S.2.1. Antibodies used in this study

APPENDIX B.

Supplementary Materials and Methods for Chapter 3

Data analysis

Iterative Hierarchical Clustering (constrained-relative standard deviation (c-RSD)

In order to segment the localized points in the super-resolution images into "objects" we performed a density-based clustering algorithm (DBSCAN) (Ester et al. 1996). DBSCAN requires two input parameters for segmentation: the minimum number of points (k) within a search radius (epsilon). We chose a minimum number of five localizations per object as a threshold for the segmentation (k = 5). To determine the search radius (epsilon) in an unbiased manner, we employed the elbow method. We first calculated the 4th nearest neighbor distances (NNDs) (k-1) between each of the localizations in the entire STORM image. We then sorted and plotted the NNDs and determined the value corresponding to the elbow point of this sorted distribution. The distance corresponding to the elbow point was used as the search radius in the DBSCAN algorithm. After running the DBSCAN algorithm on the entire STORM image, localizations were segmented into objects. In order to classify these objects into unique classes we next extracted their features. In our classification algorithm we considered 8 features describing each object. To determine the most relevant features to use in the classification, we first performed a PCA analysis on these objects to obtain the two axes corresponding to the most variation between the localization points. The 8 features were the number of localizations per object, object area, number of localizations in the upper-left, upper-right, lower-left, and lower-right quarters of the object and the length corresponding to the major and minor axes of the object. To

95

classify the objects based on these 8 features, we used agglomerative Hierarchical clustering algorithm (Rokach and Maimon 2006). In Hierarchical clustering, there is no a priori assumption on the number of classes. We found that the Hierarchical clustering alone over-estimated the number of classes, and often objects having very similar features were classified into distinct classes. In order to overcome this problem, we developed an iterative Hierarchical clustering algorithm, that we named Iterative Hierarchical Clustering (constrained-relative standard deviation (c-RSD)). We imposed a threshold on the coefficient of variation (ratio of the standard deviation to the mean) on two of the features (length and width of the object). First, we constructed a linkage (dendrogram tree) by calculating the distance between each of the objects in the 8th dimensional space. After forming the dendrogram tree, if we have N objects to classify, the closest two objects and the remaining (N-2)-many closest objects from these two first closest objects can be obtained. As a result, we can write a set wherein the N-many objects are sorted based on their distances from the first two closest objects. After doing so the algorithm combines the k-closest objects into a single class if and only if the coefficient of variation on the major and minor axis length of the new class is still less than or equal to the imposed threshold on the coefficient of variation (0.15). In the next step, we will perform the above-mentioned algorithm iteratively on the remaining classes until the number of classes reaches a plateau. It should be mentioned that in the second loop and so on, the dendrogram tree is formed from the average value of the features in a class and the restriction on the coefficient of variation is always set on the objects within a class.

As a final step we can furthermore classify the classes obtained from the Iterative Hierarchical Clustering c-RSD into unique classes based on the visual inspection of these classes. Any classes that visually resembled each other and that were connected in the

dendrogram tree were furthermore combined together. Calculation of the coefficient of variation on the major/minor axis length after this final classification step might be higher than the 0.15 value because of the supervised step but visually they appear to belong to the same class.

Supplementary Figures for Chapter 3

A

B

C

Clusters with <500
localizations

D

Z-score/height

Number of classes

E

Class 4

Class 5

Class 12

Class 15

Class 23

Class 27

1µm

F

Z-score/height
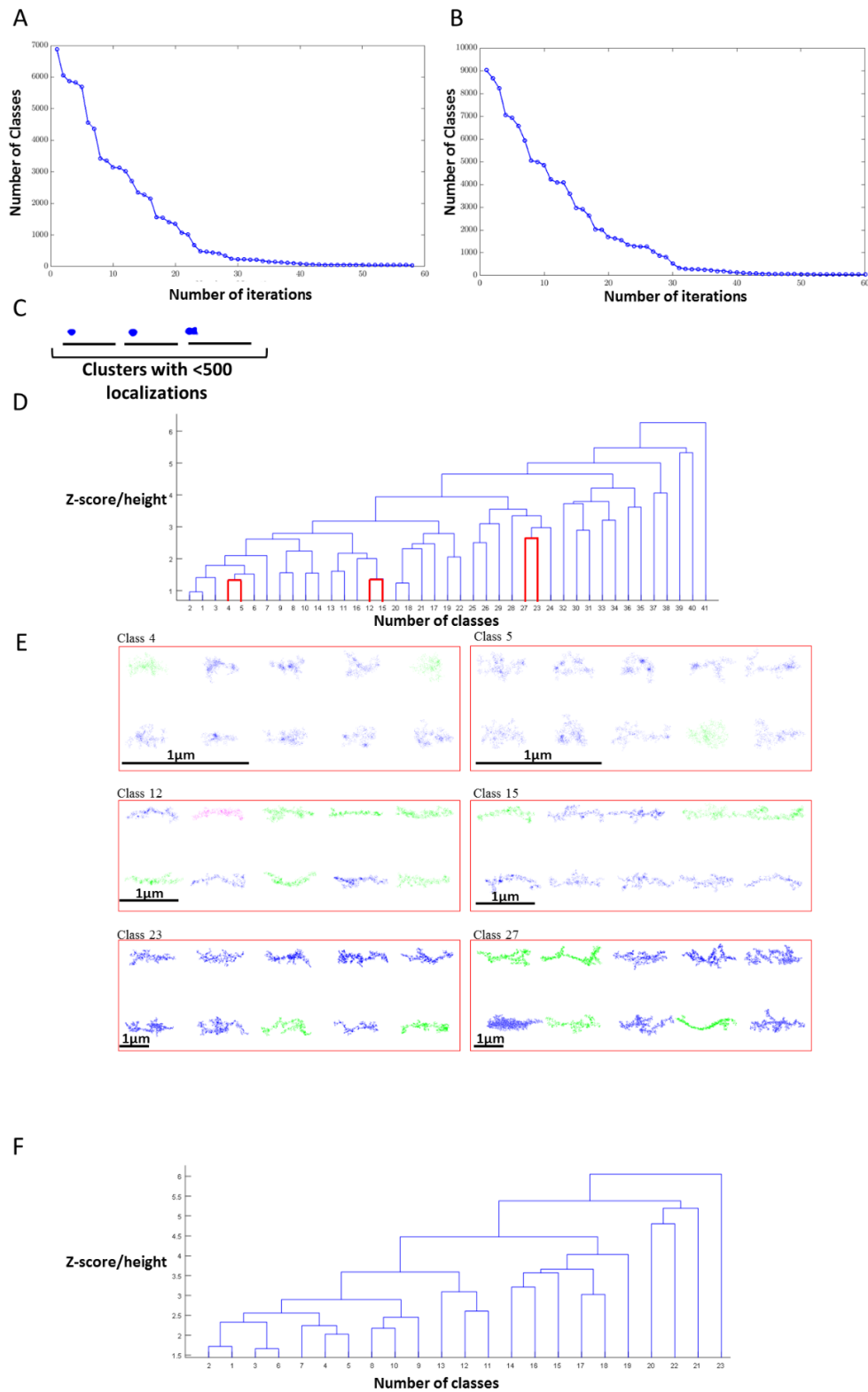
Number of classes

Fig. B1: Iterative hierarchical shape classification. A. Plots showing the number of classes identified after each iteration of the hierarchical clustering algorithm in low and high tau aggregation cells of the Clone 4.1 maintained in Dox and expressing 4R-P301L-GFP tau. The number of classes identified converge after about 30 iterations. B. Plots showing the number of classes identified after each iteration of the hierarchical clustering algorithm in GFP-nanobody, Th231 and AT8 labeled Clone 4.1 (4R-P301L-GFP tau) cells. The number of classes identified converge after about 30 iterations. C. Examples of clusters having <500 localizations in Clone 4.1 cells maintained in Dox and expressing 4R-P301L-GFP tau. These structures mostly represent nano-clusters with no particular shape. Scale bars are 500nm. D. Dendrogram tree resulting from unsupervised classification showing 41 classes of tau aggregates in Clone 4.1 maintained in Dox and expressing 4R-P301L-GFP tau and how they relate to each other. This example is derived from the analysis of Thr231, AT8 and GFP nano stained Clone 4.1 cells. Examples of pairs of classes that were visually similar and later manually combined into the same class are shown in red boxes. The x axis represents the number of classes, whereas the y axis represents the z-score/height. E. Examples of super-resolution images of pairs of classes that were visually similar and later manually combined into the same class are shown. Shapes from Thr231 stained Clone 4.1 cells are colored magenta, those from AT8 stained Clone 4.1 cells are colored green and those from the GFP nanobody stained Clone 4.1 cells are colored blue. F. Dendrogram tree after manually combining the 41 classes resulting from the unsupervised classification into 23 classes of tau aggregates in Clone 4.1 maintained in Dox and expressing 4R-P301L-GFP tau and how they relate to each other. This example is derived

from the analysis of Thr231, AT8 and GFP nano stained Clone 4.1 cells. The x axis represents the number of classes, whereas the y axis represents the z-score/height.
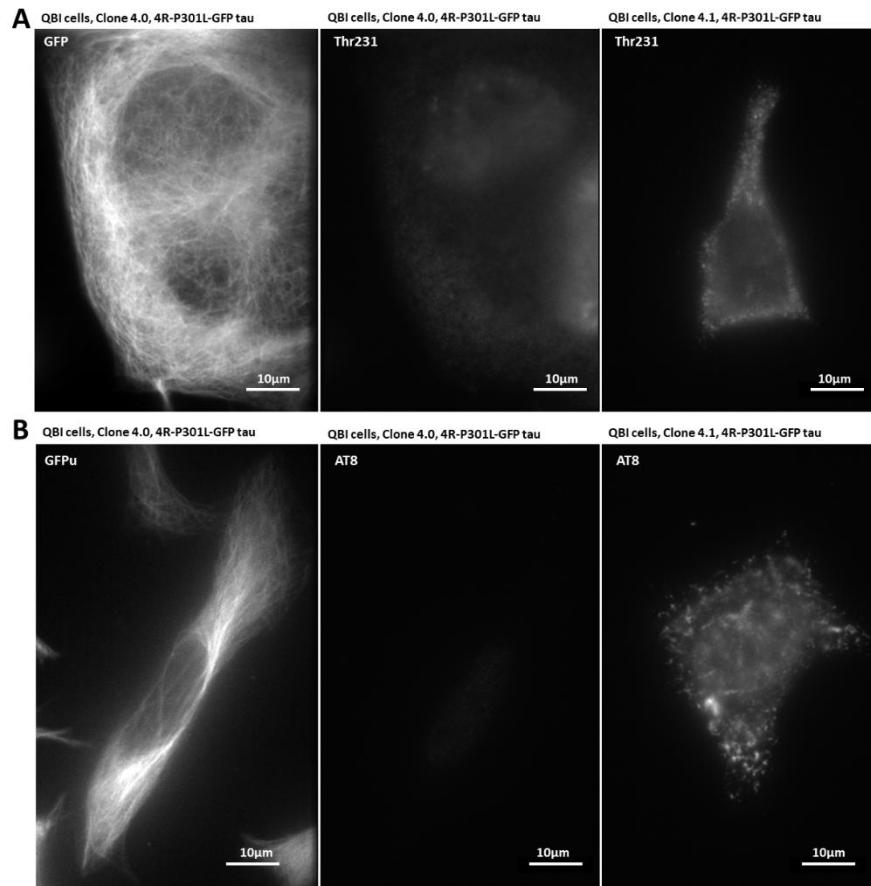
Fig. B2: Thr231 and AT8 antibodies specifically stain tau in Clone 4.1 but not Clone 4.0. A. Wide-field images of GFP fluorescence in Clone 4.0 cells expressing 4R-P301L-GFP tau after overnight Dox induction of tau expression (left panel) and fluorescence signal from Thr231 antibody staining (Thr231, middle panel) in the same cell. Fluorescence signal from Thr231 antibody staining in a Clone 4.1 maintained in Dox and expressing 4R-P301L-GFP tau (Thr231, right panel). B. Wide-field images of GFP fluorescence in Clone 4.0 cells expressing 4R-P301L-GFP tau after overnight Dox induction of tau expression (left panel) and fluorescence signal from AT8 antibody staining (AT8, middle panel) in the

same cell. Fluorescence signal from AT8 antibody staining in a Clone 4.1 maintained in Dox and expressing 4R-P301L-GFP tau (AT8, right panel).
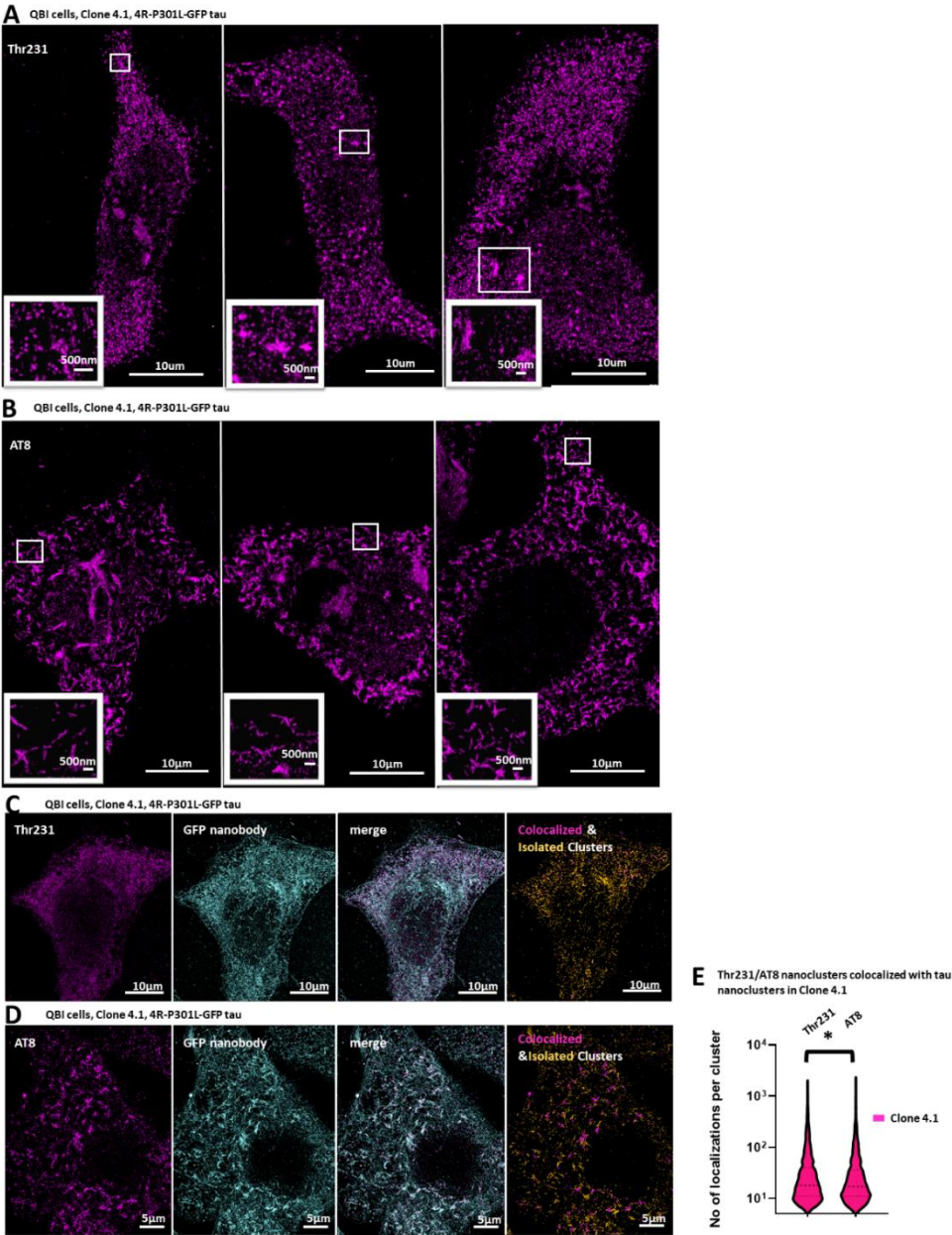
Fig. B3: Phosphorylation of specific tau residues is associated with a diverse range of tau aggregates. A. Super-resolution images of tau hyperphosphorylated at residue Thr231 in Clone 4.1 cells maintained in Dox and expressing 4R-P301L-GFP tau, stained with Thr231 antibody. B. Super-resolution images of tau hyperphosphorylated at residuea Ser202/Thr205 in Clone 4.1 cells maintained in Dox and expressing 4R-P301L-GFP tau, stained with AT8 antibody. C. Two-color super-resolution images of Thr231 (magenta), total tau (cyan) and overlay in Clone 4.1 cells maintained in Dox and expressing 4R-P301L-GFP tau. The results of the co-localization analysis are shown in which tau co-localized with Thr231 is shown in magenta and isolated tau is shown in yellow. D. Two-color super-resolution images of AT8 (magenta), total tau (cyan) and overlay in Clone 4.1 cells maintained in Dox and expressing 4R-P301L-GFP tau. The results of the co-localization analysis are shown in which tau co-localized with AT8 is shown in magenta and isolated tau is shown in yellow. E. Violin plots showing the number of localizations per segmented Voronoi object of tau that colocalizes with Thr231 or AT8 in Clone 4.1 cells maintained in Dox and expressing 4R-P301L-GFP tau. The dashed lines indicate the median and the dotted lines indicate the 25th and 75th percentile (Thr231: n=6 cells, n=2 experiments, AT8: n=5 cells, n=2 experiments). *, $p<0.05$.

Supplementary Tables for Chapter 3

Condition	Number of clusters (before classification)	Number of classes (after unsupervised classification)	Number of classes (after manually combining classes)
Low tau aggregation	1343	N/A	N/A
High tau aggregation	5539	N/A	N/A
Total	6882	40	22
Thr231 staining	225	N/A	N/A
AT8 staining	1913	N/A	N/A
GFP nano staining	6882	N/A	N/A
Total	9020	41	23

Table S.3.1. Number of tau aggregates and classes identified using Iterative Hierarchical Clustering c-RSD

Class	Number of clusters per class	Ratio of low tau aggregation clusters over the total no of low tau aggregation clusters in each class	Ratio of high tau aggregation clusters over the total no of high tau aggregation clusters in each class
1	598	0.01787044	0.10362881
2	827	0.10275503	0.12439068
3	507	0.10052122	0.06716014
4	1311	0.19136262	0.19028706
5	446	0.09828742	0.05668893
6	1066	0.2278481	0.13720888
7	276	0.04095309	0.0398989
8	595	0.10052122	0.08304748
9	281	0.03201787	0.04296804
10	337	0.0476545	0.04928687
11	67	0.00446761	0.01101282
12	302	0.02382725	0.04874526
13	97	0.00521221	0.01624842
14	10	0.0007446	0.00162484
15	76	0.00446761	0.01263766
16	30	0	0.00541614
17	28	0.0014892	0.00469399
18	3	0	0.00054161
19	18	0	0.00324968
20	1	0	0.00018054
21	5	0	0.00090269

| 22 | 1 | 0 | 0.00018054 |

Table S.3.2. Detailed quantitative description of classes from low and high tau aggregation Clone 4.1 cells

Class	Number of clusters per class	Ratio of Thr231 clusters over the total no of Thr231 clusters in each class	Ratio of AT8 clusters over the total no of AT8 clusters in each class	Ratio of GFP nano clusters over the total no of GFP nano clusters in each class
1	1491	0.1822222	0.1217982	0.1768381
2	635	0.0355556	0.0893884	0.0662598
3	2318	0.4266667	0.2122321	0.2638768
4	358	0.0266667	0.0627287	0.0337111
5	98	0.0088889	0.0245687	0.00712
6	1025	0.1288889	0.1003659	0.1168265
7	609	0.0622222	0.0935703	0.0604475
8	132	0.0133333	0.026137	0.0114792
9	738	0.0933333	0.0773654	0.0826795
10	592	0.0177778	0.0794564	0.0633537
11	11	0	0.0010455	0.0013078
12	110	0.0044444	0.0130685	0.0122058
13	668	0	0.0737062	0.0765766
14	44	0	0.0078411	0.0042139
15	95	0	0.0115003	0.0106074
16	12	0	0.0005227	0.0015984
17	37	0	0.0036592	0.0043592
18	11	0	0.0005227	0.0014531
19	11	0	0	0.0015984
20	18	0	0.0005227	0.0024702
21	1	0	0	0.0001453
22	5	0	0	0.0007265

23	1	0	0	0.0001453

Table S.3.3. Detailed quantitative description of classes from Thr231, AT8 and GFP nanobody stained Clone 4.1 cells

Supplementary Materials and Methods for Chapter 4

Cell Culture

A stable human embryonic kidney-derived QBI-293 cell line (Clone 4.1) expressing full length human tau T40 (2N4R) carrying the P301L mutation with a GFP tag, a kind gift from the V. Lee lab at the University of Pennsylvania, was used for the majority of experiments. Clone 4.1 was originally sorted from the parent Clone 4.0 cells to enrich for large compact tau aggregates after exogenous tau fibril addition (J. L. Guo et al. 2016). Cells were grown in Dulbecco's modified Eagle's medium supplemented with 10% tetracycline-screened fetal bovine serum (FBS), 1% pyruvate (10mM), 1% penicillin-streptomycin and L-glutamine (20 mM), 5ug/ml blasticidin, 200ug/ml Zeozin and were maintained in a 37°C incubator containing 5% CO_2. Clone 4.1 was maintained in media containing 100ng/mL of Doxycycline (Dox). For all imaging, cells were plated on eight-well Lab-Tek 1 coverglass chambers (Nunc).

Cell lysate extraction and Western blotting

 Cell lysate was extracted from QBI cells with Dox-regulated expression of 4R-P301L-GFP tau (Clone 4.1 grown in Dox) by RIPA (Radioimmunoprecipitation) buffer containing phosphatase and protease inhibitors and incubated on ice for 15 min. Lysates were then centrifuged at maximum speed on a tabletop centrifuge for 30 min at 4 °C. Protein concentration was determined using the Bradford assay. 2-3ug of protein per sample were resolved in 4-12% Bis-Tris NuPAGE (polyacrylamide) gels, transferred to nitrocellulose membranes, and blocked in Odyssey blocking buffer (Li-Cor Biosciences) before probing

with antibodies (Table S.4.1). The blots were further incubated with IRDye labeled secondary antibodies and scanned using ODY-2816 Imager (Li-Cor Biosciences). GAPDH was used as a loading control. Image analysis was performed using Image Studio Lite software (LI-COR). Fluorescent band intensity was normalized to the GAPDH loading control.

Immunostaining

Cells were first incubated with microtubule stabilizing buffer (MTSB: 15g PIPES, 1.9g EGTA, 1.32 $MgSO_4 \cdot 7H_2O$, 5g KOH, H_2O to a liter, pH=7) for 3 min and then ice cold methanol was added in the buffer for 3 min. Following this short incubation, cells were washed with MTSB twice. Cells were then blocked for 1hr using 4% (wt/vol) BSA in PBS. They were then incubated with the appropriate dilution of GFP nanobody in 4% (wt/vol) BSA in PBS. A list of antibodies/nanobodies used in this study is provided in Table S.4.1. The nanobody we used was GFP VHH, recombinant binding protein (gt-250, Chromotek).

SMLM imaging

SMLM was acquired using an Oxford Nanoimaging system. To avoid bias, images were randomly acquired and all acquired images were included in the analysis unless there was substantial drift present in the images, which could not be corrected by post-processing. The Nanoimager-S microscope had the following configuration: 405-, 488-, 561- and 640-nm lasers, 498-551- and 576-620-nm band-pass filters in channel 1, and 666-705-nm band-pass filters in channel 2, 100 x 1.4 NA oil immersion objective (Olympus), and a Hamamatsu Flash 4 V3 sCMOS camera. Localization microscopy images were acquired with 15 ms exposure for 50,000 frames. For multi-color SMLM, 110,000 frames with 15

ms exposure were acquired with sequential laser activation. The images were then processed using the NimOS localization software (Oxford Nanoimaging).

Data analysis

Voronoi Tesselation Analysis

Localizations were exported in .csv format using the NimOS localization software and converted to .bin files using MATLAB R2017a. The rendered SMLM images were either cropped using the AFIB plugin in ImageJ (National Institutes of Health) or used as a whole (Schindelin et al. 2012). Voronoi Tesselation Analysis was performed in MATLAB R2017a similarly to (Otterstrom et al. 2019)(Levet et al. 2015)(Andronov et al. 2016). First, a Voronoi threshold was chosen manually to define a Voronoi cluster as a collection of Voronoi polygons with areas smaller than the given threshold. We confirmed that the selected threshold led to proper segmentation of the super-resolution images visually. We adjusted the threshold to achieve proper segmentation and avoid errors in cells that were much or less dense than the majority. The x and y coordinates from the localizations were processed by the "delaunayTriangulation" function and then the 'Voronoidiagram" function to generate Voronoi polygons. The Voronoi polygon areas were calculated from the shoelace algorithm. A new molecule list assigning localizations to different channels (0-9) according to their Voronoi area was then generated. Next, these localizations were put into different clusters and their cluster statistics were generated and used for analysis. The different clusters were pseudocolored based on their channel (0-9) and visualized using a custom-written software, Insight3 (provided by B. Huang, University of California, San Francisco, San Francisco, CA; (Huang et al. 2008).

Principal Component Analysis

Principal Component Analysis (PCA) (F.R.S. 2010) is a data-dimensionality reduction technique that summarizes the original data with new variables (called principal components, or PCs), which trade a little accuracy for simplicity, and are constructed by using a set of linear combinations of the original data variables. PCA maximizes the explained variance of the data by finding the eigenvectors with the largest eigenvalues of the covariance matrix. Moreover, each PC is orthogonal (i.e., uncorrelated) with any other PC, and the first PC captures the most variance in the data, the second PC the second most, etc. Using this approach, we were able to simplify the original data, as the later PCs explained very little variance of the data (in most cases mainly noise), and were therefore removed from the model. This newly constructed PCA model was used for exploration, visualization and data analysis.

Machine Learning – Based Classification

To assess tau aggregate degradation, a supervised classification method called random forest was used (Breiman 2001). Initially, a small subset of the data was manually classified into four different groups (linear fibrils, branched fibrils, NFT Precursors, and NFTs), which was used as the ground truth for the classifier. This random forest classifier is an ensemble technique that uses a large number of so-called 'weak' classifiers (i.e., decision trees) that each classify the data (i.e., the shape descriptors describing the tau aggregates) independently and then combine these results using the 'power of numbers' principle: each tree predicts the class for each sample and the class with the most votes is then the random forest prediction. The strength of the random forest classifier can be explained by the fact that the large number of trees protect each other from their individual

errors. However, the caveat here is that the different trees have to be (largely) uncorrelated to each other, but, this can easily be obtained if each of the individual trees predict the outcome for just a small, randomly selected, subset of variables of the training data. Once the random forest classifier is trained, the model can be used on new data to predict the type of tau aggregate.

Statistical Analysis

Non-parametric Mann-Whitney tests were performed using OriginPro 2017 software for the imaging data sets in Fig. 4.1B.

Supplementary Figures for Chapter 4
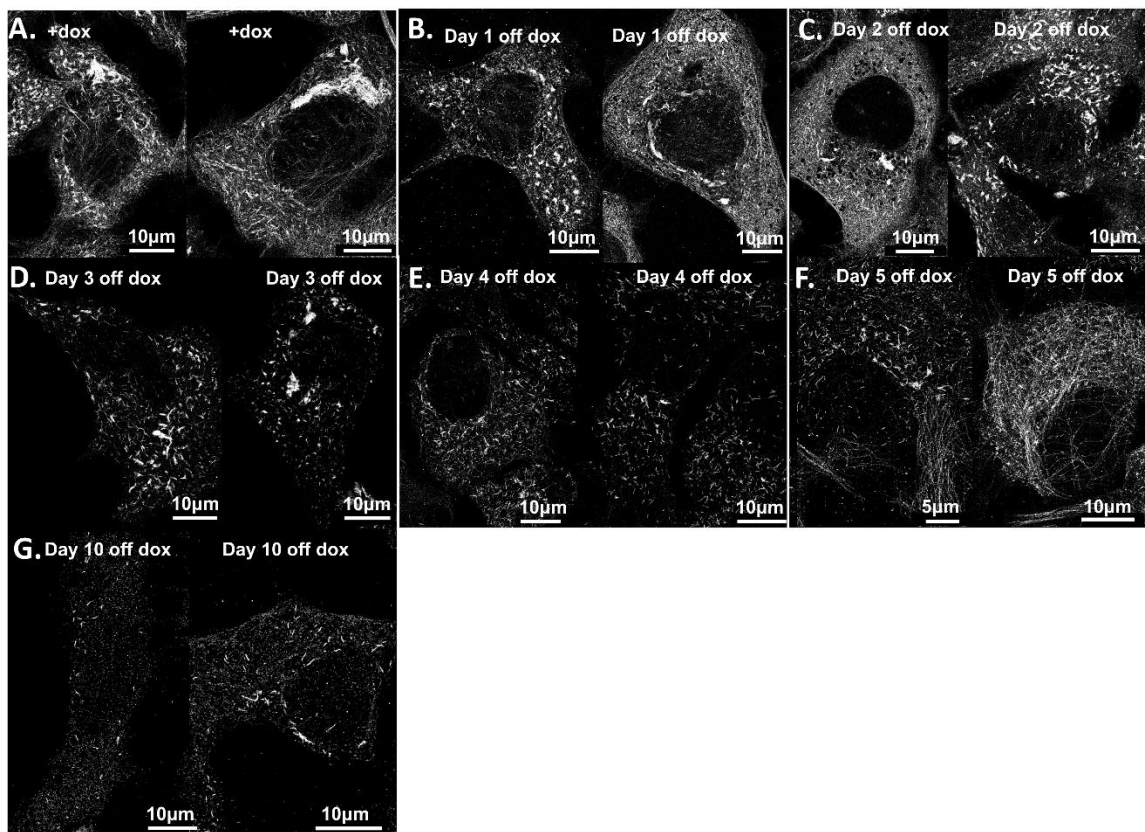
Fig. C1: Representative images of tau from +dox control and the 1-10 days off dox experiments. A. Super-resolution images of tau in Clone 4.1 cells maintained in dox media, stained with a GFP nanobody conjugated to AlexaFluor 647. B-G. Super-resolution images of tau in Clone 4.1 cells where dox has been removed for 1 day (B), 2 days (C), 3 days (D), 4 days (E), 5 days (F), 10 days (G).
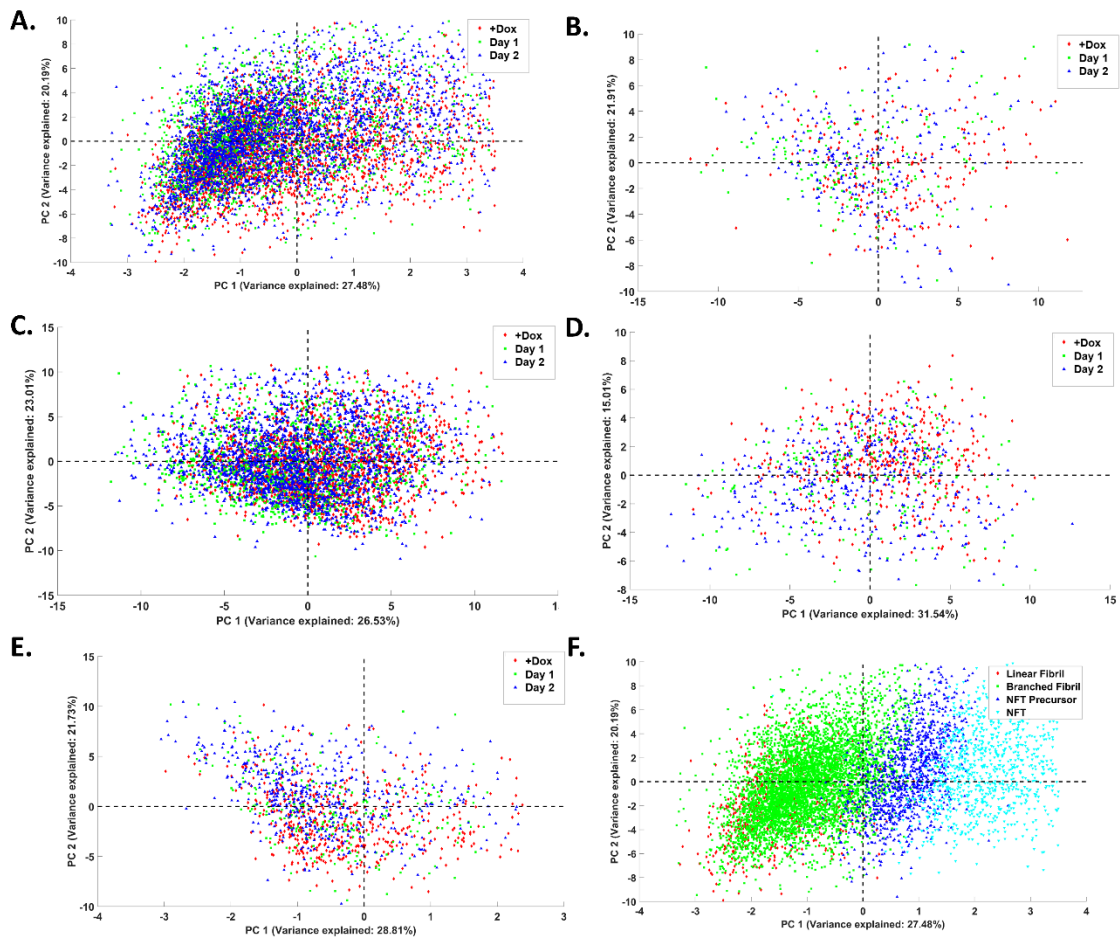
Fig. C2: PCA reveals similarities in tau aggregate structures from +dox control, Day 1 and Day 2 off dox. A. PCA plot for tau aggregates from cells from +dox control (red), Day 1 (green), Day 2 (blue). B. PCA plot of all the linear fibrils from cells from +dox control (red), Day 1 (green), Day 2 (blue). C. PCA plot of all the branched fibrils from cells from +dox control (red), Day 1 (green), Day 2 (blue). D. PCA plot of all the NFT Precursors from cells from +dox control (red), Day 1 (green),

Day 2 (blue). E. PCA plot of all the NFTs from cells from +dox control (red), Day 1 (green), Day 2 (blue). F. PCA plot of the linear fibrils (red), branched fibrils (green), NFT Precursors (blue) NFTs (cyan) from cells from +dox control, Day 1 and Day 2 off dox.
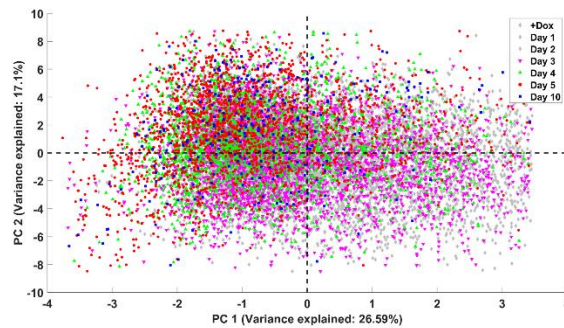
Fig. C3: PCA reveals differences in tau aggregate structures from different days off dox. PCA plot for tau aggregates from cells from +dox control (grey), Day 1 (grey), Day 2 (grey), Day 3 (magenta), Day 4 (green), Day 5 (red) and Day 10 off dox (blue).
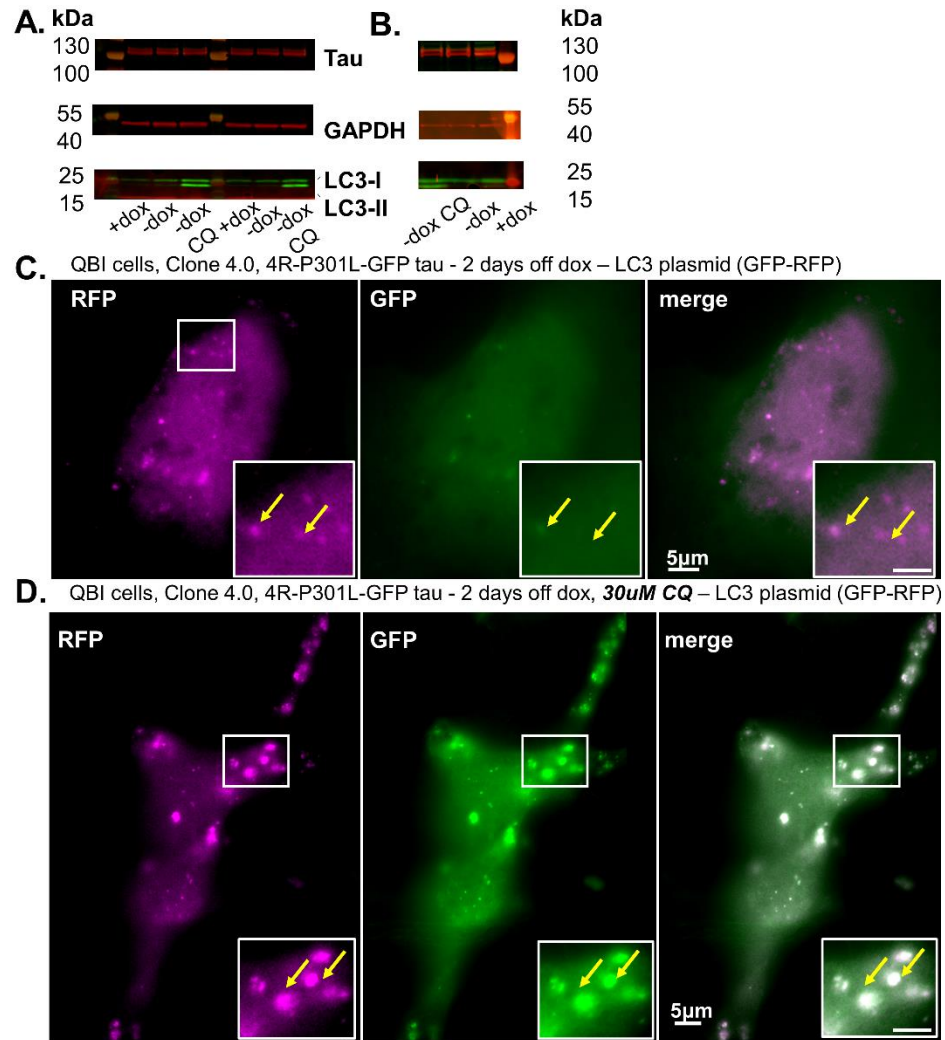
Fig. C4: Treatment with CQ leads to autophagy inhibition. A. Western Blot showing tau, GAPDH (loading control) and LC3-I and II from lysates of Clone 4.1 cells cultured in the presence of Dox (+dox), or the absence of Dox for 1 day in culture (-dox) or the absence of Dox for 1 day in culture and in the presence of 30 μM CQ (-dox CQ). B. Western Blot showing tau, GAPDH (loading control) and LC3-I and II from lysates of Clone 4.1 cells cultured in the presence of Dox (+dox), or the absence of Dox for 2 days in culture (-dox) or the absence of Dox for 2 days in culture and in the presence of 30 μM CQ (-dox CQ). Clone 4.0 cells transfected with an LC3-plasmid (GFP-RFP) that have been in media without dox for two days (C) or two days in addition to being treated with 30 μM CQ (D). Scale bar of inset is 5 μm.

115
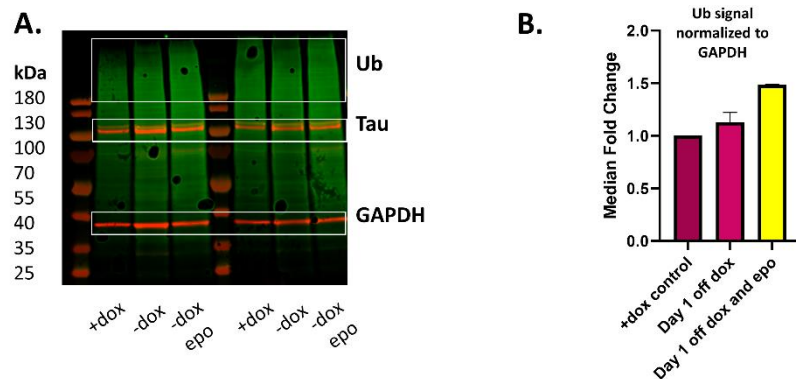
Fig. C5: Treatment with epo leads to proteasome inhibition. A. Western Blot showing tau, Ub (green), Tau, and GAPDH (loading control from lysates of Clone 4.1 cells cultured in the presence of Dox (+dox), or the absence of Dox for 1 day in culture (-dox) or the absence of Dox for 1 day in culture and in the presence of 20 nM CQ (-dox epo). B. Quantification of signal from two Western blot replicates in A. Error bars indicate standard deviation (SD).
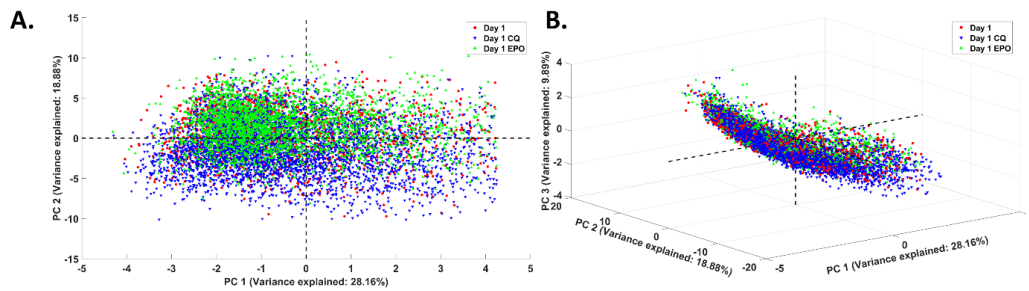
Fig. C6: PCA reveals differences in tau aggregate structures from CQ treatment versus epo treatment. A, B. 2-D and 3-D PCA plot of tau aggregates from cells from Day 1(red), Day 1 CQ (blue), Day 1 epo (green).

Antibody	Host species	Catalog number	Vendor
α-tubulin	Rabbit	ab18251	Abcam
Ubiquitin	Rabbit	E4I2J	Cell Signaling Technology
LC3	Rabbit	ab48394	Abcam
GFP Binding Protein	Alpaca	gt-250	ChromoTek
Tau-5	Mouse	AHB0042	ThermoFisher Scientific
GAPDH	Mouse	A01622-40	GenScript

Table S.4.1. Antibodies used in this study

BIBLIOGRAPHY

Agostini, Federica, Carlos G. Dotti, Azucena Pérez-Cañamás, Maria Dolores Ledesma, Federico Benetti, and Giuseppe Legname. 2013. "Prion Protein Accumulation in Lipid Rafts of Mouse Aging Brain." *PLOS ONE* 8 (9): e74244. https://doi.org/10.1371/JOURNAL.PONE.0074244.

Akoury, Elias, Marcus Pickhardt, Michal Gajda, Jacek Biernat, Eckhard Mandelkow, and Markus Zweckstetter. 2013. "Mechanistic Basis of Phenothiazine-Driven Inhibition of Tau Aggregation." *Angewandte Chemie (International Ed. in English)* 52 (12): 3511–15. https://doi.org/10.1002/ANIE.201208290.

Alonso, Alejandra Del C., Tanweer Zaidi, Inge Grundke-Iqbal, and Khalid Iqbal. 1994. "Role of Abnormally Phosphorylated Tau in the Breakdown of Microtubules in Alzheimer Disease." *Proceedings of the National Academy of Sciences of the United States of America* 91 (12): 5562. https://doi.org/10.1073/PNAS.91.12.5562.

Alquezar, Carolina, Shruti Arya, and Aimee W. Kao. 2021. "Tau Post-Translational Modifications: Dynamic Transformers of Tau Function, Degradation, and Aggregation." *Frontiers in Neurology*. Frontiers Media S.A. https://doi.org/10.3389/fneur.2020.595532.

Andronov, Leonid, Igor Orlov, Yves Lutz, Jean Luc Vonesch, and Bruno P. Klaholz. 2016. "ClusterViSu, a Method for Clustering of Protein Complexes by Voronoi Tessellation in Super-Resolution Microscopy." *Scientific Reports* 6 (1): 1–9. https://doi.org/10.1038/srep24084.

Arai, Tetsuaki, Kenji Ikeda, Haruhiko Akiyama, Takashi Nonaka, Masato Hasegawa, Koichi Ishiguro, Shuji Iritani, et al. 2004. "Identification of Amino-Terminally Cleaved Tau Fragments That Distinguish Progressive Supranuclear Palsy from Corticobasal Degeneration." *Annals of Neurology* 55 (1): 72–79. https://doi.org/10.1002/ANA.10793.

Arakhamia, Tamta, Christina E. Lee, Yari Carlomagno, Duc M. Duong, Sean R. Kundinger, Kevin Wang, Dewight Williams, et al. 2020. "Posttranslational Modifications Mediate the Structural Diversity of Tauopathy Strains." *Cell* 180 (4): 633-644.e12. https://doi.org/10.1016/j.cell.2020.01.027.

Arkin, Michelle M.R., and James A. Wells. 2004. "Small-Molecule Inhibitors of Protein–Protein Interactions: Progressing towards the Dream." *Nature Reviews Drug Discovery 2004 3:4* 3 (4): 301–17. https://doi.org/10.1038/nrd1343.

Baba, Atsushi, Koshiro Akagi, Mai Takayanagi, John G. Flanagan, Toshihide Kobayashi, and Mitsuharu Hattori. 2009. "Fyn Tyrosine Kinase Regulates the Surface Expression of Glycosylphosphatidylinositol-Linked Ephrin via the Modulation of Sphingomyelin Metabolism." *The Journal of Biological Chemistry* 284 (14): 9206. https://doi.org/10.1074/JBC.M809401200.

Babu, Jeganathan Ramesh, Thangiah Geetha, and Marie W. Wooten. 2005. "Sequestosome 1/P62 Shuttles Polyubiquitinated Tau for Proteasomal

Degradation." *Journal of Neurochemistry* 94 (1): 192–203. https://doi.org/10.1111/J.1471-4159.2005.03181.X.

Bancher, C., C. Brunner, H. Lassmann, H. Budka, K. Jellinger, G. Wiche, F. Seitelberger, I. Grundke-Iqbal, K. Iqbal, and H. M. Wisniewski. 1989. "Accumulation of Abnormally Phosphorylated Tau Precedes the Formation of Neurofibrillary Tangles in Alzheimer's Disease." *Brain Research* 477 (1–2): 90–99. https://doi.org/10.1016/0006-8993(89)91396-6.

Barrantes, Alejandro, Javier Sotres, Mercedes Hernando-Pérez, Maria J. Benítez, Pedro J. De Pablo, Arturo M. Baró, Jesus Ávila, and Juan S. Jiménez. 2009. "Tau Aggregation Followed by Atomic Force Microscopy and Surface Plasmon Resonance, and Single Molecule Tau-Tau Interaction Probed by Atomic Force Spectroscopy." *Journal of Alzheimer's Disease : JAD* 18 (1): 141–51. https://doi.org/10.3233/JAD-2009-1130.

Bates, Mark, Bo Huang, Graham T. Dempsey, and Xiaowei Zhuang. 2007. "Multicolor Super-Resolution Imaging with Photo-Switchable Fluorescent Probes." *Science* 317 (5845): 1749–53. https://doi.org/10.1126/science.1146598.

Battisti, Anna, Gabriele Ciasca, Alessandro Grottesi, Antonio Bianconi, and Alexander Tenenbaum. 2012. "Temporary Secondary Structures in Tau, an Intrinsically Disordered Protein." *Http://Dx.Doi.Org/10.1080/08927022.2011.633347* 38 (7): 525–33. https://doi.org/10.1080/08927022.2011.633347.

Bence, N. F., R. M. Sampat, and R. R. Kopito. 2001. "Impairment of the Ubiquitin-Proteasome System by Protein Aggregation." *Science (New York, N.Y.)* 292 (5521): 1552–55. https://doi.org/10.1126/SCIENCE.292.5521.1552.

Berger, Zdenek, Hanno Roder, Amanda Hanna, Aaron Carlson, Vijayaraghavan Rangachari, Mei Yue, Zbigniew Wszolek, et al. 2007. "Accumulation of Pathological Tau Species and Memory Loss in a Conditional Model of Tauopathy." *Journal of Neuroscience* 27 (14): 3650–62. https://doi.org/10.1523/JNEUROSCI.0587-07.2007.

Betzig, Eric, George H. Patterson, Rachid Sougrat, O. Wolf Lindwasser, Scott Olenych, Juan S. Bonifacino, Michael W. Davidson, Jennifer Lippincott-Schwartz, and Harald F. Hess. 2006. "Imaging Intracellular Fluorescent Proteins at Nanometer Resolution." *Science* 313 (5793): 1642–45. https://doi.org/10.1126/SCIENCE.1127344/SUPPL_FILE/BETZIG.SOM.PDF.

Bi, Xiaoning, Tasir S. Haque, Jun Zhou, A. Geoffrey Skillman, Bin Lin, Christine E. Lee, Irwin D. Kuntz, Jonathan A. Ellman, and Gary Lynch. 2000. "Novel Cathepsin D Inhibitors Block the Formation of Hyperphosphorylated Tau Fragments in Hippocampus." *Journal of Neurochemistry* 74 (4): 1469–77. https://doi.org/10.1046/J.1471-4159.2000.0741469.X.

Bochtler, Matthias, Lars Ditzel, Michael Groll, Claudia Hartmann, and Robert Huber. 1999. "The Proteasome." *Annual Review of Biophysics and Biomolecular Structure* 28: 295–317. https://doi.org/10.1146/ANNUREV.BIOPHYS.28.1.295.

Bohrer, Christopher Herrick, Xinxing Yang, Xiaoli Weng, Brian Tenner, Brian Ross, Ryan Mcquillen, Jin Zhang, Elijah Roberts, and Jie Xiao. 2019. "A Pairwise Distance Distribution Correction (DDC) Algorithm for Blinking-Free Super-Resolution Microscopy." *BioRxiv*, January, 768051. https://doi.org/10.1101/768051.

Bok, Eugene, Eunju Leem, Bo Ram Lee, Ji Min Lee, Chang Jae Yoo, Eun Mi Lee, and Jaekwang Kim. 2021. "Role of the Lipid Membrane and Membrane Proteins in Tau Pathology." *Frontiers in Cell and Developmental Biology* 9 (April). https://doi.org/10.3389/FCELL.2021.653815.

Boland, Barry, Asok Kumar, Sooyeon Lee, Frances M. Platt, Jerzy Wegiel, W. Haung Yu, and Ralph A. Nixon. 2008. "Autophagy Induction and Autophagosome Clearance in Neurons: Relationship to Autophagic Pathology in Alzheimer's Disease." *The Journal of Neuroscience : The Official Journal of the Society for Neuroscience* 28 (27): 6926–37. https://doi.org/10.1523/JNEUROSCI.0800-08.2008.

Borghgraef, Peter, Clément Menuet, Clara Theunis, Justin V. Louis, Herman Devijver, Hervé Maurin, Caroline Smet-Nocca, et al. 2013. "Increasing Brain Protein O-GlcNAc-Ylation Mitigates Breathing Defects and Mortality of Tau.P301L Mice." *PloS One* 8 (12). https://doi.org/10.1371/JOURNAL.PONE.0084442.

Braak, H., and E. Braak. 1991. "Neuropathological Stageing of Alzheimer-Related Changes." *Acta Neuropathologica* 82 (4): 239–59. https://doi.org/10.1007/BF00308809.

Braak, Heiko, Irina Alafuzoff, Thomas Arzberger, Hans Kretzschmar, and Kelly Tredici. 2006. "Staging of Alzheimer Disease-Associated Neurofibrillary Pathology Using Paraffin Sections and Immunocytochemistry." *Acta Neuropathologica* 112 (4): 389–404. https://doi.org/10.1007/S00401-006-0127-Z.

Brandt, Roland, Jocelyne Léger, and Gloria Lee. 1995. "Interaction of Tau with the Neural Plasma Membrane Mediated by Tau's Amino-Terminal Projection Domain." *The Journal of Cell Biology* 131 (5): 1327–40. https://doi.org/10.1083/JCB.131.5.1327.

Breiman, Leo. 2001. "Random Forests." *Machine Learning 2001 45:1* 45 (1): 5–32. https://doi.org/10.1023/A:1010933404324.

Brunden, Kurt R., Yuemang Yao, Justin S. Potuzak, Nuria Ibarz Ferrer, Carlo Ballatore, Michael J. James, Anne Marie L. Hogan, John Q. Trojanowski, Amos B. Smith, and Virginia M.Y. Lee. 2011. "The Characterization of Microtubule-Stabilizing Drugs as Possible Therapeutic Agents for Alzheimer's Disease and Related Tauopathies." *Pharmacological Research* 63 (4): 341–51. https://doi.org/10.1016/J.PHRS.2010.12.002.

Brunden, Kurt R., Bin Zhang, Jenna Carroll, Yuemang Yao, Justin S. Potuzak, Anne Marie L. Hogan, Michiyo Iba, et al. 2010. "Epothilone D Improves Microtubule Density, Axonal Integrity, and Cognition in a Transgenic Mouse Model of Tauopathy." *The Journal of Neuroscience : The Official Journal of the Society for*

Neuroscience 30 (41): 13861–66. https://doi.org/10.1523/JNEUROSCI.3059-10.2010.

Cario, Alisa, Adriana Savastano, Neil B. Wood, Zhu Liu, Michael J. Previs, Adam G. Hendricks, Markus Zweckstetter, and Christopher L. Berger. 2022. "The Pathogenic R5L Mutation Disrupts Formation of Tau Complexes on the Microtubule by Altering Local N-Terminal Structure." *Proceedings of the National Academy of Sciences of the United States of America* 119 (7). https://doi.org/10.1073/PNAS.2114215119.

Cash, Adam D., Gjumrakch Aliev, Sandra L. Siedlak, Akihiko Nunomura, Hisashi Fujioka, Xiongwei Zhu, Arun K. Raina, et al. 2003. "Microtubule Reduction in Alzheimer's Disease and Aging Is Independent of Tau Filament Formation." *The American Journal of Pathology* 162 (5): 1623–27. https://doi.org/10.1016/S0002-9440(10)64296-4.

Castillo-Carranza, Diana L., Urmi Sengupta, Marcos J. Guerrero-Muñoz, Cristian A. Lasagna-Reeves, Julia E. Gerson, Gurpreet Singh, D. Mark Estes, et al. 2014. "Passive Immunization with Tau Oligomer Monoclonal Antibody Reverses Tauopathy Phenotypes without Affecting Hyperphosphorylated Neurofibrillary Tangles." *Journal of Neuroscience* 34 (12): 4260–72. https://doi.org/10.1523/JNEUROSCI.3192-13.2014.

Cella Zanacchi, Francesca, Carlo Manzo, Angel S. Alvarez, Nathan D. Derr, Maria F. Garcia-Parajo, and Melike Lakadamyali. 2017. "ADNAorigami Platform for Quantifying Protein Copy Number in Super-Resolution." *Nature Methods* 14 (8): 789–92. https://doi.org/10.1038/nmeth.4342.

Chen, J., Y. Kanai, N. J. Cowan, and N. Hirokawa. 1992. "Projection Domains of MAP2 and Tau Determine Spacings between Microtubules in Dendrites and Axons." *Nature 1992 360:6405* 360 (6405): 674–77. https://doi.org/10.1038/360674a0.

Cheng, Ji, Brian J. North, Tao Zhang, Xiangpeng Dai, Kaixiong Tao, Jianping Guo, and Wenyi Wei. 2018. "The Emerging Roles of Protein Homeostasis-Governing Pathways in Alzheimer's Disease." *Aging Cell* 17 (5). https://doi.org/10.1111/ACEL.12801.

Cherry, Jonathan D., Camille D. Esnault, Zachary H. Baucom, Yorghos Tripodis, Bertrand R. Huber, Victor E. Alvarez, Thor D. Stein, Dennis W. Dickson, and Ann C. McKee. 2021. "Tau Isoforms Are Differentially Expressed across the Hippocampus in Chronic Traumatic Encephalopathy and Alzheimer's Disease." *Acta Neuropathologica Communications* 9 (1): 1–17. https://doi.org/10.1186/S40478-021-01189-4/FIGURES/11.

Cho, Jae-Hyeon, and Gail V. W. Johnson. 2003. "Primed Phosphorylation of Tau at Thr231 by Glycogen Synthase Kinase 3β (GSK3β) Plays a Critical Role in Regulating Tau's Ability to Bind and Stabilize Microtubules." *Journal of Neurochemistry* 88 (2): 349–58. https://doi.org/10.1111/j.1471-4159.2004.02155.x.

Clavaguera, Florence, Hiroyasu Akatsu, Graham Fraser, R. Anthony Crowther, Stephan Frank, Jürgen Hench, Alphonse Probst, et al. 2013. "Brain Homogenates from

Human Tauopathies Induce Tau Inclusions in Mouse Brain." *Proceedings of the National Academy of Sciences of the United States of America* 110 (23): 9535–40. https://doi.org/10.1073/pnas.1301175110.

Congdon, Erin E., Jessica W. Wu, Natura Myeku, Yvette H. Figueroa, Mathieu Herman, Paul S. Marinec, Jason E. Gestwicki, Chad A. Dickey, W. Haung Yu, and Karen E. Duff. 2012. "Methylthioninium Chloride (Methylene Blue) Induces Autophagy and Attenuates Tauopathy in Vitro and in Vivo." *Autophagy* 8 (4): 609–22. https://doi.org/10.4161/AUTO.19048.

Corre, Sylvie Le, Hans W. Klafki, Nikolaus Plesnila, Gabriele Hübinger, Axel Obermeier, Heidi Sahagún, Barbara Monse, et al. 2006. "An Inhibitor of Tau Hyperphosphorylation Prevents Severe Motor Impairments in Tau Transgenic Mice." *Proceedings of the National Academy of Sciences of the United States of America* 103 (25): 9673–78. https://doi.org/10.1073/PNAS.0602913103.

Cowan, Catherine M., Torsten Bossing, Anton Page, David Shepherd, and Amritpal Mudher. 2010. "Soluble Hyper-Phosphorylated Tau Causes Microtubule Breakdown and Functionally Compromises Normal Tau in Vivo." *Acta Neuropathologica* 120 (5): 593–604. https://doi.org/10.1007/s00401-010-0716-8.

Crowe, Alex, Carlo Ballatore, Edward Hyde, John Q. Trojanowski, and Virginia M.Y. Lee. 2007. "High Throughput Screening for Small Molecule Inhibitors of Heparin-Induced Tau Fibril Formation." *Biochemical and Biophysical Research Communications* 358 (1): 1–6. https://doi.org/10.1016/J.BBRC.2007.03.056.

Csordás, György, David Weaver, and György Hajnóczky. 2018. "Endoplasmic Reticulum-Mitochondrial Contactology: Structure and Signaling Functions." *Trends in Cell Biology* 28 (7): 523–40. https://doi.org/10.1016/J.TCB.2018.02.009.

David, Della C., Robert Layfield, Louise Serpell, Yolanda Narain, Michel Goedert, and Maria Grazia Spillantini. 2002. "Proteasomal Degradation of Tau Protein." *Journal of Neurochemistry* 83 (1): 176–85. https://doi.org/10.1046/J.1471-4159.2002.01137.X.

Dawson, Hana N., Adriana Ferreira, Michele V. Eyster, Nupur Ghoshal, Lester I. Binder, and Michael P. Vitek. 2001. "Inhibition of Neuronal Maturation in Primary Hippocampal Neurons from Tau Deficient Mice." *Journal of Cell Science* 114 (Pt 6): 1179–87. https://doi.org/10.1242/JCS.114.6.1179.

Despres, Clément, Cillian Byrne, Haoling Qi, François Xavier Cantrelle, Isabelle Huvent, Béatrice Chambraud, Etienne Emile Baulieu, et al. 2017. "Identification of the Tau Phosphorylation Pattern That Drives Its Aggregation." *Proceedings of the National Academy of Sciences of the United States of America* 114 (34): 9080–85. https://doi.org/10.1073/PNAS.1708448114/SUPPL_FILE/PNAS.1708448114.SAPP.PDF.

Dixit, Ram, Jennifer L. Ross, Yale E. Goldman, and Erika L.F. Holzbaur. 2008. "Differential Regulation of Dynein and Kinesin Motor Proteins by Tau." *Science* 319 (5866): 1086–89. https://doi.org/10.1126/science.1152993.

Dolan, Philip J., and Gail V.W. Johnson. 2010. "A Caspase Cleaved Form of Tau Is Preferentially Degraded through the Autophagy Pathway." *The Journal of Biological Chemistry* 285 (29): 21978–87. https://doi.org/10.1074/JBC.M110.110940.

Drechsel, D. N., A. A. Hyman, M. H. Cobb, and M. W. Kirschner. 1992. "Modulation of the Dynamic Instability of Tubulin Assembly by the Microtubule-Associated Protein Tau." *Molecular Biology of the Cell* 3 (10): 1141. https://doi.org/10.1091/MBC.3.10.1141.

Drubin, David G., and Marc W. Kirschner. 1986. "Tau Protein Function in Living Cells." *The Journal of Cell Biology* 103 (6 Pt 2): 2739–46. https://doi.org/10.1083/JCB.103.6.2739.

Dujardin, Simon, Séverine Bégard, Raphaëlle Caillierez, Cédrick Lachaud, Lucie Delattre, Sébastien Carrier, Anne Loyens, et al. 2014. "Ectosomes: A New Mechanism for Non-Exosomal Secretion of Tau Protein." *PLoS ONE* 9 (6). https://doi.org/10.1371/JOURNAL.PONE.0100760.

Durisic, Nela, Lara Laparra Cuervo, and Melike Lakadamyali. 2014. "Quantitative Super-Resolution Microscopy: Pitfalls and Strategies for Image Analysis." *Current Opinion in Chemical Biology*. Elsevier Ltd. https://doi.org/10.1016/j.cbpa.2014.04.005.

Ebneth, A., R. Godemann, K. Stamer, S. Illenberger, B. Trinczek, E. M. Mandelkow, and E. Mandelkow. 1998. "Overexpression of Tau Protein Inhibits Kinesin-Dependent Trafficking of Vesicles, Mitochondria, and Endoplasmic Reticulum: Implications for Alzheimer's Disease." *Journal of Cell Biology* 143 (3): 777–94. https://doi.org/10.1083/jcb.143.3.777.

Ehmann, Nadine, Sebastian Van De Linde, Amit Alon, Dmitrij Ljaschenko, Xi Zhen Keung, Thorge Holm, Annika Rings, et al. 2014. "Quantitative Super-Resolution Imaging of Bruchpilot Distinguishes Active Zone States." *Nature Communications* 5 (1): 1–12. https://doi.org/10.1038/ncomms5650.

Ester, Martin, Hans-Peter Kriegel, Jiirg Sander, and Xiaowei Xu. 1996. "A Density-Based Algorithm for Discovering Clusters in Large Spatial Databases with Noise." www.aaai.org.

F.R.S., Karl Pearson. 2010. "LIII. On Lines and Planes of Closest Fit to Systems of Points in Space." *Https://Doi.Org/10.1080/14786440109462720* 2 (11): 559–72. https://doi.org/10.1080/14786440109462720.

Fá, M., D. Puzzo, R. Piacentini, A. Staniszewski, H. Zhang, M. A. Baltrons, D. D. Li Puma, et al. 2016. "Extracellular Tau Oligomers Produce An Immediate Impairment of LTP and Memory." *Scientific Reports* 6 (January). https://doi.org/10.1038/srep19393.

Falcon, Benjamin, Wenjuan Zhang, Alexey G. Murzin, Garib Murshudov, Holly J. Garringer, Ruben Vidal, R. Anthony Crowther, Bernardino Ghetti, Sjors H.W. Scheres, and Michel Goedert. 2018. "Structures of Filaments from Pick's Disease Reveal a Novel Tau Protein Fold." *Nature* 561 (7721): 137–40. https://doi.org/10.1038/s41586-018-0454-y.

Falcon, Benjamin, Jasenko Zivanov, Wenjuan Zhang, Alexey G. Murzin, Holly J. Garringer, Ruben Vidal, R. Anthony Crowther, et al. 2019. "Novel Tau Filament Fold in Chronic Traumatic Encephalopathy Encloses Hydrophobic Molecules." *Nature* 568 (7752): 420–23. https://doi.org/10.1038/s41586-019-1026-5.

Fauquant, Caroline, Virginie Redeker, Isabelle Landrieu, Jean Michel Wieruszeski, Dries Verdegem, Olivier Laprévote, Guy Lippens, Benoît Gigant, and Marcel Knossow. 2011. "Systematic Identification of Tubulin-Interacting Fragments of the Microtubule-Associated Protein Tau Leads to a Highly Efficient Promoter of Microtubule Assembly." *Journal of Biological Chemistry* 286 (38): 33358–68. https://doi.org/10.1074/jbc.M111.223545.

Feinstein, H. Eric, Sarah J. Benbow, Nichole E. LaPointe, Nirav Patel, Srinivasan Ramachandran, Thanh D. Do, Michelle R. Gaylord, et al. 2016. "Oligomerization of the Microtubule-Associated Protein Tau Is Mediated by Its N-Terminal Sequences: Implications for Normal and Pathological Tau Action." *Journal of Neurochemistry* 137 (6): 939–54. https://doi.org/10.1111/jnc.13604.

Feng, Qiong, Yu Luo, Xiang Nan Zhang, Xi Fei Yang, Xiao Yue Hong, Dong Shen Sun, Xia Chun Li, et al. 2020. "MAPT/Tau Accumulation Represses Autophagy Flux by Disrupting IST1-Regulated ESCRT-III Complex Formation: A Vicious Cycle in Alzheimer Neurodegeneration." *Autophagy* 16 (4): 641–58. https://doi.org/10.1080/15548627.2019.1633862.

Ferreira, Adriana, and Eileen H. Bigio. 2011. "Calpain-Mediated Tau Cleavage: A Mechanism Leading to Neurodegeneration Shared by Multiple Tauopathies." *Molecular Medicine (Cambridge, Mass.)* 17 (7–8): 676–85. https://doi.org/10.2119/MOLMED.2010.00220.

Fischer, Itzhak, and Peter W. Baas. 2020. "Resurrecting the Mysteries of Big Tau." *Trends in Neurosciences* 43 (7): 493–504. https://doi.org/10.1016/J.TINS.2020.04.007.

Fish, Kenneth N. 2009. "Total Internal Reflection Fluorescence (TIRF) Microscopy." *Current Protocols in Cytometry / Editorial Board, J. Paul Robinson, Managing Editor ... [et Al.]* 0 12 (SUPPL.50): Unit12.18. https://doi.org/10.1002/0471142956.CY1218S50.

Fitzpatrick, Anthony W.P., Benjamin Falcon, Shaoda He, Alexey G. Murzin, Garib Murshudov, Holly J. Garringer, R. Anthony Crowther, Bernardino Ghetti, Michel Goedert, and Sjors H.W. Scheres. 2017. "Cryo-EM Structures of Tau Filaments from Alzheimer's Disease." *Nature* 547 (7662): 185–90. https://doi.org/10.1038/nature23002.

Flores-Rodríguez, Paola, Miguel A. Ontiveros-Torres, María C. Cárdenas-Aguayo, Juan P. Luna-Arias, Marco A. Meraz-Ríos, Amparo Viramontes-Pintos, Charles R. Harrington, et al. 2015. "The Relationship between Truncation and Phosphorylation at the C-Terminus of Tau Protein in the Paired Helical Filaments of Alzheimer's Disease." *Frontiers in Neuroscience* 9 (FEB). https://doi.org/10.3389/FNINS.2015.00033.

Friedhoff, P., M. Von Bergen, E. M. Mandelkow, P. Davies, and E. Mandelkow. 1998. "A Nucleated Assembly Mechanism of Alzheimer Paired Helical Filaments." *Proceedings of the National Academy of Sciences of the United States of America* 95 (26): 15712–17. https://doi.org/10.1073/pnas.95.26.15712.

Fuster-Matanzo, Almudena, María Llorens-Martín, Jerónimo Jurado-Arjona, Jesús Avila, and Félix Hernández. 2012. "Tau Protein and Adult Hippocampal Neurogenesis." *Frontiers in Neuroscience* 6 (JULY): 1–6. https://doi.org/10.3389/fnins.2012.00104.

Ghetti, Bernardino, Adrian L. Oblak, Bradley F. Boeve, Keith A. Johnson, Bradford C. Dickerson, and Michel Goedert. 2015. "Invited Review: Frontotemporal Dementia Caused by Microtubule-Associated Protein Tau Gene (MAPT) Mutations: A Chameleon for Neuropathology and Neuroimaging." *Neuropathology and Applied Neurobiology* 41 (1): 24. https://doi.org/10.1111/NAN.12213.

Goedert, M., M. G. Spillantini, and R. A. Crowther. 1992. "Cloning of a Big Tau Microtubule-Associated Protein Characteristic of the Peripheral Nervous System." *Proceedings of the National Academy of Sciences of the United States of America* 89 (5): 1983–87. https://doi.org/10.1073/PNAS.89.5.1983.

Goedert, M., M. G. Spillantini, R. Jakes, D. Rutherford, and R. A. Crowther. 1989. "Multiple Isoforms of Human Microtubule-Associated Protein Tau: Sequences and Localization in Neurofibrillary Tangles of Alzheimer's Disease." *Neuron* 3 (4): 519–26. https://doi.org/10.1016/0896-6273(89)90210-9.

Goode, B. L., and S. C. Feinstein. 1994. "Identification of a Novel Microtubule Binding and Assembly Domain in the Developmentally Regulated Inter-Repeat Region of Tau." *The Journal of Cell Biology* 124 (5): 769–81. https://doi.org/10.1083/JCB.124.5.769.

Grassi, Diego, Shannon Howard, Minghai Zhou, Natalia Diaz-Perez, Nicolai T. Urban, Debbie Guerrero-Given, Naomi Kamasawa, Laura A. Volpicelli-Daley, Philip LoGrasso, and Corinne Ida Lasmézas. 2018. "Identification of a Highly Neurotoxic α-Synuclein Species Inducing Mitochondrial Damage and Mitophagy in Parkinson's Disease." *Proceedings of the National Academy of Sciences of the United States of America* 115 (11): E2634–43. https://doi.org/10.1073/PNAS.1713849115/-/DCSUPPLEMENTAL.

Grundke-Iqbal, I., K. Iqbal, Y. C. Tung, M. Quinlan, H. M. Wisniewski, and L. I. Binder. 1986. "Abnormal Phosphorylation of the Microtubule-Associated Protein Tau (Tau) in Alzheimer Cytoskeletal Pathology." *Proceedings of the National Academy of Sciences of the United States of America* 83 (13): 4913–17. https://doi.org/10.1073/pnas.83.13.4913.

Guillozet, Angela L., Sandra Weintraub, Deborah C. Mash, and M. Marsel Mesulam. 2003. "Neurofibrillary Tangles, Amyloid, and Memory in Aging and Mild Cognitive Impairment." *Archives of Neurology* 60 (5): 729–36. https://doi.org/10.1001/ARCHNEUR.60.5.729.

Guo, Jing L., A. Bulst, A. Soares, K. Callaerts, S. Calafate, F. Stevenaert, J.P. Daniels,

et al. 2016. "The Dynamics and Turnover of Tau Aggregates in CulturedCells." *The Journal of Biological Chemistry* 291 (25): 13175–93.

Guo, Tong, Wendy Noble, and Diane P. Hanger. 2017. "Roles of Tau Protein in Health and Disease." *Acta Neuropathologica* 133 (5): 665–704. https://doi.org/10.1007/S00401-017-1707-9.

Gyparaki, Melina Theoni, Arian Arab, Elena M. Sorokina, Adriana N. Santiago-Ruiz, Christopher H. Bohrer, Jie Xiao, and Melike Lakadamyali. 2021. "Tau Forms Oligomeric Complexes on Microtubules That Are Distinct from Tau Aggregates." *Proceedings of the National Academy of Sciences of the United States of America* 118 (19). https://doi.org/10.1073/PNAS.2021461118/-/DCSUPPLEMENTAL.

Hamano, Tadanori, Soichi Enomoto, Norimichi Shirafuji, Masamichi Ikawa, Osamu Yamamura, Shu Hui Yen, and Yasunari Nakamoto. 2021. "Autophagy and Tau Protein." *International Journal of Molecular Sciences* 22 (14). https://doi.org/10.3390/IJMS22147475.

Hamano, Tadanori, Tania F. Gendron, Ena Causevic, Shu Hui Yen, Wen Lang Lin, Ciro Isidoro, Michael Deture, and Li Wen Ko. 2008. "Autophagic-Lysosomal Perturbation Enhances Tau Aggregation in Transfectants with Induced Wild-Type Tau Expression." *The European Journal of Neuroscience* 27 (5): 1119–30. https://doi.org/10.1111/J.1460-9568.2008.06084.X.

He, Zhuohao, Jennifer D. McBride, Hong Xu, Lakshmi Changolkar, Soo jung Kim, Bin Zhang, Sneha Narasimhan, et al. 2020. "Transmission of Tauopathy Strains Is Independent of Their Isoform Composition." *Nature Communications 2020 11:1* 11 (1): 1–18. https://doi.org/10.1038/s41467-019-13787-x.

Heilemann, Mike, Sebastian Van De Linde, Mark Schüttpelz, Robert Kasper, Britta Seefeldt, Anindita Mukherjee, Philip Tinnefeld, and Markus Sauer. 2008. "Subdiffraction-Resolution Fluorescence Imaging with Conventional Fluorescent Probes." *Angewandte Chemie (International Ed. in English)* 47 (33): 6172–76. https://doi.org/10.1002/ANIE.200802376.

Hempen, Bart, and Jean Pierre Brion. 1996. "Reduction of Acetylated Alpha-Tubulin Immunoreactivity in Neurofibrillary Tangle-Bearing Neurons in Alzheimer's Disease." *Journal of Neuropathology and Experimental Neurology* 55 (9): 964–72. https://doi.org/10.1097/00005072-199609000-00003.

Hess, Samuel T., Thanu P.K. Girirajan, and Michael D. Mason. 2006. "Ultra-High Resolution Imaging by Fluorescence Photoactivation Localization Microscopy." *Biophysical Journal* 91 (11): 4258. https://doi.org/10.1529/BIOPHYSJ.106.091116.

Hill, Emily, Thomas K. Karikari, Kevin G. Moffat, Magnus J.E. Richardson, and Mark J. Wall. 2019. "Introduction of Tau Oligomers into Cortical Neurons Alters Action Potential Dynamics and Disrupts Synaptic Transmission and Plasticity." *ENeuro* 6 (5). https://doi.org/10.1523/ENEURO.0166-19.2019.

Huang, Bo, Wenqin Wang, Mark Bates, and Xiaowei Zhuang. 2008. "Three-Dimensional Super-Resolution Imaging by Stochastic Optical Reconstruction Microscopy."

Science 319 (5864): 810–13. https://doi.org/10.1126/science.1153529.

Huseby, Carol J., and Jeff Kuret. 2016. "Analyzing Tau Aggregation with Electron Microscopy." *Methods in Molecular Biology (Clifton, N.J.)* 1345: 101–12. https://doi.org/10.1007/978-1-4939-2978-8_7.

Hutton, M., C. L. Lendon, P. Rizzu, M. Baker, S. Froelich, H. H. Houlden, S. Pickering-Brown, et al. 1998. "Association of Missense and 5′-Splice-Site Mutations in Tau with the Inherited Dementia FTDP-17." *Nature 1998 393:6686* 393 (6686): 702–5. https://doi.org/10.1038/31508.

Illenberger, Susanne, Qingyi Zheng-Fischhöfer, Ute Preuss, Karsten Stamer, Karlheinz Baumann, Bernhard Trinczek, Jacek Biernat, Robert Godemann, Eva Maria Mandelkow, and Eckhard Mandelkow. 1998. "The Endogenous and Cell Cycle-Dependent Phosphorylation of Tau Protein in Living Cells: Implications for Alzheimer's Disease." *Molecular Biology of the Cell* 9 (6): 1495–1512. https://doi.org/10.1091/mbc.9.6.1495.

Janning, Dennis, Maxim Igaev, Frederik Sündermann, Jörg Brühmann, Oliver Beutel, Jürgen J. Heinisch, Lidia Bakota, Jacob Piehler, Wolfgang Junge, and Roland Brandt. 2014. "Single-Molecule Tracking of Tau Reveals Fast Kiss-and-Hop Interaction with Microtubules in Living Neurons." *Molecular Biology of the Cell* 25 (22): 3541. https://doi.org/10.1091/MBC.E14-06-1099.

Johnson, Gail V.W., and William H. Stoothoff. 2004. "Tau Phosphorylation in Neuronal Cell Function and Dysfunction." *Journal of Cell Science* 117 (Pt 24): 5721–29. https://doi.org/10.1242/JCS.01558.

Jung, D., D. Filliol, M. Miehe, and A. Rendon. 1993. "Interaction of Brain Mitochondria with Microtubules Reconstituted from Brain Tubulin and MAP2 or TAU." *Cell Motility and the Cytoskeleton* 24 (4): 245–55. https://doi.org/10.1002/CM.970240405.

Kadavath, Harindranath, Romina V. Hofele, Jacek Biernat, Satish Kumar, Katharina Tepper, Henning Urlaub, Eckhard Mandelkow, and Markus Zweckstetter. 2015. "Tau Stabilizes Microtubules by Binding at the Interface between Tubulin Heterodimers." *Proceedings of the National Academy of Sciences of the United States of America* 112 (24): 7501–6. https://doi.org/10.1073/PNAS.1504081112/SUPPL_FILE/PNAS.1504081112.SAPP.PDF.

Kanai, Y, J Chen, and N Hirokawa. 1992. "Microtubule Bundling by Tau Proteins in Vivo: Analysis of Functional Domains." *The EMBO Journal* 11 (11): 3953–61. http://www.ncbi.nlm.nih.gov/pubmed/1396588.

Katsinelos, Taxiarchis, Marcel Zeitler, Eleni Dimou, Andromachi Karakatsani, Hans Michael Müller, Eliana Nachman, Julia P. Steringer, Carmen Ruiz de Almodovar, Walter Nickel, and Thomas R. Jahn. 2018. "Unconventional Secretion Mediates the Trans-Cellular Spreading of Tau." *Cell Reports* 23 (7): 2039–55. https://doi.org/10.1016/J.CELREP.2018.04.056.

Kaufman, Sarah K., David W. Sanders, Talitha L. Thomas, Allison J. Ruchinskas, Jaime

Vaquer-Alicea, Apurwa M. Sharma, Timothy M. Miller, and Marc I. Diamond. 2016. "Tau Prion Strains Dictate Patterns of Cell Pathology, Progression Rate, and Regional Vulnerability In Vivo." *Neuron* 92 (4): 796–812. https://doi.org/10.1016/J.NEURON.2016.09.055.

Keck, Susi, Robert Nitsch, Tilman Grune, and Oliver Ullrich. 2003. "Proteasome Inhibition by Paired Helical Filament-Tau in Brains of Patients with Alzheimer's Disease." *Journal of Neurochemistry* 85 (1): 115–22. https://doi.org/10.1046/J.1471-4159.2003.01642.X.

Keller, Jeffrey N., Jillian Gee, and Qunxing Ding. 2002. "The Proteasome in Brain Aging." *Ageing Research Reviews* 1 (2): 279–93. https://doi.org/10.1016/S1568-1637(01)00006-X.

Keller, Jeffrey N., Keith B. Hanni, and William R. Markesbery. 2000. "Impaired Proteasome Function in Alzheimer's Disease." *Journal of Neurochemistry* 75 (1): 436–39. https://doi.org/10.1046/J.1471-4159.2000.0750436.X.

Kellogg, Elizabeth H., Nisreen M.A. Hejab, Simon Poepsel, Kenneth H. Downing, Frank DiMaio, and Eva Nogales. 2018. "Near-Atomic Model of Microtubule-Tau Interactions." *Science* 360 (6394): 1242–46. https://doi.org/10.1126/science.aat1780.

Khatoon, Sabiha, Inge Grundke-Iqbal, and Khalid Iqbal. 1992. "Brain Levels of Microtubule-Associated Protein Tau Are Elevated in Alzheimer's Disease: A Radioimmuno-Slot-Blot Assay for Nanograms of the Protein." *Journal of Neurochemistry* 59 (2): 750–53. https://doi.org/10.1111/J.1471-4159.1992.TB09432.X.

Kimura, Taeko, Govinda Sharma, Koichi Ishiguro, and Shin Ichi Hisanaga. 2018. "Phospho-Tau Bar Code: Analysis of Phosphoisotypes of Tau and Its Application to Tauopathy." *Frontiers in Neuroscience*. Frontiers Media S.A. https://doi.org/10.3389/fnins.2018.00044.

Kopke, E., Y. C. Tung, S. Shaikh, C. A. Del Alonso, K. Iqbal, and I. Grundke-Iqbal. 1993. "Microtubule-Associated Protein Tau. Abnormal Phosphorylation of a Non- Paired Helical Filament Pool in Alzheimer Disease." *Journal of Biological Chemistry* 268 (32): 24374–84.

Krüger, Ulrike, Yipeng Wang, Satish Kumar, and Eva Maria Mandelkow. 2012. "Autophagic Degradation of Tau in Primary Neurons and Its Enhancement by Trehalose." *Neurobiology of Aging* 33 (10): 2291–2305. https://doi.org/10.1016/J.NEUROBIOLAGING.2011.11.009.

La-Rocque, Samantha De, Edoardo Moretto, Ioana Butnaru, and Giampietro Schiavo. 2021. "Knockin' on Heaven's Door: Molecular Mechanisms of Neuronal Tau Uptake." *Journal of Neurochemistry* 156 (5): 563–88. https://doi.org/10.1111/JNC.15144.

Lasagna-Reeves, Cristian A., Diana L. Castillo-Carranza, Urmi Sengupta, Audra L. Clos, George R. Jackson, and Rakez Kayed. 2011. "Tau Oligomers Impair Memory and

Induce Synaptic and Mitochondrial Dysfunction in Wild-Type Mice." *Molecular Neurodegeneration* 6 (1). https://doi.org/10.1186/1750-1326-6-39.

Lee, Gloria, and Chad J. Leugers. 2012. "Tau and Tauopathies." *Progress in Molecular Biology and Translational Science* 107: 263–93. https://doi.org/10.1016/B978-0-12-385883-2.00004-7.

Lee, V. M.Y., M. Goedert, and J. Q. Trojanowski. 2001. "Neurodegenerative Tauopathies." *Annual Review of Neuroscience* 24: 1121–59. https://doi.org/10.1146/ANNUREV.NEURO.24.1.1121.

Lelek, Mickaël, Melina T. Gyparaki, Gerti Beliu, Florian Schueder, Juliette Griffié, Suliana Manley, Ralf Jungmann, Markus Sauer, Melike Lakadamyali, and Christophe Zimmer. 2021. "Single-Molecule Localization Microscopy." *Nature Reviews Methods Primers 2021 1:1* 1 (1): 1–27. https://doi.org/10.1038/s43586-021-00038-x.

Levet, Florian, Eric Hosy, Adel Kechkar, Corey Butler, Anne Beghin, Daniel Choquet, and Jean Baptiste Sibarita. 2015. "SR-Tesseler: A Method to Segment and Quantify Localization-Based Super-Resolution Microscopy Data." *Nature Methods* 12 (11): 1065–71. https://doi.org/10.1038/nmeth.3579.

Li, Bin, Muhammad Omar Chohan, Inge Grundke-Iqbal, and Khalid Iqbal. 2007. "Disruption of Microtubule Network by Alzheimer Abnormally Hyperphosphorylated Tau." *Acta Neuropathologica* 113 (5): 501–11. https://doi.org/10.1007/S00401-007-0207-8.

Li, Dan, and Yong Ku Cho. 2020. "High Specificity of Widely Used Phospho-tau Antibodies Validated Using a Quantitative Whole-cell Based Assay." *Journal of Neurochemistry* 152 (1): 122–35. https://doi.org/10.1111/jnc.14830.

Lilienbaum, Alain. 2013. "Relationship between the Proteasomal System and Autophagy." *International Journal of Biochemistry and Molecular Biology* 4 (1): 1. /pmc/articles/PMC3627065/.

Lindwall, G., and R. D. Cole. 1984. "Phosphorylation Affects the Ability of Tau Protein to Promote Microtubule Assembly." *Journal of Biological Chemistry* 259 (8): 5301–5. https://doi.org/10.1016/S0021-9258(17)42989-9.

Liu, Ying Hua, Wei Wei, Jun Yin, Gong Ping Liu, Qun Wang, Fu Yuan Cao, and Jian Zhi Wang. 2009. "Proteasome Inhibition Increases Tau Accumulation Independent of Phosphorylation." *Neurobiology of Aging* 30 (12): 1949–61. https://doi.org/10.1016/J.NEUROBIOLAGING.2008.02.012.

Maeda, Sumihiro, Naruhiko Sahara, Yuko Saito, Miyuki Murayama, Yuji Yoshiike, Hyonchol Kim, Tomohiro Miyasaka, Shigeo Murayama, Atsushi Ikai, and Akihiko Takashima. 2007. "Granular Tau Oligomers as Intermediates of Tau Filaments." *Biochemistry* 46 (12): 3856–61. https://doi.org/10.1021/bi061359o.

Makky, Ali, Luc Bousset, Karine Madiona, and Ronald Melki. 2020. "Atomic Force Microscopy Imaging and Nanomechanical Properties of Six Tau Isoform

Assemblies." *Biophysical Journal* 119 (12): 2497–2507.
https://doi.org/10.1016/J.BPJ.2020.10.045.

Makrides, Victoria, Ting E. Shen, Rajinder Bhatia, Bettye L. Smith, Julian Thimm,
Ratneshwar Lal, and Stuart C. Feinstein. 2003. "Microtubule-Dependent
Oligomerization of Tau: Implications for Physiological Tau Function and
Tauopathies." *Journal of Biological Chemistry* 278 (35): 33298–304.
https://doi.org/10.1074/jbc.M305207200.

Marianayagam, Neelan J., Margaret Sunde, and Jacqueline M. Matthews. 2004. "The
Power of Two: Protein Dimerization in Biology." *Trends in Biochemical Sciences*.
Trends Biochem Sci. https://doi.org/10.1016/j.tibs.2004.09.006.

Martin, Ludovic, Xenia Latypova, Cornelia M. Wilson, Amandine Magnaudeix, Marie
Laure Perrin, Catherine Yardin, and Faraj Terro. 2013. "Tau Protein Kinases:
Involvement in Alzheimer's Disease." *Ageing Research Reviews* 12 (1): 289–309.
https://doi.org/10.1016/J.ARR.2012.06.003.

Matsuo, Eriko S., Ryong Woon Shin, Melvin L. Billingsley, Andre Van deVoorde, Michael
O'Connor, John Q. Trojanowski, and Virginia M.Y. Lee. 1994. "Biopsy-Derived Adult
Human Brain Tau Is Phosphorylated at Many of the Same Sites as Alzheimer's
Disease Paired Helical Filament Tau." *Neuron* 13 (4): 989–1002.
https://doi.org/10.1016/0896-6273(94)90264-X.

Mauthe, Mario, Idil Orhon, Cecilia Rocchi, Xingdong Zhou, Morten Luhr, Kerst Jan
Hijlkema, Robert P. Coppes, Nikolai Engedal, Muriel Mari, and Fulvio Reggiori.
2018. "Chloroquine Inhibits Autophagic Flux by Decreasing Autophagosome-
Lysosome Fusion." *Autophagy* 14 (8): 1435–55.
https://doi.org/10.1080/15548627.2018.1474314.

Meng, Lihao, Royce Mohan, Benjamin H.B. Kwok, Mikael Elofsson, Ny Sin, and Craig M.
Crews. 1999. "Epoxomicin, a Potent and Selective Proteasome Inhibitor, Exhibits in
Vivo Antiinflammatory Activity." *Proceedings of the National Academy of Sciences
of the United States of America* 96 (18): 10403–8.
https://doi.org/10.1073/PNAS.96.18.10403.

Merezhko, Maria, Cecilia A. Brunello, Xu Yan, Helena Vihinen, Eija Jokitalo, Riikka Liisa
Uronen, and Henri J. Huttunen. 2018. "Secretion of Tau via an Unconventional
Non-Vesicular Mechanism." *Cell Reports* 25 (8): 2027-2035.e4.
https://doi.org/10.1016/j.celrep.2018.10.078.

Min, Sang Won, Xu Chen, Tara E. Tracy, Yaqiao Li, Yungui Zhou, Chao Wang, Kotaro
Shirakawa, et al. 2015. "Critical Role of Acetylation in Tau-Mediated
Neurodegeneration and Cognitive Deficits." *Nature Medicine* 21 (10): 1154–62.
https://doi.org/10.1038/NM.3951.

Mohan, Nitin, Elena M. Sorokina, Ione Vilanova Verdeny, Angel Sandoval Alvarez, and
Melike Lakadamyali. 2019. "Detyrosinated Microtubules Spatially Constrain
Lysosomes Facilitating Lysosome-Autophagosome Fusion." *Journal of Cell Biology*
218 (2): 632–43. https://doi.org/10.1083/jcb.201807124.

Moltedo, Ornella, Paolo Remondelli, and Giuseppina Amodio. 2019. "The Mitochondria–Endoplasmic Reticulum Contacts and Their Critical Role in Aging and Age-Associated Diseases." *Frontiers in Cell and Developmental Biology* 7 (August). https://doi.org/10.3389/FCELL.2019.00172.

Morsch, Renee, William Simon, and Paul D. Coleman. 1999. "Neurons May Live for Decades with Neurofibrillary Tangles." *Journal of Neuropathology and Experimental Neurology* 58 (2): 188–97. https://doi.org/10.1097/00005072-199902000-00008.

Myeku, Natura, Catherine L. Clelland, Sheina Emrani, Nikolay V. Kukushkin, Wai Haung Yu, Alfred L. Goldberg, and Karen E. Duff. 2016. "Tau-Driven 26S Proteasome Impairment and Cognitive Dysfunction Can Be Prevented Early in Disease by Activating CAMP-PKA Signaling." *Nature Medicine* 22 (1): 46–53. https://doi.org/10.1038/NM.4011.

Necula, Mihaela, and Jeff Kuret. 2004. "Electron Microscopy as a Quantitative Method for Investigating Tau Fibrillization." *Analytical Biochemistry* 329 (2): 238–46. https://doi.org/10.1016/J.AB.2004.02.023.

Neve, Rachael L., Peter Harris, Kenneth S. Kosik, David M. Kurnit, and Timothy A. Donlon. 1986. "Identification of CDNA Clones for the Human Microtubule-Associated Protein Tau and Chromosomal Localization of the Genes for Tau and Microtubule-Associated Protein 2." *Brain Research* 387 (3): 271–80. https://doi.org/10.1016/0169-328X(86)90033-1.

Nixon, Ralph A. 2013. "The Role of Autophagy in Neurodegenerative Disease." *Nature Medicine 2013 19:8* 19 (8): 983–97. https://doi.org/10.1038/nm.3232.

Nixon, Ralph A., Jerzy Wegiel, Asok Kumar, Wai Haung Yu, Corrinne Peterhoff, Anne Cataldo, and Ana Maria Cuervo. 2005. "Extensive Involvement of Autophagy in Alzheimer Disease: An Immuno-Electron Microscopy Study." *Journal of Neuropathology and Experimental Neurology* 64 (2): 113–22. https://doi.org/10.1093/JNEN/64.2.113.

Noble, Wendy, Emmanuel Planel, Cindy Zehr, Vicki Olm, Jordana Meyerson, Farhana Suleman, Kate Gaynor, et al. 2005. "Inhibition of Glycogen Synthase Kinase-3 by Lithium Correlates with Reduced Tauopathy and Degeneration in Vivo." *Proceedings of the National Academy of Sciences of the United States of America* 102 (19): 6990–95. https://doi.org/10.1073/PNAS.0500466102.

Ondrejcak, Tomas, Igor Klyubin, Grant T. Corbett, Graham Fraser, Wei Hong, Alexandra J. Mably, Matthew Gardener, et al. 2018. "Cellular Prion Protein Mediates the Disruption of Hippocampal Synaptic Plasticity by Soluble Tau in Vivo." *Journal of Neuroscience* 38 (50): 10595–606. https://doi.org/10.1523/JNEUROSCI.1700-18.2018.

Orr, Miranda E., A. Campbell Sullivan, and Bess Frost. 2017. "A Brief Overview of Tauopathy: Causes, Consequences, and Therapeutic Strategies." *Trends in Pharmacological Sciences* 38 (7): 637–48. https://doi.org/10.1016/J.TIPS.2017.03.011.

Otterstrom, Jason, Alvaro Castells-Garcia, Chiara Vicario, Pablo A. Gomez-Garcia, Maria Pia Cosma, and Melike Lakadamyali. 2019. "Super-Resolution Microscopy Reveals How Histone Tail Acetylation Affects DNA Compaction within Nucleosomes in Vivo." *Nucleic Acids Research* 47 (16): 8470–84. https://doi.org/10.1093/nar/gkz593.

Panda, Dulal, Herbert P. Miller, and Leslie Wilson. 1999. "Rapid Treadmilling of Brain Microtubules Free of Microtubule-Associated Proteins in Vitro and Its Suppression by Tau." *Proceedings of the National Academy of Sciences of the United States of America* 96 (22): 12459–64. https://doi.org/10.1073/PNAS.96.22.12459/ASSET/E849AFD9-FFEC-45B2-8A2B-385208053140/ASSETS/GRAPHIC/PQ2193647004.JPEG.

Patterson, Kristina R., Christine Remmers, Yifan Fu, Sarah Brooker, Nicholas M. Kanaan, Laurel Vana, Sarah Ward, et al. 2011. "Characterization of Prefibrillar Tau Oligomers in Vitro and in Alzheimer Disease." *Journal of Biological Chemistry* 286 (26): 23063–76. https://doi.org/10.1074/jbc.M111.237974.

Pedersen, Jan Torleif, and Einar M. Sigurdsson. 2015. "Tau Immunotherapy for Alzheimer's Disease." *Trends in Molecular Medicine* 21 (6): 394–402. https://doi.org/10.1016/J.MOLMED.2015.03.003.

Perreault, Sébastien, Olivier Bousquet, Michel Lauzon, Jacques Paiement, and Nicole Leclerc. 2009. "Increased Association between Rough Endoplasmic Reticulum Membranes and Mitochondria in Transgenic Mice That Express P301L Tau." *Journal of Neuropathology and Experimental Neurology* 68 (5): 503–14. https://doi.org/10.1097/NEN.0B013E3181A1FC49.

Piras, Antonio, Ludovic Collin, Fiona Grüninger, Caroline Graff, and Annica Rönnbäck. 2016. "Autophagic and Lysosomal Defects in Human Tauopathies: Analysis of Post-Mortem Brain from Patients with Familial Alzheimer Disease, Corticobasal Degeneration and Progressive Supranuclear Palsy." *Acta Neuropathologica Communications* 4 (March): 22. https://doi.org/10.1186/S40478-016-0292-9.

Poorkaj, Parvoneh, Thomas D. Bird, Ellen Wijsman, Ellen Nemens, Ralph M. Garruto, Leojean Anderson, Athena Andreadis, Wigbert C. Wiederholt, Murray Raskind, and Gerard D. Schellenberg. 1998. "Tau Is a Candidate Gene for Chromosome 17 Frontotemporal Dementia." *Annals of Neurology* 43 (6): 815–25. https://doi.org/10.1002/ANA.410430617.

Poppek, Diana, Susi Keck, Gennady Ermak, Tobias Jung, Alexandra Stolzing, Oliver Ullrich, Kelvin J.A. Davies, and Tilman Grune. 2006. "Phosphorylation Inhibits Turnover of the Tau Protein by the Proteasome: Influence of RCAN1 and Oxidative Stress." *The Biochemical Journal* 400 (3): 511–20. https://doi.org/10.1042/BJ20060463.

Prusiner, Stanley B. 1984. "Some Speculations about Prions, Amyloid, and Alzheimer's Disease." *New England Journal of Medicine*. N Engl J Med. https://doi.org/10.1056/NEJM198403083101021.

Puangmalai, Nicha, Urmi Sengupta, Nemil Bhatt, Sagar Gaikwad, Mauro Montalbano, Arijit Bhuyan, Stephanie Garcia, et al. 2022. "Lysine 63-Linked Ubiquitination of Tau Oligomers Contributes to the Pathogenesis of Alzheimer's Disease." *Journal of Biological Chemistry* 298 (4): 101766. https://doi.org/10.1016/J.JBC.2022.101766/ATTACHMENT/12B03DCB-328B-4F72-8CC2-BDF203C2A2F7/MMC5.PDF.

Qiang, Liang, Xiaohuan Sun, Timothy O Austin, Mei Liu, Wenqian Yu, and Peter W Baas. 2018. "Tau Does Not Stabilize Axonal Microtubules but Rather Enables Them to Have Long Labile Domains Correspondence." *Current Biology* 28: 2181-2189.e4. https://doi.org/10.1016/j.cub.2018.05.045.

Qiang, Liang, Wenqian Yu, Athena Andreadis, Minhua Luo, and Peter W. Baas. 2006. "Tau Protects Microtubules in the Axon from Severing by Katanin." *The Journal of Neuroscience : The Official Journal of the Society for Neuroscience* 26 (12): 3120–29. https://doi.org/10.1523/JNEUROSCI.5392-05.2006.

Reddy, P. Hemachandra, and Darryll MA Oliver. 2019. "Amyloid Beta and Phosphorylated Tau-Induced Defective Autophagy and Mitophagy in Alzheimer's Disease." *Cells* 8 (5): 488. https://doi.org/10.3390/CELLS8050488.

Reynolds, C. Hugh, Claire J. Garwood, Selina Wray, Caroline Price, Stuart Kellie, Timothy Perera, Marketa Zvelebil, et al. 2008. "Phosphorylation Regulates Tau Interactions with Src Homology 3 Domains of Phosphatidylinositol 3-Kinase, Phospholipase Cgamma1, Grb2, and Src Family Kinases." *The Journal of Biological Chemistry* 283 (26): 18177–86. https://doi.org/10.1074/JBC.M709715200.

Rissman, Robert A., Wayne W. Poon, Mathew Blurton-Jones, Salvatore Oddo, Reidun Torp, Michael P. Vitek, Frank M. LaFerla, Troy T. Rohn, and Carl W. Cotman. 2004. "Caspase-Cleavage of Tau Is an Early Event in Alzheimer Disease Tangle Pathology." *The Journal of Clinical Investigation* 114 (1): 121–30. https://doi.org/10.1172/JCI20640.

Rokach, Lior, and Oded Maimon. 2006. "Clustering Methods." In *Data Mining and Knowledge Discovery Handbook*, 321–52. Springer-Verlag. https://doi.org/10.1007/0-387-25465-x_15.

Rosenberg, Kenneth J., Jennifer L. Ross, H. Eric Feinstein, Stuart C. Feinstein, and Jacob Israelachvili. 2008. "Complementary Dimerization of Microtubule-Associated Tau Protein: Implications for Microtubule Bundling and Tau-Mediated Pathogenesis." *Proceedings of the National Academy of Sciences of the United States of America* 105 (21): 7445–50. https://doi.org/10.1073/pnas.0802036105.

Rubinsztein, David C. 2006. "The Roles of Intracellular Protein-Degradation Pathways in Neurodegeneration." *Nature* 443 (7113): 780–86. https://doi.org/10.1038/NATURE05291.

Rust, Michael J., Mark Bates, and Xiaowei Zhuang. 2006. "Sub-Diffraction-Limit Imaging by Stochastic Optical Reconstruction Microscopy (STORM)." *Nature Methods 2006*

3:10 3 (10): 793–96. https://doi.org/10.1038/nmeth929.

Sanchez-Varo, Raquel, Laura Trujillo-Estrada, Elisabeth Sanchez-Mejias, Manuel Torres, David Baglietto-Vargas, Ines Moreno-Gonzalez, Vanessa De Castro, et al. 2012. "Abnormal Accumulation of Autophagic Vesicles Correlates with Axonal and Synaptic Pathology in Young Alzheimer's Mice Hippocampus." *Acta Neuropathologica* 123 (1): 53–70. https://doi.org/10.1007/S00401-011-0896-X.

Sanders, David W., Sarah K. Kaufman, Sarah L. DeVos, Apurwa M. Sharma, Hilda Mirbaha, Aimin Li, Scarlett J. Barker, et al. 2014. "Distinct Tau Prion Strains Propagate in Cells and Mice and Define Different Tauopathies." *Neuron* 82 (6): 1271–88. https://doi.org/10.1016/j.neuron.2014.04.047.

Santacruz, K., J. Lewis, T. Spires, J. Paulson, L. Kotilinek, M. Ingelsson, A. Guimaraes, et al. 2005. "Medicine: Tau Suppression in a Neurodegenerative Mouse Model Improves Memory Function." *Science* 309 (5733): 476–81. https://doi.org/10.1126/science.1113694.

Sayas, Carmen Laura, Elena Tortosa, Flavia Bollati, Sacnicte Ramírez-Ríos, Isabelle Arnal, and Jesús Avila. 2015. "Tau Regulates the Localization and Function of End-Binding Proteins 1 and 3 in Developing Neuronal Cells." *Journal of Neurochemistry* 133 (5): 653–67. https://doi.org/10.1111/JNC.13091.

Scheres, Sjors HW, Wenjuan Zhang, Benjamin Falcon, and Michel Goedert. 2020. "Cryo-EM Structures of Tau Filaments." *Current Opinion in Structural Biology* 64 (October): 17–25. https://doi.org/10.1016/J.SBI.2020.05.011.

Schindelin, Johannes, Ignacio Arganda-Carreras, Erwin Frise, Verena Kaynig, Mark Longair, Tobias Pietzsch, Stephan Preibisch, et al. 2012. "Fiji: An Open-Source Platform for Biological-Image Analysis." *Nature Methods*. Nature Publishing Group. https://doi.org/10.1038/nmeth.2019.

Schroeder, Sulana K., Aurelie Joly-Amado, Marcia N. Gordon, and Dave Morgan. 2016. "Tau-Directed Immunotherapy: A Promising Strategy for Treating Alzheimer's Disease and Other Tauopathies." *Journal of Neuroimmune Pharmacology : The Official Journal of the Society on NeuroImmune Pharmacology* 11 (1): 9–25. https://doi.org/10.1007/S11481-015-9637-6.

Siahaan, Valerie, Jochen Krattenmacher, Anthony A. Hyman, Stefan Diez, Amayra Hernández-Vega, Zdenek Lansky, and Marcus Braun. 2019. "Kinetically Distinct Phases of Tau on Microtubules Regulate Kinesin Motors and Severing Enzymes." *Nature Cell Biology*. Nature Publishing Group. https://doi.org/10.1038/s41556-019-0374-6.

Sibille, Nathalie, Isabelle Huvent, Caroline Fauquant, Dries Verdegem, Laziza Amniai, Arnaud Leroy, Jean Michel Wieruszeski, Guy Lippens, and Isabelle Landrieu. 2012. "Structural Characterization by Nuclear Magnetic Resonance of the Impact of Phosphorylation in the Proline-Rich Region of the Disordered Tau Protein." *Proteins* 80 (2): 454–62. https://doi.org/10.1002/PROT.23210.

Spiess, Matthias, Pablo Hernandez-Varas, Anna Oddone, Helene Olofsson, Hans Blom,

Dominic Waithe, John G. Lock, Melike Lakadamyali, and Staffan Strömblad. 2018. "Active and Inactive B1 Integrins Segregate into Distinct Nanoclusters in Focal Adhesions." *The Journal of Cell Biology* 217 (6): 1929–40. https://doi.org/10.1083/JCB.201707075.

Spillantini, Maria Grazia, Jill R. Murrell, Michel Goedert, Martin R. Farlow, Aaron Klug, and Bernardino Ghetti. 1998. "Mutation in the Tau Gene in Familial Multiple System Tauopathy with Presenile Dementia." *Proceedings of the National Academy of Sciences of the United States of America* 95 (13): 7737–41. https://doi.org/10.1073/PNAS.95.13.7737.

Spires, Tara L., Jennifer D. Orne, Karen SantaCruz, Rose Pitstick, George A. Carlson, Karen H. Ashe, and Bradley T. Hyman. 2006. "Region-Specific Dissociation of Neuronal Loss and Neurofibrillary Pathology in a Mouse Model of Tauopathy." *American Journal of Pathology* 168 (5): 1598–1607. https://doi.org/10.2353/ajpath.2006.050840.

Stamer, K., R. Vogel, E. Thies, E. Mandelkow, and E. M. Mandelkow. 2002. "Tau Blocks Traffic of Organelles, Neurofilaments, and APP Vesicles in Neurons and Enhances Oxidative Stress." *The Journal of Cell Biology* 156 (6): 1051–63. https://doi.org/10.1083/JCB.200108057.

Sündermann, Frederik, Maria Pilar Fernandez, and Reginald O. Morgan. 2016. "An Evolutionary Roadmap to the Microtubule-Associated Protein MAP Tau." *BMC Genomics* 17 (1): 1–16. https://doi.org/10.1186/S12864-016-2590-9/FIGURES/6.

Swatek, Kirby N., and David Komander. 2016. "Ubiquitin Modifications." *Cell Research* 26 (4): 399–422. https://doi.org/10.1038/CR.2016.39.

Takashima, Akihiko. 2013. "Tauopathies and Tau Oligomers." *Journal of Alzheimer's Disease*. IOS Press. https://doi.org/10.3233/JAD-130653.

Tan, Jeanne M.M., Esther S.P. Wong, Donald S. Kirkpatrick, Olga Pletnikova, Han Seok Ko, Shiam Peng Tay, Michelle W.L. Ho, et al. 2008. "Lysine 63-Linked Ubiquitination Promotes the Formation and Autophagic Clearance of Protein Inclusions Associated with Neurodegenerative Diseases." *Human Molecular Genetics* 17 (3): 431–39. https://doi.org/10.1093/HMG/DDM320.

Tan, Ruensern, Aileen J. Lam, Tracy Tan, Jisoo Han, Dan W. Nowakowski, Michael Vershinin, Sergi Simó, Kassandra M. Ori-McKenney, and Richard J. McKenney. 2019. "Microtubules Gate Tau Condensation to Spatially Regulate Microtubule Functions." *Nature Cell Biology*. Nature Publishing Group. https://doi.org/10.1038/s41556-019-0375-5.

Taniguchi-Watanabe, Sayuri, Tetsuaki Arai, Fuyuki Kametani, Takashi Nonaka, Masami Masuda-Suzukake, Airi Tarutani, Shigeo Murayama, et al. 2016. "Biochemical Classification of Tauopathies by Immunoblot, Protein Sequence and Mass Spectrometric Analyses of Sarkosyl-Insoluble and Trypsin-Resistant Tau." *Acta Neuropathologica* 131 (2): 267–80. https://doi.org/10.1007/S00401-015-1503-3.

Tell, Volkmar, and Andreas Hilgeroth. 2013. "Recent Developments of Protein Kinase

Inhibitors as Potential AD Therapeutics." *Frontiers in Cellular Neuroscience* 7 (NOV). https://doi.org/10.3389/FNCEL.2013.00189.

Thibaudeau, Tiffany A., Raymond T. Anderson, and David M. Smith. 2018. "A Common Mechanism of Proteasome Impairment by Neurodegenerative Disease-Associated Oligomers." *Nature Communications 2018 9:1* 9 (1): 1–14. https://doi.org/10.1038/s41467-018-03509-0.

Vandebroek, Tom, Dick Terwel, Thomas Vanhelmont, Maarten Gysemans, Chris Van Haesendonck, Yves Engelborghs, Joris Winderickx, and Fred Van Leuven. 2006. "Microtubule Binding and Clustering of Human Tau-4R and Tau-P301L Proteins Isolated from Yeast Deficient in Orthologues of Glycogen Synthase Kinase-3β or Cdk5." *Journal of Biological Chemistry* 281 (35): 25388–97. https://doi.org/10.1074/jbc.M602792200.

Wang, Y., U. Krüger, E. Mandelkow, and E. M. Mandelkow. 2010. "Generation of Tau Aggregates and Clearance by Autophagy in an Inducible Cell Model of Tauopathy." *Neuro-Degenerative Diseases* 7 (1–3): 103–7. https://doi.org/10.1159/000285516.

Wang, Y. P., J. Biernat, M. Pickhardt, E. Mandelkow, and E. M. Mandelkow. 2007. "Stepwise Proteolysis Liberates Tau Fragments That Nucleate the Alzheimer-like Aggregation of Full-Length Tau in a Neuronal Cell Model." *Proceedings of the National Academy of Sciences of the United States of America* 104 (24): 10252–57. https://doi.org/10.1073/PNAS.0703676104.

Wang, Yipeng, Marta Martinez-Vicente, Ulrike Krüger, Susmita Kaushik, Esther Wong, Eva Maria Mandelkow, Ana Maria Cuervo, and Eckhard Mandelkow. 2009. "Tau Fragmentation, Aggregation and Clearance: The Dual Role of Lysosomal Processing." *Human Molecular Genetics* 18 (21): 4153–70. https://doi.org/10.1093/HMG/DDP367.

Wegmann, Susanne, Bahareh Eftekharzadeh, Katharina Tepper, Katarzyna M Zoltowska, Rachel E Bennett, Simon Dujardin, Pawel R Laskowski, et al. 2018. "Tau Protein Liquid–Liquid Phase Separation Can Initiate Tau Aggregation." *The EMBO Journal* 37 (7). https://doi.org/10.15252/embj.201798049.

Wegmann, Susanne, Daniel J. Muller, and Eckhard Mandelkow. 2012. "Investigating Fibrillar Aggregates of Tau Protein by Atomic Force Microscopy." *Methods in Molecular Biology (Clifton, N.J.)* 849: 169–83. https://doi.org/10.1007/978-1-61779-551-0_12.

Weingarten, M. D., A. H. Lockwood, S. Y. Hwo, and M. W. Kirschner. 1975. "A Protein Factor Essential for Microtubule Assembly." *Proceedings of the National Academy of Sciences of the United States of America* 72 (5): 1858–62. https://doi.org/10.1073/PNAS.72.5.1858.

Weissmann, Carina, Hans Jürgen Reyher, Anne Gauthier, Heinz Jürgen Steinhoff, Wolfgang Junge, and Roland Brandt. 2009. "Microtubule Binding and Trapping at the Tip of Neurites Regulate Tau Motion in Living Neurons." *Traffic*. https://doi.org/10.1111/j.1600-0854.2009.00977.x.

Wischik, Claude M., Roger T. Staff, Damon J. Wischik, Peter Bentham, Alison D. Murray, John M.D. Storey, Karin A. Kook, and Charles R. Harrington. 2015. "Tau Aggregation Inhibitor Therapy: An Exploratory Phase 2 Study in Mild or Moderate Alzheimer's Disease." *Journal of Alzheimer's Disease : JAD* 44 (2): 705–20. https://doi.org/10.3233/JAD-142874.

Wittmann, C. W., M. F. Wszolek, J. M. Shulman, P. M. Salvaterra, J. Lewis, M. Hutton, and M. B. Feany. 2001. "Tauopathy in Drosophila: Neurodegeneration without Neurofibrillary Tangles." *Science* 293 (5530): 711–14. https://doi.org/10.1126/science.1062382.

Yu, Wenqian, Liang Qiang, Joanna M. Solowska, Arzu Karabay, Sirin Korulu, and Peter W. Baas. 2008. "The Microtubule-Severing Proteins Spastin and Katanin Participate Differently in the Formation of Axonal Branches." *Molecular Biology of the Cell* 19 (4): 1485. https://doi.org/10.1091/MBC.E07-09-0878.

Yuan, Aidong, Asok Kumar, Corrinne Peterhoff, Karen Duff, and Ralph A. Nixon. 2008. "Axonal Transport Rates in Vivo Are Unaffected by Tau Deletion or Overexpression in Mice." *The Journal of Neuroscience : The Official Journal of the Society for Neuroscience* 28 (7): 1682–87. https://doi.org/10.1523/JNEUROSCI.5242-07.2008.

Yuzwa, Scott A., Matthew S. Macauley, Julia E. Heinonen, Xiaoyang Shan, Rebecca J. Dennis, Yuan He, Garrett E. Whitworth, et al. 2008. "A Potent Mechanism-Inspired O-GlcNAcase Inhibitor That Blocks Phosphorylation of Tau in Vivo." *Nature Chemical Biology* 4 (8): 483–90. https://doi.org/10.1038/NCHEMBIO.96.

Zhang, Bin, Jenna Carroll, John Q. Trojanowski, Yuemang Yao, Michiyo Iba, Justin S. Potuzak, Anne Marie L. Hogan, et al. 2012. "The Microtubule-Stabilizing Agent, Epothilone D, Reduces Axonal Dysfunction, Neurotoxicity, Cognitive Deficits, and Alzheimer-like Pathology in an Interventional Study with Aged Tau Transgenic Mice." *The Journal of Neuroscience : The Official Journal of the Society for Neuroscience* 32 (11): 3601–11. https://doi.org/10.1523/JNEUROSCI.4922-11.2012.

Zhang, Bin, Arpita Maiti, Sharon Shively, Fara Lakhani, Gaye McDonald-Jones, Jennifer Bruce, Edward B. Lee, et al. 2005. "Microtubule-Binding Drugs Offset Tau Sequestration by Stabilizing Microtubules and Reversing Fast Axonal Transport Deficits in a Tauopathy Model." *Proceedings of the National Academy of Sciences of the United States of America* 102 (1): 227–31. https://doi.org/10.1073/PNAS.0406361102.

Zhang, J. Y., S. J. Liu, H. L. Li, and J. Z. Wang. 2005. "Microtubule-Associated Protein Tau Is a Substrate of ATP/Mg(2+)-Dependent Proteasome Protease System." *Journal of Neural Transmission (Vienna, Austria : 1996)* 112 (4): 547–55. https://doi.org/10.1007/S00702-004-0196-X.

Zhang, Wenjuan, Benjamin Falcon, Alexey G. Murzin, Juan Fan, R. Anthony Crowther, Michel Goedert, and Sjors H.W. Scheres. 2019a. "Heparin-Induced Tau Filaments Are Polymorphic and Differ from Those in Alzheimer's and Pick's Diseases." *ELife* 8 (February). https://doi.org/10.7554/eLife.43584.

———. 2019b. "Heparin-Induced Tau Filaments Are Polymorphic and Differ from Those in Alzheimer's and Pick's Diseases." *ELife* 8 (February). https://doi.org/10.7554/ELIFE.43584.

Zhang, Wenjuan, Airi Tarutani, Kathy L. Newell, Alexey G. Murzin, Tomoyasu Matsubara, Benjamin Falcon, Ruben Vidal, et al. 2020. "Novel Tau Filament Fold in Corticobasal Degeneration." *Nature 2020 580:7802* 580 (7802): 283–87. https://doi.org/10.1038/s41586-020-2043-0.